Advances in photostop

Neil Warner

Department of Chemistry

University of Durham

A thesis submitted in partial fulfilment of the requirements for the degree of Doctor of Philosophy

2016

ABSTRACT

This thesis is an expansion on previous work using the photostop technique for the production of near-zero velocity atoms and molecules. The goal is to produce stopped SH molecules and trap them in a permanent magnetic trap and the aim of this project was to construct a new experimental apparatus to accomplish this.

During initial tests of the apparatus, the Rayleigh scattering cross-section of N_2 was measured to provide a reference point for future experiments. The uncertainty and systematic errors in the measurements was such that definitive quantitative results of this were not be obtained at this stage.

The emerging technique of cavity-enhanced laser-induced fluorescence (CELIF) was used to perform absolute number density measurements of a molecular beam of SO_2. CELIF was then applied to measuring the photostop of SD/SH. This showed that CELIF would not have the required sensitivity to measure the trapped SD/SH molecules due to issues of stray light from the lasers. As a result of this we elected to use resonance-enhanced multi-photon ionisation (REMPI) as an alternative.

We devised and constructed a novel ion extraction system for use in performing REMPI, which was based on a time-of-flight mass spectroscopy system, but utilising the magnets themselves as electrodes, as well as some ion lensing components. This was initially tested using Xe, showing a strong signal and good mass resolution. Using this, the photostop of SH and S was measured showing that the detection apparatus is able to distinguish signal over a range of 9 orders of magnitude. However, despite this sensitivity, the trapping of these stopped molecules could not initially be demonstrated as the signal from these stopped molecules was obscured by signal from the inadvertent dissociation of the background parent molecules by the probe laser. More recent measurements in the group have directly addressed this issue with background subtraction and the results have now demonstrated the trapping of SH.

Significant headway has been made in the demonstration of the trapping of SH produced by photostop. From the results produced using REMPI the detection limit has improved significantly over the prior experiments and very recent measurements have successfully demonstrated the trapping of SH.

CONTENTS

LIST OF ABBREVIATIONS

CELIF	cavity-enhanced laser-induced fluorescence.
CRDS	cavity ring-down spectroscopy.
FIG	fast ionisation gauge.
LIF	laser-induced fluorescence.
MCP	microchannel plate.
PMT	photomultiplier tube.
REMPI	resonance-enhanced multiphoton ionisation.
RGA	residual gas analyser.
VMI	velocity map ion imaging.

Declaration

The material contained within this thesis has not previously been submitted for a degree at the University of Durham or at any other university. The research reported within this thesis has been conducted by the author unless indicated otherwise.

Copyright

Acknowledgements

I'd like to thank my supervisors Eckart Wrede and David Carty for putting up with me and guiding me through this project for the past four years, Paul White and Lee McAlpine in the Mechanical workshop for making my madcap designs actually work, Bryan Denton and Kelvin Appleby in the Electronics workshop for helping us get the instruments working and the EPSRC for funding. Additionally I would like to thank the various 4th year undergraduates who have worked with me on this project namely: Tom Wilson, Charlotte Gerwat, Gareth Davies, James Crickmore, Grace Dempsey and Jack Eardley as well as Dennis Deng, our former post-doctoral researcher and the other members of the Durham Laser Spectroscopy and Dynamics Group.

Part I

BACKGROUND AND EXPERIMENTAL DESIGN

1. INTRODUCTION AND LITERATURE REVIEW

The field of ultracold physics has become a matter of significant interest in recent years not only due to academic curiosity but also on account of the potential applications. Experimental work performed with molecular gases at ultracold temperatures has provided insight into a number of areas such as many-body physics, quantum dynamics of complex systems, quantum chemistry and fundamental forces of nature. To explore this area a variety of new experimental techniques have been developed including magnetic and electric decelerators, magneto- and photo-association, buffer gas cooling and more recently Sisyphus cooling. The photostop technique is one such method of producing cold molecules and is the focus of this project. In order to fully understand this experiment and its place in the field we must first discuss the domain of ultracold molecules as a whole.

1.1 Cold and Ultracold regimes

Before we can properly examine this field, the exact nature of what is meant by cold and ultracold needs to be defined. These two states are often defined in relation to the de Broglie wavelength, which is a manifestation of the wave/particle duality and is defined by the equation

$$\lambda_{\mathrm{dB}} = \frac{h}{p} = \left(\frac{2\pi\hbar^2}{mk_{\mathrm{B}}T}\right)^{1/2}, \tag{1.1}$$

where λ_{dB} is the de Broglie wavelength of the molecule, h is the Planck constant, p is the momentum of the particle, $\hbar$ is the reduced Planck constant, k_{B} is the Boltzmann constant, m is the mass of the particle and T is its temperature. The cold region is defined as being a temperature at which the de Broglie wavelength of the molecule

is the same order of magnitude as the classical size of the molecule and typically lies in the region of 1 K to 1 mK. The ultracold region is defined where the de Broglie wavelength is in the same order of magnitude as the average molecule separation of the ensemble and in terms of temperature tends to lie below 1 mK. In this region the dynamics of the molecules are predominantly wavelike as the wavepackets of individual molecules overlap. This can lead to unique quantum mechanical events such as the formation of Bose-Einstein condensates (BECs) where a dilute gas of bosons are cooled to such a degree that the vast majority occupy the lowest quantum state which results in the manifestation of macroscopic quantum phenomena [1, 2]. An illustrative summary of the different properties of the temperature regimes is given in Fig. 1.1.

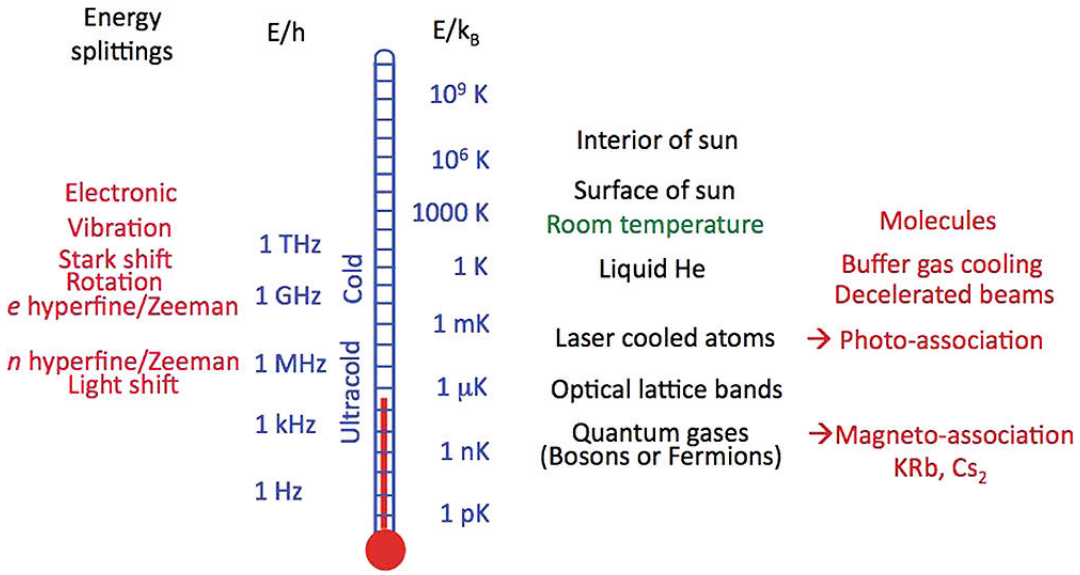

Fig. 1.1 Illustration of the phenomena associated with various ranges of energy/temperature taken from [3]. From left to right the columns indicate: the energy splitting at this temperature, the frequency of the transitions that occur at this temperature, the absolute value of the temperature in this state (in K), typical environments that exist at this temperature and different cooling methods that are used to reach this temperature.

1.2 Applications of cold molecules

Considering the quantum mechanical nature of cold and ultracold molecules there are many potential applications to which they could be utilised. Additionally, the fact that the velocity of these molecules is significantly reduced gives rise to potential

use in spectroscopy and related fields. Furthermore, the low temperature of these molecules may allow them to be held in magnetic, electric or optical traps, which in turn may lead to more complex applications.

1.2.1 Chemical Reaction Dynamics

As previously mentioned, at ultracold temperatures the quantum mechanical nature of the molecules' translational properties become more dominant (in particular with regards to translational degrees of freedom). This allows a direct insight into the fine quantum mechanical nature of chemical reactions as the molecules can no longer be accurately described as particles that collide but are more akin to interfering waves [4, 5]. Because of this, the dynamics of ultracold molecules are characterised by quantum effects which could potentially lead to the production of hard to produce molecules. To illustrate this let us consider an example where a desired product is separated from the reactants by an insurmountable reaction barrier. Classically the product would not be able to be produced on account of the barrier but in the quantum regime the products could effectively tunnel through the reaction barrier. This effectively means that measurements of chemical reaction rates of these species allow for an assessment of the roles of tunnelling, zero-point energy and quantum reflection effects have in chemical reactivity. This can also potentially provide new reaction pathways to be used as, when molecules are cooled to low temperatures, the likelihood of populating specific rovibrational states is enhanced due to the state selectivity of inelastic and reactive collisions. In addition to this, as the durations for ultracold interactions tends to be longer than at room temperature, which increases the molecules' sensitivity to weak external fields and potentially allows a greater degree of control over them.

One of the avenues of investigation is the production of entangled molecules. Entanglement is a phenomena where if one entangled species changes state the other automatically changes state as well regardless of distance. This phenomena is vital for the study of quantum information transfer and the development of quantum computing schemes based on the manipulation of atomic and molecular systems.

Photodissociation of molecules in a BEC can be used for the controlled preparation of entangled pairs of radicals [6]. The production of entangled molecules may also be applied to realising the coherent control of bimolecular chemical reactions [7].

The production of ultracold molecules drastically changes the nature of intermolecular interactions and may allow for coherent control of bi-molecular collision processes with laser fields. Coherent control of molecular processes is based around quantum interference between distinct interactions leading to the same outcome. This relies on creating coherent superpositions of internal states of molecules which are moving with different relative momenta corresponding to the same momentum state of the centre of mass motion [7]. Creating such coherent superpositions in a gas with random molecular motions is highly problematic. However, methods have been proposed to create coherent superpositions of different Zeeman or Stark states in the presence of a magnetic or electric field [8]. At certain field strengths the energy splitting between different angular momentum states of the colliding molecules becomes equal, which enables coherent control of these collisions.

In order for this potential to be realised it is clear that methods for the production of dense ensembles of ultracold molecules will be required. As will be outlined in Section 1.3, there are a number of techniques in development to achieve this but it remains a significant challenge. However if this obstacle can be overcome then it will lead the way into the study of new avenues of ultracold chemistry as well as the production of new quantum materials.

1.2.2 High-resolution spectroscopy

In the majority of cases spectroscopic measurements are taken at room temperature where the average velocity of gas-phase molecules is around $500\,\mathrm{m\,s^{-1}}$ [9]. At this velocity the molecules being examined by the spectroscopic methods often spend a relatively short time in the measurement device. This can also result in Doppler broadening, whereby the thermal motion of the species will result in different transition frequencies for those travelling toward the detector and those moving away

from it. Commonly the time available to study a molecule will be limited to a few milliseconds, which gives a limit of a few kHz on the width of the spectral lines observed. Given these considerations it would naturally be beneficial to cool the molecules and increase the interaction time and thus the resolution of the spectra.

Precision laser tools are in development to make such advances in spectroscopy based on samples of cold molecules. This could allow for coherent control of the production processes, excitation pathways, spatial confinement, coupling to the environment and sensitive trace molecule detections. In fact cold molecules have been used in collision and chemical reaction studies [10, 11]. This precision control in both external and internal degrees of freedom allows for an assessment of some of the most fundamental molecular interactions. In turn this will provide an insight into more complex molecular processes.

1.2.3 Variation in Fundamental Constants

With the potential to perform high resolution spectroscopy, high precision measurements can be made. This is particularly prevalent as a concept as there is some evidence to suggest that fundamental constants may vary, in particular the fine-structure constant α [12] and the proton to electron mass ratio $\mu = m_p/m_e$ [13–16]. Atomic clocks have been used to set limits on the α variations, but atoms tend to lack transitions that can show variations in μ. However for molecules, if μ changes, the vibrational (and rotational) energy levels of molecules move relative to their electronic potentials. This has a greater effect on the moderately bound vibrational levels at intermediate inter-nuclear distances than the stronger (near potential minimum) or weak bound levels [15, 16]. This potentially can allow for accurate determinations of $\Delta\mu/\mu$ by using the least sensitive levels as frequency anchors.

The $J = 3/2$ Λ-doublet of OH [12] is at the focus of significant astrophysical research because it can be used to measure the variation of the fine-structure constant and electron mass ratio by comparing the energy levels of cosmological and Earth-bound OH molecules [17–19]. In order to accurately make this comparison, more precise

measurements of these transition frequencies need to be made in order to match the high resolution radio telescope data. Such precise measurements can be performed using ultracold molecules.

More recently there have been some concerted efforts in this field to perform measurements on the electron's electric dipole moment using cold YbF molecules [20,21]. This entailed measuring the interaction energy between the electric dipole moment of the ^{174}YbF molecule and an applied electric field which was interpreted as the interaction energy between the electron electric dipole moment and an effective electric field. This was achieved using a specialised pulsed molecular beam experiment as shown in Fig. 1.2. For this experiment pulses of YbF are emitted by a specialised source [22] with the molecules occupying the $F = 0$ and $F = 1$ hyperfine levels of the ground state. The $F = 1$ population is then emptied out so that the population is state specific. These molecules are then excited from $|F, m_F\rangle = |0, 0\rangle$ to the state $\frac{1}{\sqrt{2}}(|1, +1\rangle + |1, -1\rangle)$ (where m_F is the component of the total angular momentum along the z-axis). These molecules then evolve freely as they pass along the electric field plates with a phase difference forming between the components on account of the static electric field. From this phase difference the electron dipole moment can be extracted.

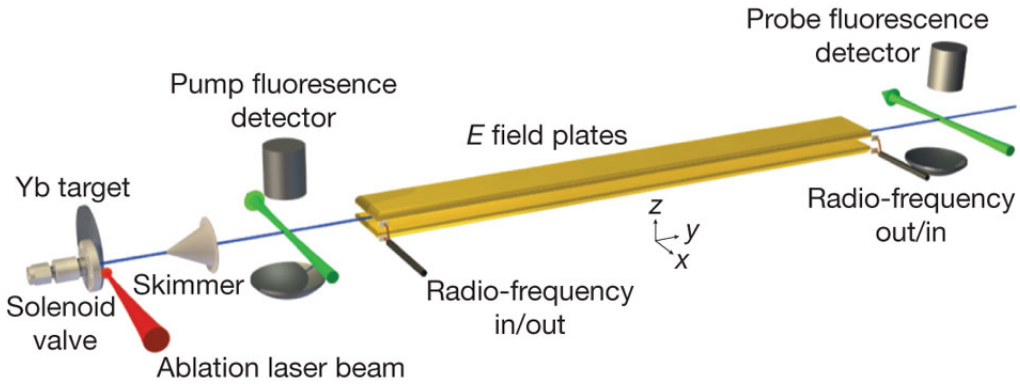

Fig. 1.2 Schematic diagram of pulsed molecular beam apparatus for YbF measurements of the electron dipole moment (taken from [20]).

This technique was able to obtain an upper limit of $|d_e| < 10.5 \times 10^{-28}$ e cm with a 90% confidence. This indicates that the electron is spherical and goes some way to exploring the validity of the current theoretical models of particle physics.

The main barrier to further exploration at this stage is the sensitivity of the equipment and issues of noise so it is very possible that future measurements may give more precise values of the electron dipole moment. In the event that these measurements can be made it would not only go some way to identifying any variations in the fundamental constants, but also give clarification to certain models of particle physics. Specifically, the existence of an electron electric dipole moment greater than 10.5×10^{-38} e cm would contradict the standard model of elementary particle physics as a violation of both parity invariance and time reversal invariance.

1.2.4 Quantum Information Processing

According to Moore's Law, the processing power of computers doubles every 18 months [23]. In order to accommodate this, the size of transistors has become increasingly smaller and, with the current rate of progress, they will soon reach atomic scales. At this scale quantum mechanical effects will impede the operation of the transistor, this is known as the quantum limit. To combat this it has been proposed to use quantum mechanical systems for information processing. The advantage of this being that whereas classical system code data in the form of 'bits' which are either 0 or 1, quantum systems use 'qubits' which are a superposition of both. This can potentially allow for parallel processes to be performed more efficiently and, through use of specialised algorithms [24], speed up information processing.

Polar ultracold molecules have many properties which make them viable candidates for use in quantum information processing. As with atomic systems, molecules have complex internal state structures including long lived internal states, which can be used for encoding of quantum information. In particular the large electric dipole moment associated with rotational structure in polar molecules provides an avenue for quantum control greater than what is viable in atoms. These electric dipole moments can be manipulated with microwave frequency electric fields which can be controlled to a high precision [7]. Additionally, the electric dipole-dipole interaction is both long ranged and strong, which means that it is possible to couple the internal states of molecules even at moderate distances. This gives a potential

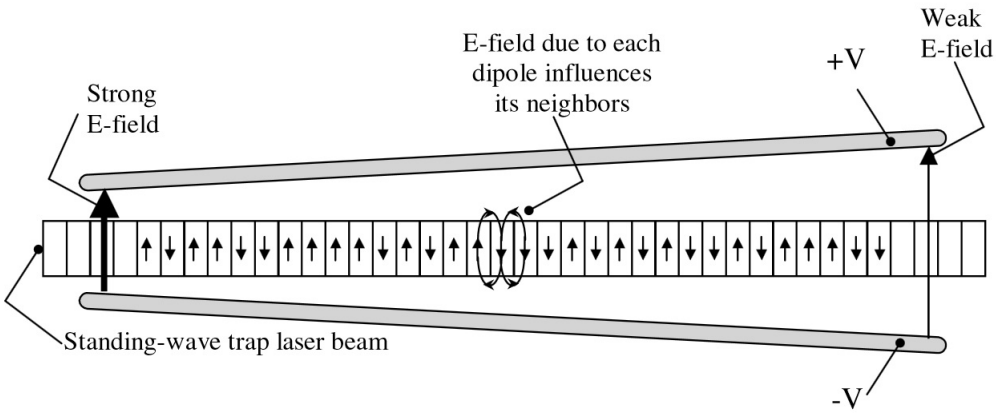

Fig. 1.3 Schematic of polar molecule quantum computer taken from [28]. In this qubit states 0 or 1 correspond to up or down relative to the applied field.

route towards scaling to large networks of coupled qubits. In addition to this, the rich internal structure of the molecules may make it possible to store more than one bit of quantum information in each molecule [25–27].

There have been some potential systems devised that utilise ultracold polar molecules as qubits where the molecules are held in an optical lattice along an electric field gradient [28]. In this scenario (as illustrated in Fig. 1.3) molecules with a simple rigid rotor structure are used and qubits are encoded into the two lowest rotational energy levels encoded as the qubits (with $|0\rangle$ being encoded as the lowest energy level of the two). For a single qubit superpositions of $|0\rangle$ and $|1\rangle$ can be prepared by applying microwave pulses with frequency tuned to the resonance with energy needed to flip the dipole.

This system illustrates some of the key advantages of using molecular qubits. First, neutral polar molecules can potentially be assembled in large numbers at high density into regular structures, this provides potential for scalability. Additionally the long range nature of the dipole interactions means that qubits can be held at some distance and still interact. Additionally, unlike systems that use Rydberg atoms in a similar manner, this system will have longer decoherence time allowing more processes to be performed before the qubits collapse. Further the manipulation of the individual qubits can easily be performed allowing for a greater control of the system.

1.2.5 Quantum Simulation

Although quantum mechanical simulation techniques using classical computers are becoming ever more advanced, there are certain processes that are significantly problematic for classical computers to perform. On account of this limitation it has been proposed to use ultracold molecules to form a quantum simulator. The principle of the quantum simulator is that the molecules are used to directly engineer a system whose Hamiltonian matches that of a fully quantum many body system whose properties are not fully understood. The long range and anisotropic dipole interactions between molecules in an optical lattice provides an effective medium for this purpose. Different manifestations of this idea can be used to simulate a number of condensed matter models [29–31].

The principle behind the quantum simulator was first proposed by Feynman in 1982 [32] and in many ways is an expansion upon the ideas of quantum information processing. In essence a quantum computer could be considered to be a quantum simulator that can be applied to a number of different quantum simulators. However the difficulty lies in making such a system universal so that information can be encoded into it. An alternative for simulating a specific system is to build a quantum simulator. For instance, if we wish to simulate the properties of a solid a simulator could be constructed using an optical lattice of cold polar molecules in an array. As the magnetic and electric dipole interactions of the molecules are (in certain cases) significantly stronger than the interactions of atoms in a solid, changes in the optical lattice structure are easier to measure; and hence one can simulate the properties of the solid.

In order for this to be realised ultracold molecules need to be used in order to ensure that the molecules remain in the trap for a long enough period of time to perform the desired simulations. Additionally a large number density is required so that enough molecules can be held to effectively simulate the desired systems. However if quantum simulation can be achieved it could form the precursor for a universal quantum computer.

1.3 Production of cold molecules

Broadly speaking the methods of producing ultracold molecules fall into two categories: direct and indirect cooling. Direct cooling involves cooling intact molecules whereas indirect cooling combines ultracold atoms to form an ultracold molecule. For the purposes of producing ultracold molecules we are presently concerned with the production of diatomic molecules, as triatomic molecules or higher have a greater number of rotational and vibrational degrees of freedom and hence it becomes harder to reduce these to ultacold temperatures.

1.3.1 Direct Cooling

As stated above direct cooling actively attempts to make molecules colder without changing the molecule. This can be a problematic process as molecules have vibrational and rotational degrees of freedom in addition to the translational freedom of atoms. This means that in order to reduce the temperature of molecules the vibrational and rotational energies need to be reduced as well as the translation of the molecule as a whole. There are many methods by which this can be achieved some of which are outlined below.

Supersonic Expansion

A relatively simple method to cool a gas is to let it expand from a high pressure system through a nozzle into vacuum. Let us consider a container with high pressure gas and a small hole through which the molecules can emerge into the vacuum. While in the container the molecules will be able to travel a certain distance before they collide with another molecule, and the average of this distance is the mean free path of the gas. If the hole in the container is much smaller than the mean free path of the gas the velocity distribution will not be disturbed inside the container and will remain the same as the beam leaves the container. This would be an effusive molecular beam.

If the orifice is much larger than the mean free path, the molecules escaping the container will collide more frequently. At the hole molecules will experience a net force coming from collisions with molecules still in the container which will push them out. Due to this the speed distribution of the molecules in the beam will be different than within the chamber as the faster molecules will collide with slower molecules flying ahead which will increase the average velocity and reduce the velocity distribution. This narrower velocity distribution corresponds to a lower temperature (see Fig. 1.4).

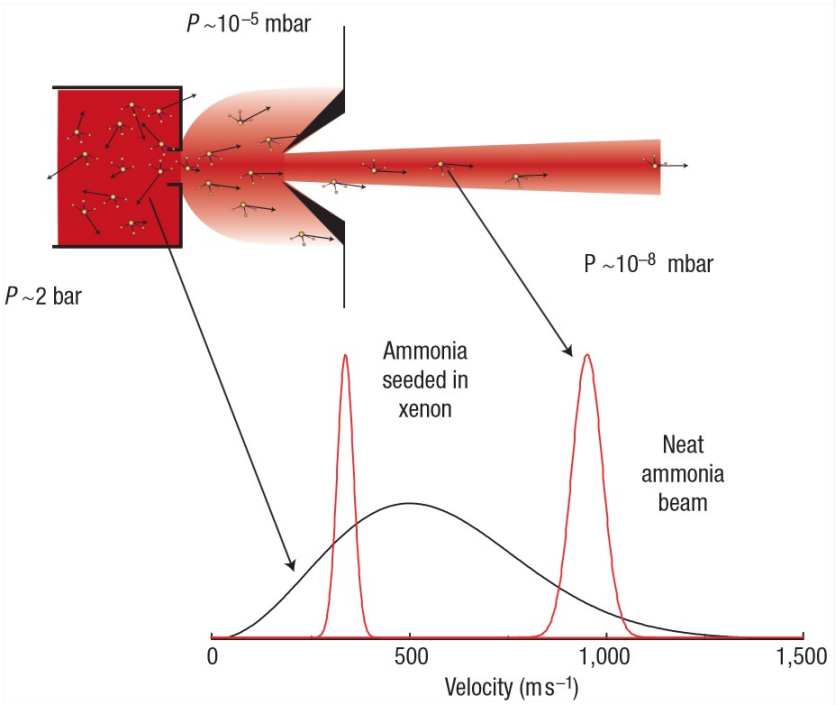

Fig. 1.4 Schematic representation of supersonic expansion of ammonia taken from [33]. The high pressure gas is expanded through a small hole into vacuum. Also shown is the velocity distribution both in the chamber and in the supersonic beam. Seeding the ammonia in a xenon carrier gas greatly reduces the mean velocity.

This process boils down to the transformation of the random thermal motion of the high pressure gas into a directed translational motion. During this the thermal energy per molecule is largely converted into kinetic energy, which implies a significant reduction in the translational temperature in the moving frame of the molecular beam. However, in practice finite collision cross sections and the formation of clusters limit the temperature as the beam density drops with r^{-2} so there is a limit to the number of cooling collisions that can occur.

Using this method highly directional molecular beams can be obtained when combined with a skimmer. Skimmers are cone-shaped metal pieces with a small orifice at the apex so that when the molecular beam passes through it, molecules with higher transverse velocities are removed. Additionally the velocity and velocity distribution can be controlled by mixing a carrier gas into the molecular beam. This is because the collisions between the primary gas molecules and the carrier gas molecules will be different than between the primary gas ones themselves. Noble gases are often used as the carrier due to their non-reactive nature and can also reduce the aforementioned cluster formation (although this is not the case with the more polarisable noble gases such as Xe). This is due to the fact that noble gases only cluster at very low temperatures and so can act as a heat sink during the expansion. It is common practice to use a mixture of a small percentage of the molecules of interest in the carrier gas. By this method translational temperatures below 1 K and rotational temperatures below 5 K can be obtained; along with vibrational temperatures of around 50 K [9]. The terminal velocity of the molecular beam with this method is usually in the supersonic region and is altered by using different mixtures of carrier gas.

Kinematic Cooling

As a supplement to supersonic expansion, kinematic cooling can be used to further cool molecules in a molecular beam. Essentially this technique involves crossing atomic and molecular beams and using the collisions to reduce the velocity in the laboratory frame. The molecular and atomic beams are tuned such that when the molecules and atoms the scattering process brings the molecules to rest in the lab frame. Further, if the collision is elastic and the species are of approximately the same mass, the scattered molecule will be in its rovibrational ground state.

The earliest experiments with this method used supersonically cooled beams of Ar and NO and produced NO molecules with a temperature of $\sim$ 440 mK [35] via inelastic collisions. However secondary collisions of the cooled molecules with the supersonic beams make these conditions difficult to maintain. On account of this

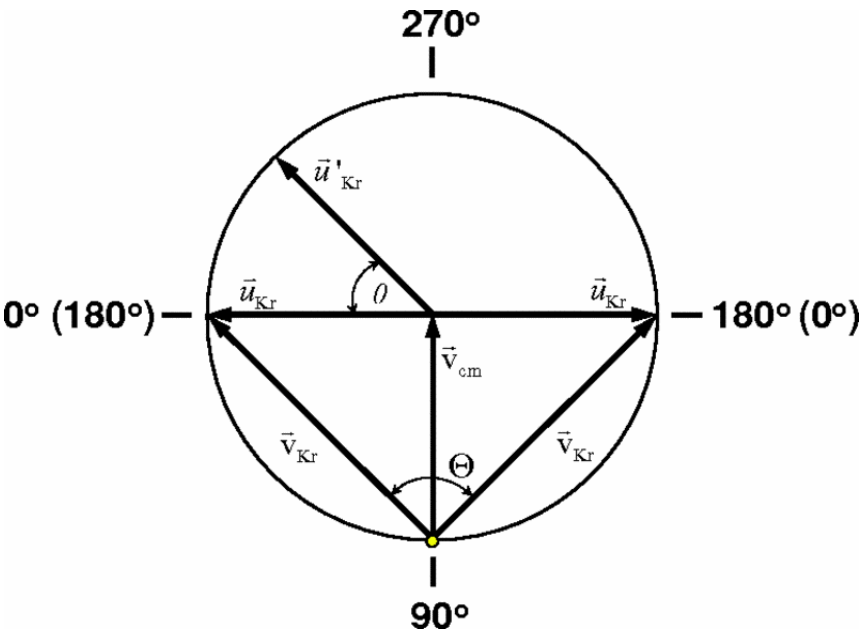

Fig. 1.5 Newton Diagram illustrating the process of kinematic cooling using cross beams of Kr (taken from [34]). The fiure is drawn for atoms with identical masses and identical velocities colliding at a laboratory frame angle of 90° with the most slowly scattered atoms stationary in the lab frame.

there has been further developments with this technique [36,37], which has also been expanded to other species [34,38].

The primary advantage of this method is that it can potentially be applied to any molecules as it only relies on the quantum states and momenta on the species in question. However the process is experimentally difficult due to the reliance on collimated supersonic beams at sensitive angles.

Laser Cooling

One of the more prominent cooling techniques of recent years has been laser cooling. This process involves cooling atoms by many consecutive absorption-emission cycles which results in a significant momentum transfer from photons in the laser beam to the atoms or molecules. More specifically, laser beams are directed at an atom or molecule such that the photons of the laser can be absorbed by it. The momentum of these absorbed photons counteract the translational motion of the target atoms/molecules thus slowing them down. Generally the method used to perform this process also makes use of the Doppler effect. If the slowing laser is tuned to

just below a specific absorption peak of the atoms/molecules, the atoms/molecules moving into the laser will encounter photons which are Doppler shifted onto the absorption peak and therefore they are slowed down by the laser. This cycle of absorption and emission continues until the target atoms/molecules reach a velocity such that the incoming light is no longer Doppler-shifted into an absorption peak.

These techniques have been shown to cool atoms to temperatures below 1 mK at a density of 10^{10} atoms cm^{-3}. However there are limitations as to what species this technique can be applied to as a closed cyclic transition is required so that the absorption of a photon is always followed by a spontaneous decay to the initial state. This can make the process extremely problematic for molecules as their vibrational and rotational degrees of freedom mean that they have far more energy levels and decay routes that can lead them out of the cooling cycle. On account of this, when the molecule is excited by the incoming photon, there are a number of states that the excited state can decay to (via spontaneous emission). As these states are not at the same energy as the initial state, the incoming photon is no longer resonant with the given transition and hence the molecule in this state cannot be cooled by the same laser.

Despite these difficulties there have been some instances where such optical methods have been used to effectively cool molecules. Notably variations of this technique have been used in the rovibrational cooling of Cs_2 [39], the optical cooling of SrF [40] and the rotational cooling of molecular ions [41]. More recently a variation of this technique has been used to slow a molecular beam of SrF from a buffer gas source [42] as well as for CaF [43]. In both cases the issue of spontaneous decay of the molecules out of the cooling cycle was overcome by using a secondary 'repump' laser to re-excite the molecules into the initially excited state. A diagrammatic illustration of the scheme used in [43] is shown in Fig. 1.6.

In addition to the experimental findings, there have been a number of theoretical investigations into the feasibility of this method. Some of the species simulated include BeCl and BeBr [44], C_2^- [45], MgCl and MgBr [46], which show good prospects for use in laser cooling. It is important to note that the molecules that have been suc-

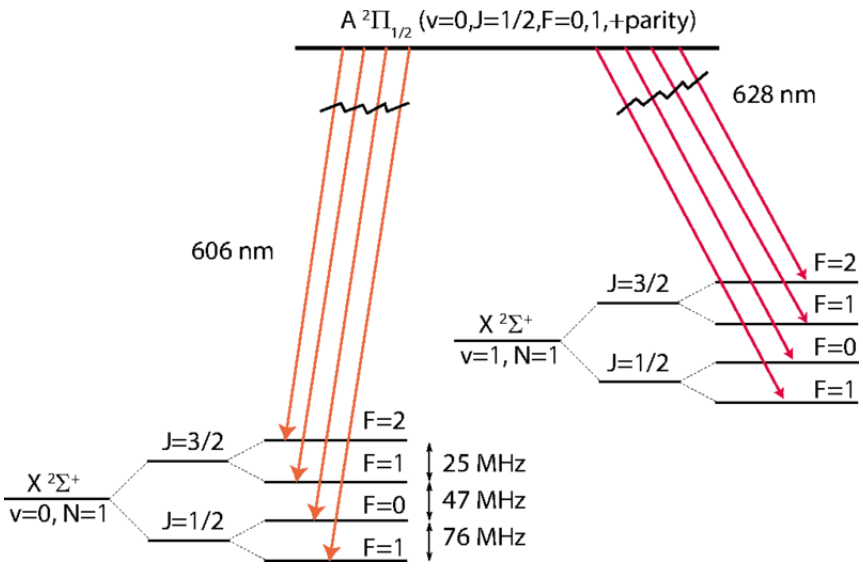

Fig. 1.6 Illustration of the transitions used for the laser cooling of CaF from [43]. The main cooling cycle takes place on the $A\,(v'=0) \leftrightarrow X\,(v''=0)$ transition while the repump laser acts on the $A\,(v'=0) \leftrightarrow X\,(v''=1)$ transition.

cessfully laser cooled possess what is known as a 'diagonal' Franck-Condon factor. In practice this means that when excited to the desired excited state the spontaneous emission from the molecule predominantly results in a decay back to the ground state. On the whole this technique remains somewhat in its infancy but there is good potential looking forward for further expansion.

Sisyphus Cooling

The more recently developed method of Sisyphus cooling offers an alternative approach to optically cooling molecules held in an electric trap. A schematic illustration of this method is given in in Fig. 1.7. Initially the target molecules are held in an electric trap with two distinct regions (high-field and low-field). Molecules in strong low-field-seeking states (which we shall refer to as $|s\rangle$) will experience a different potential in the trap to those in weaker low-field-seeking states (which we shall refer to as $|w\rangle$). So, as shown in Fig. 1.7 as a molecule in the $|s\rangle$ state moves into the high-field region it is driven into the weaker $|w\rangle$ which then moves back the low-field region due to the favourable potential. This can then be driven to an excited state $|e\rangle$ which will spontaneously decay back to the $|s\rangle$ state, restarting the cycle.

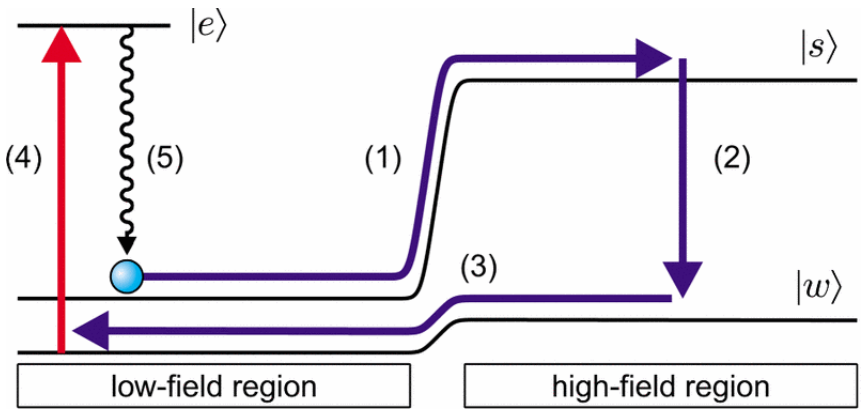

Fig. 1.7 Diagrammatic representation of Sisyphus cooling taken from [47]. When a molecule in the strong low-field-seeking state $|s\rangle$ diffuses into the high field region it is driven to the weaker low-field-seeking state $|w\rangle$. This then moves back to the low-field region where the molecule is excited to the state $|e\rangle$. This decays spontaneously back to $|s\rangle$ and the cycle repeats. As the spontaneous decay is irreversible the cycling process is unidirectional.

This Sisyphus technique has been demonstrated using CH_3F molecules which have had the temperature reduced by a factor of 13.5 [48]. It has also been successfully used to produce an ensemble of 3×10^5 formaldehyde molecules with a temperature of approx 420 µK populating a single rotational state with more than 80% purity [49]. Additionally there have been a number of theoretical studies for potential schemes of this type [50, 51].

When directly compared to more traditional Doppler-based laser cooling methods, Sisyphus cooling has some distinct advantages. As an infra-red laser is used to change the trapped molecules' vibrational state, this gives the option of using high powered and narrow band lasers, which are difficult to find for the electronic transitions used in Doppler-based methods. Additionally there is no reliance on favourable Franck-Condon factors to facilitate the cooling process. However, Sisyphus cooling can only cool to low-field seeking states which is rarely the case for ground state molecules, therefore further cooling would be required to reach significantly lower temperatures.

Buffer Gas Cooling

One of the more versatile methods for the preparation of cold molecules is that of buffer-gas cooling. The basic principle of this method is that the molecules are enveloped in a buffer-gas of cryogenically cooled atoms (often helium) and via collisions with the buffer gas the molecules lose momentum and become colder. This method has been used on a variety of atomic and molecular species such as CaH [52], CaF [53], NH [54], Cr [55], Mn and N [7]. As result of this method the molecules can reach a temperature of around 1 K with molecular densities that can exceed $10^9\,\mathrm{cm}^{-3}$. Cold molecules produced by this method are sometimes held in a magnetic trap as this allows the opportunity to study different aspects of the cooling process such as the dynamics between molecules and He atoms [56].

Another direction for buffer gas cooling is the creation of cold molecular beams. For this process the molecules are introduced into a chamber containing the buffer gas. After a sufficient number of collisions with the buffer gas the molecules are cooled both rotationally and translationally and the mixture is allowed to escape the chamber via an orifice. Electric or magnetic field guides are placed at the exit of the chamber so that only molecules that are moving sufficiently slowly will be guided to the intended destination.

Sympathetic Cooling

A more recently developing method for cold molecule production is that of sympathetic cooling. In many ways this has similar operating principles to buffer gas cooling with the target molecule being cooled by interaction with colder atoms to ultimately reach an equilibrium. The primary difference for sympathetic cooling is that during the process the "buffer gas" atoms are themselves also being continuously cooled via laser cooling. This ultimately leads to lower temperatures than can be achieved through buffer gas cooling as the constant reduction in temperature of the cooling atoms ultimately leads to lower temperatures. An illustrative analogy for a comparison of the methods would be that buffer gas cooling is like putting an

ice cube in a drink whereas sympathetic cooling is like having a constant flow of ice into it.

One of the earliest realisations of this method was in the sympathetic cooling of trapped $^{198}Hg^+$ in a Penning ion trap with laser-cooled $^{9}Be^+$ ions, which reached temperatures below 1 K [57]. This early experiment served as a good demonstration of the effectiveness of sympathetic cooling as well as illustrating some of the characteristics of a cold, magnetically confined, two-species plasma. Another prominent experiment with this technique performed sympathetic cooling between two spin states of ^{87}Rb [58]. In this case a double magneto-optic trap and a so-called Ioffe-type trap was used to create condensates of the $|F = 2, m = 2\rangle$ or $|F = 1, m = -1\rangle$ states which were then overlapped causing sympathetic cooling of the former via thermal contact with the evaporatively cooled latter. From here the method has been applied to a number of atomic species with a variety of different techniques including (but not limited to) the cooling of ^{41}K using evaporatively cooled ^{87}Rb [59], the cooling of ^{6}Li in a thermal bath of ^{23}Na [60], the cooling of ^{6}Li using the forced evaporation of ^{7}Li [61], the cooling of optically trapped ^{7}Li atoms using trapped ^{133}Cs atoms [62] and the cooling of ^{133}Cs via elastic collisions with ^{87}Rb [63].

The application of this technique to molecules is a more recent development with a number of theoretical models produced [64–67]. In terms of experimental work, the field is still developing with some promising results from the cooling of molecular hydrogen ions with laser cooled beryllium [68], a variety of diatomic and triatomic molecular ions [69] as well as larger organic molecules which were cooled by interaction with laser-cooled barium ions [70] and more recently the cooling of $^{40}CaH^+$ with co-trapped $^{40}Ca^+$ ions.

Stark and Zeeman Deceleration

As one of the main points of interest in ultracold molecules is their permanent magnetic and electric dipoles it seems natural to use this property as a means to manipulate them. This is the idea behind both the Stark and Zeeman deceleration

techniques.

In both cases a narrow pulse of molecules is slowed by using an electric or magnetic field gradient to oppose the motion of the molecules. If we take the example of Stark deceleration as illustrated in Fig. 1.8, when entering an electric field molecules the with an electric dipole moment will gain Stark energy at the cost of kinetic energy [71]. To prevent the molecules regaining the kinetic energy the electric field is switched to the opposite polarity. If the molecules are directed through multiple pulsed electric fields such as this they can effectively be slowed down. The same principles can also apply for the magnetic dipole moment of a molecule, which gives rise to Zeeman deceleration [72].

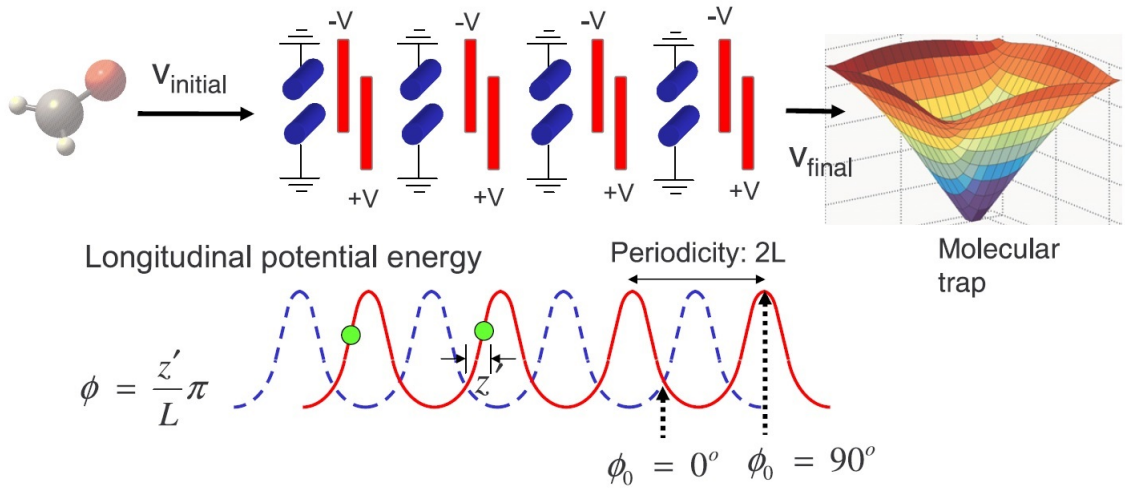

Fig. 1.8 Schematic for Stark deceleration taken from [7]. As the molecules enter the electric field they will gain Stark energy at the cost of kinetic energy as shown by the red curve. The electric potentials are then switched to the dashed blue curve so the molecule is once again at the bottom of a potential well. This process is repeated and the decelerated molecules are often loaded into a molecular trap.

When in an electric or magnetic field the quantum states of a molecule will shift in energy as a result of the Stark and Zeeman effects respectively. These shifts can be positive or negative depending on the alignment of the electric/magnetic dipole relative to the electric/magnetic field. States where the electric/magnetic dipole is aligned with the external field will decrease in energy in higher fields (high-field seeking states) and those where the dipole is aligned opposite to the external field will gain energy in higher fields. As the high field seeking states are lower in energy

the rotational ground state of a molecule is always a high field seeking state.

Given that the high field seeking states tend to be lower in energy it seems that it would be preferable to decelerate these states. However it is often experimentally simpler to decelerate low-field seeking states. In the case of Stark deceleration, the technique has been used to successfully decelerate a number of molecules such as CO [71], OH [73], SO_2 [74], YbF [75] and H_2CO, which have been used in high precision spectroscopy and crossed beam collision experiments. More recent work has shown the successful Stark deceleration of CaF [76] as well as OH radicals, indicating the efficacy of the method for decelerating molecules.

Zeeman deceleration tends to be more difficult than Stark deceleration on account of the requirement for strong magnetic fields that can be switched quickly. In spite of this difficulty there have been some successes in the deceleration of metastable Ne [77, 78], metastable Ar [79], metastable He [80] as well as more recent work in the deceleration of electron-impact-excited metastable He atoms [81]. Applications of this technique to molecular species are forthcoming with O_2 molecules [82], and given the complexity of the apparatus required for these experiments the progress made thus far has been substantial.

1.3.2 Indirect Cooling

Although direct cooling methods are effective at producing ultracold molecules a successful alternative is to assemble them from ultracold atoms. This approach allows for the use of the cooling power of techniques available for atomic species in producing ultracold molecules. It has also been shown that binding can be induced between atoms without significant motional heating [7]. However the internal degrees of freedom of the molecules during and after formation can be problematic. Despite this it seems likely that quantum degenerate gases of molecules can be created with these methods.

One of the main limitations of indirect cooling techniques is that they can only be used to create ultracold molecules with atoms that can be laser cooled and trapped,

which excludes many chemically relevant species. Presently the majority of indirect cooling experiments have been performed with alkali metals, although the use of alkaline earth metals is growing [83].

The first experiments in forming ultracold molecules from laser-cooled atoms was performed using photoassociation (PA). In PA, a laser is tuned to resonance with a transition from the free (scattering) state of the ultracold ground state atoms, to a bound level of the excited (s + p) potential. However, because the photoassociation often results in production of molecules in an excited vibrational state, cooling further into lower vibrational states often requires spontaneous emission; this, in some cases, may lead to the dissociation of the molecule. The initial experiments with this technique focussed on homonuclear molecules [84,85] but were soon followed by experiments with heteronuclear species [86,87].

More recent experiments have utilised Feschbach resonances in order to form ultracold molecules. A Feschbach resonance occurs when a bound molecular state has the same energy as the collision energy of two free atoms in a scattering channel. When the difference in the quantum states of the scattering channel is associated with a difference in magnetic moments, a tunable magnetic field can be used to bring the energies of the quantum states of the atoms and molecules into resonance. By performing this manipulation colliding pairs of atoms can form ultracold molecules; this technique is known as magnetoassociation.

1.3.3 Comparison of Cooling Methods

As many of the aforementioned cooling methods are only applicable to certain species a comprehensive comparison cannot always be made between them. However for the majority of applications of cold molecules it is beneficial to obtain high molecular densities at low temperatures. To make this comparison the methods outlined here are summarised in Table 1.1.

In terms of temperatures, indirect cooling methods tend to reach far lower temperatures than the direct ones. This primarily comes from the advantage that the

Table 1.1 A comparison of the cooling methods outlined in terms of the temperatures (or final velocities) reached and the number of molecules, N, in the sample. Adapted from [88].

Method	Requirements	T or v	N
Kinematic Cooling	Applicable to all	400 mK	No Data
Buffer Gas Cooling	Applicable to all	400 mK	$> 10^8$
Stark Deceleration	A permanent or induced electric dipole moment	5 mK	10^6
Zeeman Deceleration	A permanent or induced magnetic dipole moment	$50\,\mathrm{m\,s^{-1}}$	No Data
Photoassociation	Only applicable to atoms that can be laser cooled	30 µK	2×10^5
Feschbach Resonance	Only applicable to atoms that can be laser cooled	50 nK	$> 10^5$

utilisation of laser cooling the atomic constituents brings. However this is also the drawback of the methods as it fundamentally limits the species that they can be applied to.

If we compare the direct cooling methods, although Stark deceleration reaches the lower temperatures the number densities are also significantly lower. Coupled with this the requirements for the electric/magnetic dipole moment in the cooled species ultimately limits the applicability of these techniques. However, one of the main advantages of the direct cooling methods is that they can potentially be combined, for instance a buffer gas source can be introduced into a Stark decelerator, thus providing the benefits of both techniques.

1.4 Molecule detection methods

When using the above cooling techniques it is important to be able to establish how successful they are by measuring the molecules produced. Specifically, we wish to be able to identify the ultracold molecules as well as measure their temperature and number density. In this regard there are a number of different spectroscopic techniques which can be used to identify them based upon their quantum mechanical properties. Additionally, the use of different forms of mass spectrometry can also be used to characterise different molecules. The temperature of the molecules can also be measured using velocity map imaging techniques, which can extrapolate the temperature of the molecules from their velocities. However measuring the number density of the molecules produced can become problematic requiring calibration based on, for instance, the intensity of photons emitted from the molecules. There are some methods that can be used to measure the number density directly, notably the employment of a cavity and the use of cavity ring down spectroscopy. For the sake of this work I will be discussing the techniques used in this project and by no means is this all-inclusive of every measurement method available.

1.4.1 Resonance Enhanced Multi-Photon Ionisation

Resonance-enhanced multiphoton ionisation (REMPI) is a spectroscopic technique that is often used for atoms and small molecules and can in some cases also be used for large molecules. The process involves using a tunable laser to perform a multiphoton process to ionise the atom or molecule. Initially the laser is tuned to a frequency such that a single or multiphoton excitation will excite the atom or molecule into an intermediate state. When in this intermediate state the molecule is further excited above the ionisation potential, thus ionising the atom or molecule. Additionally, the nature of this process means that the excitation to the intermediate state is dependent on the initial state of the molecule. Thus, the quantum state of the atom/molecule being ionised can be determined from the REMPI transition.

This process can be performed with different numbers of photons being absorbed by

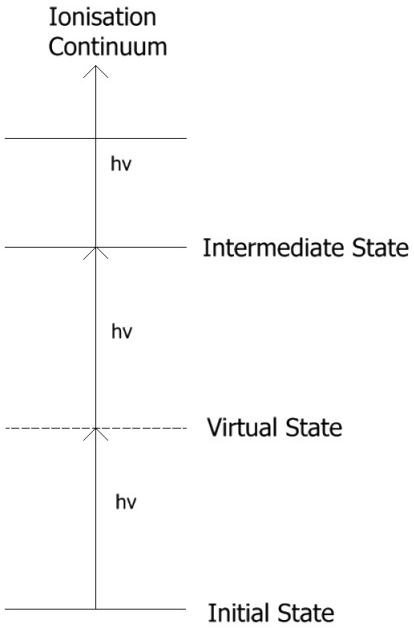

Fig. 1.9 Schematic of the transitions involved in a 2+1 REMPI scheme.

the species. However, the more photons required for the process the more difficult it becomes as each species has a finite absorption cross-section. One such REMPI configuration is the 2 + 1 scheme as shown in Fig. 1.9. Here two photons are used for the initial excitation and the third ionises the species. The viability of this process and the number of photons required will naturally vary depending on the energy level differences in the species used and the more photons required the higher the laser power will need to be in order for this to be efficient. Another variation on this process involves the use of two separate excitation lasers, one to bring the atom/molecule to the intermediate state (via however many photon absorptions are required to do this) and another to ionise the species. The advantage of this is that it can allow for the ionisation/measurement of species in states that would be difficult to ionise in other circumstances, as well as allow for ionisation on or near the ionisation threshold.

As REMPI requires specific wavelengths to excite the molecules to the intermediate states, high intensity tunable lasers tend to be used for the excitation. Additionally once the molecules are ionised by the REMPI process there needs to be some method by which the ions can be measured. One such method is to use a combination of

electrodes and a microchannel plate (MCP). In this scenario when the ions are produced they are accelerated by a set of electrodes (known as ion optics) to an MCP which can detect the ion.

Velocity-Mapped Ion Imaging

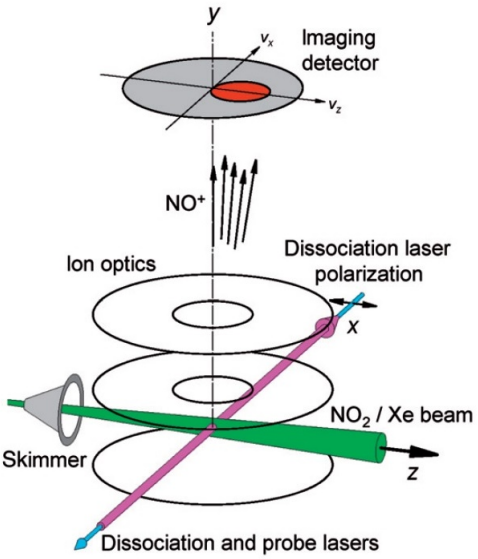

Fig. 1.10 Velocity-mapped ion-imaging set up taken from [89]. Schematic diagram of the experiment. The molecules in the molecular beam are ionised and accelerated by a set of ion optics towards a position sensitive detector to image the ions.

One of the methods that can be used to perform measurements on ions produced by REMPI is that of velocity map ion imaging (VMI). The idea behind this is that the velocities of species that are moving in a specific plane can be measured by deflecting it along a path that is perpendicular to that plane. This can give a two dimensional map of the velocities of the species in this plane. This method was first demonstrated in 1997 [90] and has been used extensively since [34, 37, 89, 91, 92].

An example of such a VMI set up is shown in Fig. 1.10[1]. In this case NO molecules were ionised by a pulsed dye laser using a 1+1 REMPI scheme. The resulting NO^+ ions were accelerated by an electrostatic field generated by a set of ion optics towards a position sensitive imaging detector which consists of a pair of microchannel plates, a phosphorescent screen and a CCD camera. The ion lens system was designed and

[1] This setup was used in previous photostop experiments which will be addressed in Chapter 2

operated such that the velocity of the original NO molecule was mapped onto a unique position on the detector.

In order for this to provide a measure of the velocity of the NO molecules in the laboratory frame, the velocity origin (i.e. the position on the detector where (v_z, v_x) = (0,0) $\mathrm{m\,s^{-1}}$) needs to be found. In the aforementioned case this was achieved by recording an ion image of thermal NO bled into the vacuum chamber. Two one-dimensional Maxwell-Boltzmann distributions of the form

$$f(v_x) \propto \exp\left(-\frac{m_{\mathrm{NO}} v_x^2}{2kT}\right), \tag{1.2}$$

were fitted to the ion image in the v_x and v_y and its centre located.

1.4.2 Laser Induced Fluorescence

Another highly useful and well established form of spectroscopy is laser-induced fluorescence (LIF) [93, 94]. In this method the examined species is first excited with a laser, then the excited species will fluoresce emitting light isotropically at a wavelength longer than (or equal to) the excitation wavelength; it is this emitted light that is measured.

The primary advantage of this technique (when compared to other spectroscopic techniques) is that as the probing wavelength is tuned to the molecule in question, it is virtually background free, which means it can be used for the detection of very low concentrations in confined volumes. Additionally, the fact that the signal is background free means that it can be used in scenarios that range from requiring single photon detection to saturation of measurement equipment.

The applicability of this technique will vary depending upon the species used or more specifically the properties of the excited state. If the fluorescence lifetime of the state is short, stray light from the incident laser needs to be controlled e.g. with an optical filter. For longer fluorescence lifetimes stray light can be discriminated against by time-gating the signal. For some molecules the upper state may be predissociative,

which occurs when the potential curve of the excited state overlaps with an unbound state. In this scenario processes such as intersystem crossing (ISC) may occur and the molecule will transfer to the unbound state and dissociate. This, along with the current capabilities of laser technology (i.e. what wavelengths can be reached), may make this technique inappropriate for certain species.

As the emitted light is often isotropic LIF can potentially be used to generate spatial images of the fluorescence, which is a distinct advantage over other forms of absorption spectroscopy. Additionally, with a well designed light detection system, a high signal-to-noise ratio for the fluorescence is easily achievable, allowing for measurements of small numbers of molecules. Additionally the fact that initial excitation needs to be tuned to specific transitions in a molecule means that to some degree it can be used to distinguish between different species.

1.4.3 Cavity Ring-Down Spectroscopy

Cavity ring-down spectroscopy (CRDS) is a direct absorption technique which can be significantly more sensitive than conventional absorption techniques. Instead of measuring the magnitude of absorption from a sample this technique measures the rate of absorption. The sample is placed in an optical cavity consisting of two highly reflective mirrors. A short laser pulse is coupled into the cavity and the light is reflected back and forth between the mirrors. With each pass some light leaks out of the cavity. The amount of light that leaks out of the cavity will decay over time and it is the rate of this decay that is measured. This allows for the rate of absorption to be measured so that the more the sample absorbs the faster the decay of light in the cavity[2]. This is a relatively simple technique that allows for accurate measurements to be taken with little requirement for complex equipment. Further, the fact that the absorption is determined from the decay of the signal as opposed to the intensity it means that it is independent of pulse to pulse fluctuations of the laser. Additionally, the effective absorption pathlength can be very long, while the sample volume is small.

[2] The full mathematical description of this will be explored in section 3.8.1

The precursor to this technique was a method for the measurement of the reflectance of mirror coatings by Herbelin *et al.* [95] and Anderson *et al.* [96]. In 1988 O'Keefe and Deacon first demonstrated the sensitivity of this technique by recording the weak $b^1\Sigma_g^+(v = 1, 2) \leftarrow X^3\Sigma_g^-(v = 0)$ bands of molecular oxygen [97]. Since then it has been repeatedly shown to be a powerful spectroscopic technique for measurements of either strong absorptions of species present in trace amounts or weak absorptions of abundant species among other applications [98].

Although CRDS is significantly more sensitive than standard absorption spectroscopy techniques, in many circumstances it cannot compete with background-free detection techniques such as LIF or REMPI. However CRDS can be applied to species with excited states that do not fluoresce or cannot or species that are difficult to ionise using a REMPI process. Another major advantage is that CRDS can be used to extract quantitative absolute concentration data, which is difficult with the other methods.

1.5 Objectives of photostop project

As a part of the larger collaboration between Imperial College and Durham University known as the MicroKelvin molecules in a Quantum Array (MMQA) grant for the production of cold molecules for use in a quantum simulator, the photostop project is focussed on developing a novel way of producing cold molecules. The initial stage of this will be to trap the cold molecules produced in a permanent magnetic trap so that further cooling can be facilitated. As will be shown in Chapter 2, the demonstration of this trapping will require the development and application of highly sensitive detection apparatus. The crux of this project is the development of this measurement apparatus for photostop as well as the initial application of it to the photostop measurements.

2. PRINCIPLES OF PHOTOSTOP

2.1 The Photostop Method

Photostop is a slowing method for producing cold species based on the photodissociation of larger molecules. This technique requires a molecular beam of larger molecules (which shall be referred to as the parent molecule) with a narrow velocity distribution centred on a well defined average velocity. When the parent molecules are photodissociated, the fragments produced will recoil relative to the centre-of-mass (COM) of the precursor. In the lab frame this results in a velocity given by the difference between the recoil from the COM and the velocity of the COM (see Fig. 2.1(a)). If the molecular beam speed matches the recoil velocity of the desired fragment from the COM, a portion of the molecular fragments will have an effective velocity in the lab frame of zero bringing the molecule to a standstill and hence "stopping" them.

With this technique the key is to tune the recoil velocity from the dissociation to match the forward velocity of the molecular beam. Although the molecular beam speed itself can be controlled by the use of different carrier gases (see 1.3.1), the final velocity of the fragments is also determined by the photodissociation process. If we take the photostop of H_2S to produce SH as an example, photon energies, $h\nu$, exceeding the dissociation energy, D_0, of the HS-H bond will cause the molecule to fragment (see Fig. 2.1(b)). The excess energy, $E_{excess} = h\nu - D_0$, is distributed between the kinetic and internal energies of the fragments in proportions determined by the photodissociation dynamics. For fragments that are formed in a given combination of states, the total internal energy of the fragments, $E_{\mathrm{int(frag)}}$, is fixed and

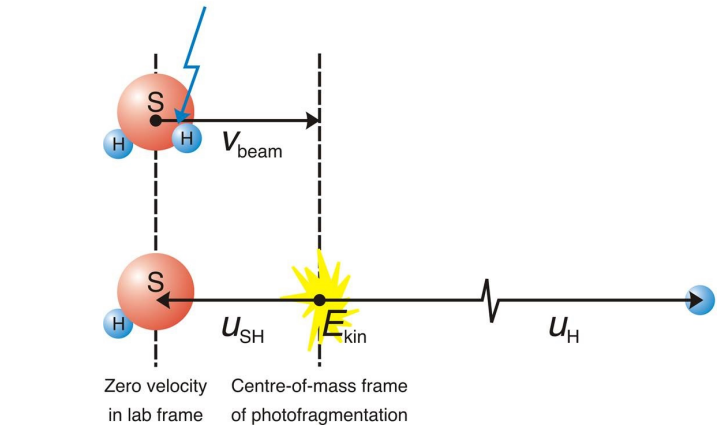

(a)

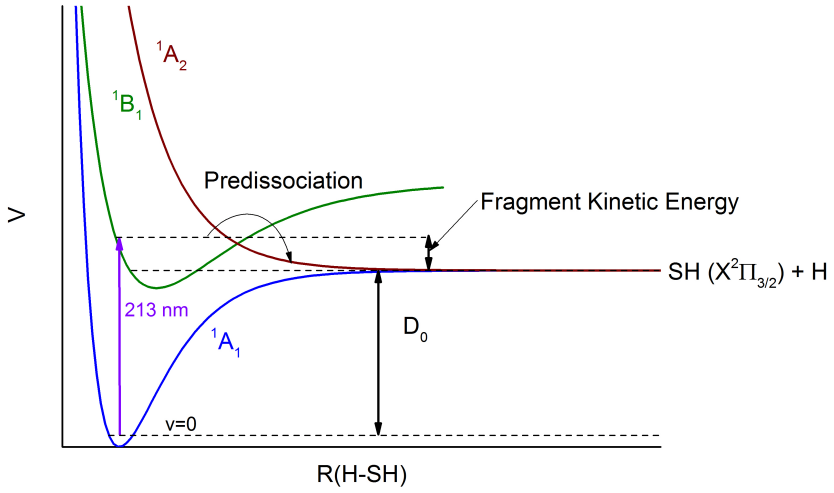

(b)

Fig. 2.1 Schematic outline of photostop technique using a H_2S parent molecule (a) along with an energy level representation of the dissociation mechanism (b). The recoil velocity of the SH fragments as a result of the photodissociation cancels out the velocity of the molecular beam, resulting in zero velocity in the laboratory frame.

the total kinetic energy, E_{kin}, is governed entirely by the photon energy

$$E_{\text{kin}} = E_{\text{kin}}(\text{SH}) + E_{\text{kin}}(\text{H}) = h\nu - D_0 - E_{\text{int(frag)}} + (E_{\text{int(H}_2\text{S)}}), \tag{2.1}$$

where E_{kin}(frag) and E_{kin}(H) are the kinetic energies of the SH and fragments respectively and $E_{\text{int(H}_2\text{S)}}$ is the internal energy of the H_2S at the point of dissociation. It should be noted that the $E_{\text{int(H}_2\text{S)}}$ can often be disregarded for these experiments. This is because the ultimate effect of different internal energies of the H_2S molecules would result in a distribution of different recoil velocities. However in practical

terms it is often the case (as it is for this experiment with H_2S) that the spread of the velocity distribution of the molecular beam far exceeds this and so this term can be disregarded. By conservation of momentum, in the COM frame of the photodissociation, the velocities of the fragments are given by

$$u_{\mathrm{SH}} = \left(2E_{\mathrm{kin}}.\frac{m_{\mathrm{H}}}{m_{\mathrm{SH}}.m_{\mathrm{H_2S}}}\right)^{1/2}, \tag{2.2a}$$

$$u_{\mathrm{H}} = \left(2E_{\mathrm{kin}}.\frac{m_{\mathrm{SH}}}{m_{\mathrm{H}}.m_{\mathrm{H_2S}}}\right)^{1/2}, \tag{2.2b}$$

where m_{H}, m_{SH} and $m_{\mathrm{H_2S}}$ are the masses of the H fragment, SH fragment and H_2S molecule, respectively. For the fragment to become stopped in the laboratory frame the condition $u_{\mathrm{SH}} = -v_{beam}$ must be met. By manipulation of equations 2.1 and 2.2a, the wavelength of the photons required to meet the photostop condition is given by

$$\lambda_{\mathrm{SH}} = hc\left[\frac{1}{2}\left(\frac{m_{\mathrm{SH}}m_{\mathrm{H_2S}}}{m_{\mathrm{H}}}\right)v_{\mathrm{beam}}^2 + D_0 + E_{\mathrm{int}}\right]^{-1}, \tag{2.3}$$

where λ_{SH} is the dissociation wavelength. With this consideration, it is feasible to produce molecules with zero velocity.

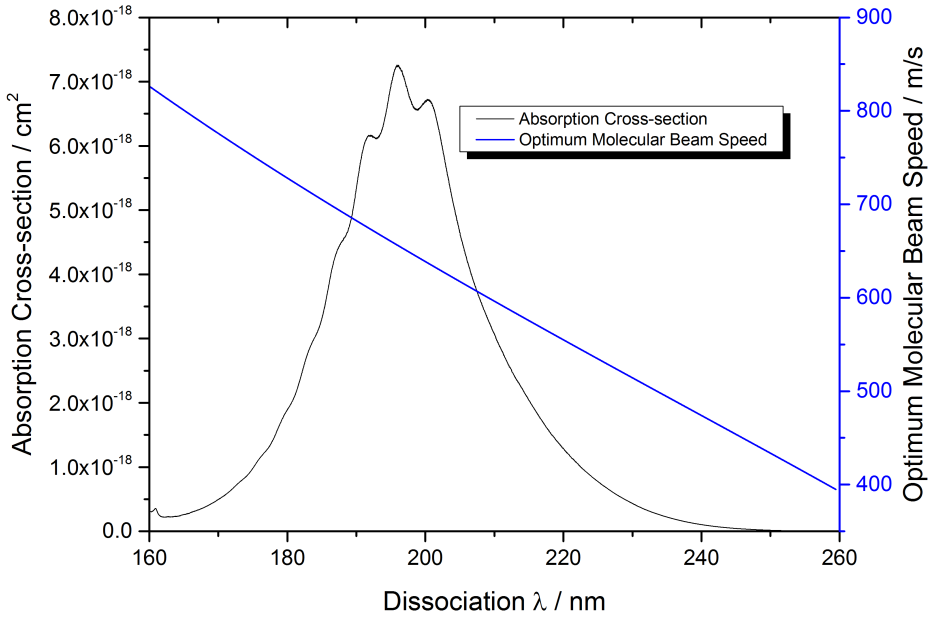

Fig. 2.2 Desired molecular beam speed of H_2S for different increasing wavelength of the dissociation laser along with the absorption cross-section of H_2S at the same wavelengths.

In order for the photodissociation to have the desired effect the velocity of the molec-

ular beam should be matched to the recoil of the target fragment. The molecular beam speed can be adjusted by mixing the target molecule with inert buffer gases which, via collisions, will speed up or slow down the movement the gas molecules. Similarly, the dissociation wavelength can also be adjusted to match a given molecular beam velocity. Additionally, for the purposes of trapping, it would be advantageous for the recoil (and therefore the molecular beam velocity) to be as small as possible as it would produce a smaller newton sphere and therefore porportionally produce more trappable molecules. This matching is, however, limited by the absorption properties of the parent molecule. For instance in the example of H_2S given in Fig. 2.2, performing the photodissociation at wavelengths above 220 nm would not produce as much SH as at 190 nm and therefore would not be favourable.

2.2 Past Results from Photostop

This technique is a fairly recent development in cold chemistry. In 2007, Matthews et al. [99] proposed that cold oxygen atoms could be made from NO_2 with zero mean-velocity by the photostop method. Since then the process has been successfully performed on both NO_2 (with NO_2 as the parent molecule and NO as the target fragment) and Br_2 (with Br_2 as the parent molecule and Br as the target fragment) [89,92]. A summary of the molecules that have been assessed for use in the photostop is given in Table 2.1; the current experiments within our group are focused on using H_2S/D_2S.

A schematic representation of the experiment (as used for NO_2, Br_2 and H_2S) is shown in Fig 2.3. The molecular beam is formed using a pulsed and skimmed supersonic expansion of a gas of the parent molecule mixed in with a defined ratio of carrier gases to alter the molecular beam speed and the direction of the molecular beam defines the z-axis of the experiment. This molecular beam is intersected at right angles by two laser beams counter propagating along the x-axis. The first laser is the dissociation laser and the light is either produced by a pulsed dye laser, the fifth harmonic of a pulsed frequency doubled Nd:YAG laser or an ArF Excimer

Table 2.1 Summary of previously assessed photostop molecules along with the positive and negative aspects of each experiment.

Target Molecule	Parent Molecule	Positives	Negatives
NO	NO_2	Easy to detect.	Too few fragments in trapping state
Br	Br_2	Comparatively straightforward.	
SO	SO_2	Readily available	Too few fragments in trapping state
SH	H_2S	Few quantum states populated.	Low fluorescence quantum yield and requires fast molecular beam.
SD	D_2S	Higher fluorescence quantum yield than SH	Requires fast molecular beam and D_2S is not universally readily available.

laser, depending on the species used (the former was used for NO_2 and the latter for H_2S). The second laser is the probe laser which is produced by a tunable pulsed dye laser and can be altered to perform either LIF or REMPI.

The REMPI scheme used for each photostopped species will naturally vary but the schemes requiring the smallest number of photons will be preferential in order to maximise the signal (i.e. molecules that can be photostopped with achievable 1 + 1 REMPI schemes would be preferable to those with 2 + 1 scheme). When using REMPI the laser beams are directed to intersect the molecular beam at the centre of an ion lens system orientated along the y-axis. The ions produced by the REMPI process are accelerated by the electrostatic field towards a position sensitive imaging detector which consists of a pair of microchannel plates, a phosphorescent screen and a CCD camera. The ion lens system is designed and operated such that the velocity of the original dissociated diatomic is mapped onto the detector using

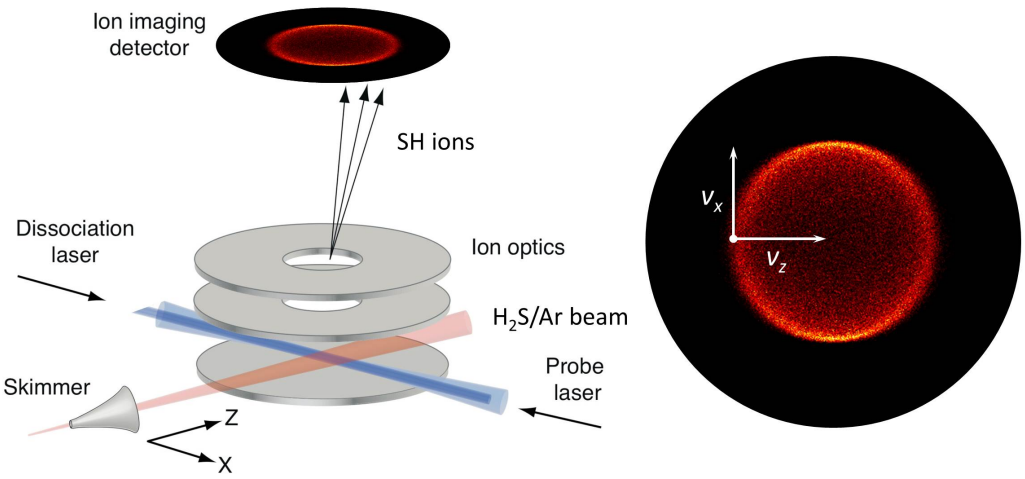

Fig. 2.3 Schematic of setup to photostop SH from H_2S with ion optics and VMI in the old system.

VMI. This detected ion image corresponds to the two dimensional projection of the three-dimensional velocity distribution of the molecules onto the (v_x,v_z) plane. This allows for the direct measurement of the absolute velocity of both the molecular beam and of the fragment molecules, allowing for optimisation of the process.

In order to demonstrate the photostopping process the stopped molecules need to be isolated from the rest of the molecular beam. This is achieved by altering the time delay between the probe and dissociation lasers. With increasing time delays the faster molecules will leave the area of the dissociation leaving the slowed or stopped molecules behind. This was illustrated for both Br_2 and NO_2 using a VMI detection apparatus [89, 92].

However even in this scenario the photostopped molecules would still leave the dissociation area eventually as the process does not completely stop all of them. To account for this the intention was to trap the molecules with a permanent magnetic trap as shown in Fig 2.4. On account of both the construction of the chamber used for the process and the effect of magnets on the motion of the ions in the VMI ion optics the REMPI could not be effectively used to illustrate trapping. To compensate for this, LIF was used as the detection method instead.

As with the REMPI process, the probe laser wavelengths used for the LIF varied for different species but it is preferential to select transitions to states which have large

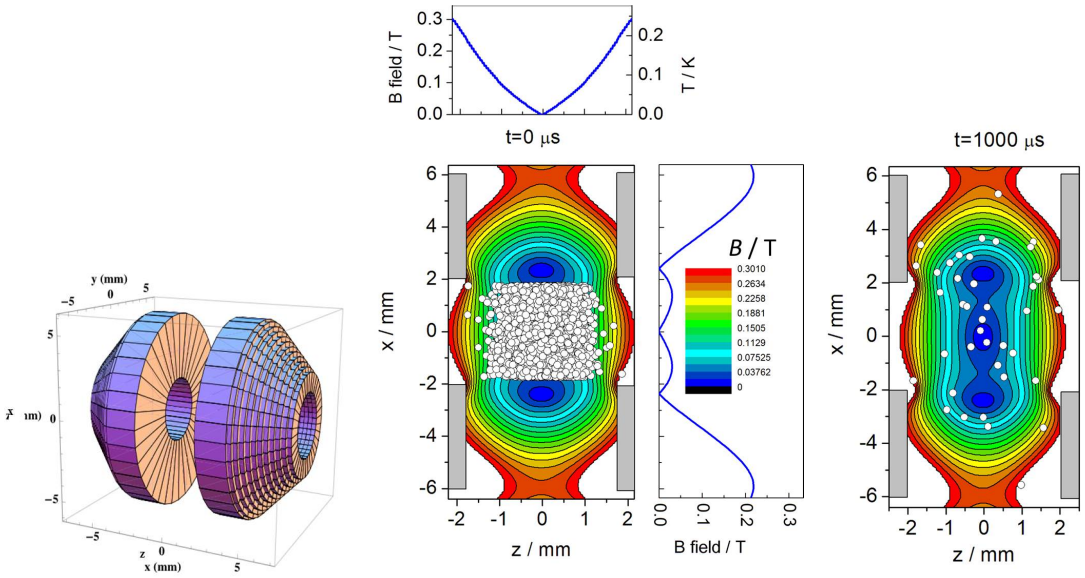

(a) Magnet Configuration (b) Magnetic trap at t=0 (c) Trap at t=1 ms

Fig. 2.4 Permanent magnetic trap used for trapping SH in prior experiments. It is $\approx 200\,\mathrm{mK}$ deep for $\mathrm{SH}(X^2\Pi_{3/2}, M_J = 3/2)$. Also shown are the spatial profiles of molecules in the trap for time delay of $0\,\mu\mathrm{s}$ and $1\,\mathrm{ms}$ after dissociation from Monte Carlo trajectory simulations.

absorption cross-sections and strong fluorescence properties. The laser beams with this method are directed to intersect the molecular beam near the focus of a set of detection optics. These optics focused the emitted fluorescence onto a detector (in previous cases a photomultiplier tube (PMT)), with a set of filters to remove stray light.

Trapping was first attempted for NO from NO_2 parent molecules but this encountered certain issues. The primary issue was that the LIF signal was not strong enough to distinguish it from the background signal. Additionally less than 0.5% of the NO molecules produced were in the correct state for trapping meaning that it would be unlikely that sufficient molecules would be trapped for them to be easily detected.

Thus for the more recent experiments H_2S has been used as an alternative as it was expected that almost 3% of the SH fragments would be in the correct state for trapping and the dissociation cross-section is an order of magnitude larger than for NO_2. The results of this investigation, along with corresponding simulations are shown in Fig. 2.5.

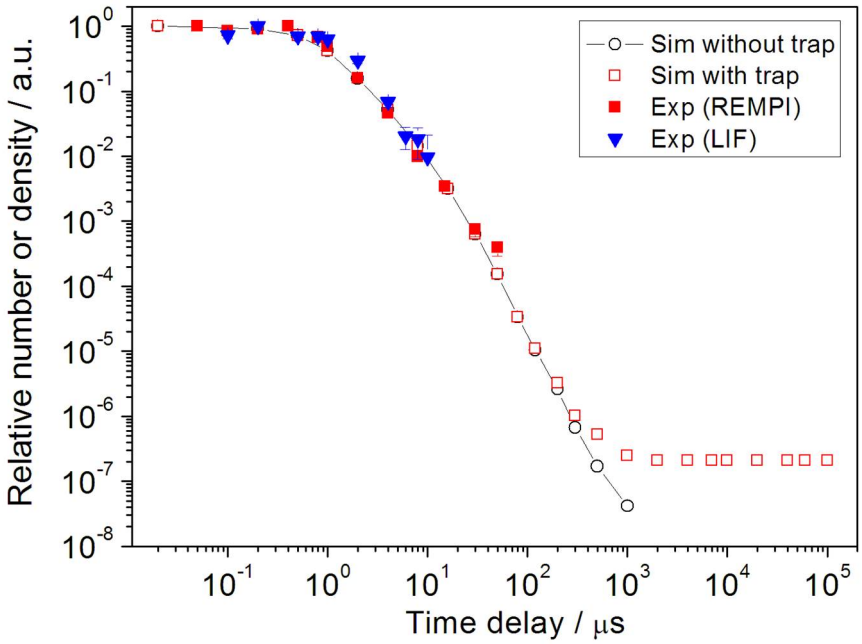

Fig. 2.5 Relative number density of SH molecules in the probe volume as a function of time delay between the dissociation and probe lasers. Experimental data (solid symbols) show current detection limits for REMPI and LIF detection. Simulations (open symbols suggest that trapping will only be observable after a time delay of $\approx 500\,\mu s$. These simulations do not include loss due to absorption of blackbody radiation or collisions with background gas.)

When performing photostop on H_2S it was only possible to take measurements at time delays up to around 100 µs. This is in part due to issues with noise in the LIF detection. However the more dominant issue is the predissociation dynamics of SH which weakens the fluorescence signal. As the effects of trapping only become apparent after 500 µs, it could not be demonstrated with this species at this time.

To improve upon this issue D_2S was used as an alternative to H_2S. This is because SD has a higher reduced mass than SH and subsequently a lower energy of the $v' = 0$ level. This reduces the probability of predissociation and increases the fluorescence quantum yield by a factor of 70 and so should provide a stronger fluorescence signal. However as shown in Fig. 2.6, although signal could be obtained for longer time delays, despite best efforts this did not provide sufficient improvement to demonstrate trapping.

Due to the significant problems with noise and the inability to demonstrate the trapping of SH/SD it was decided that the best course of action would be to design

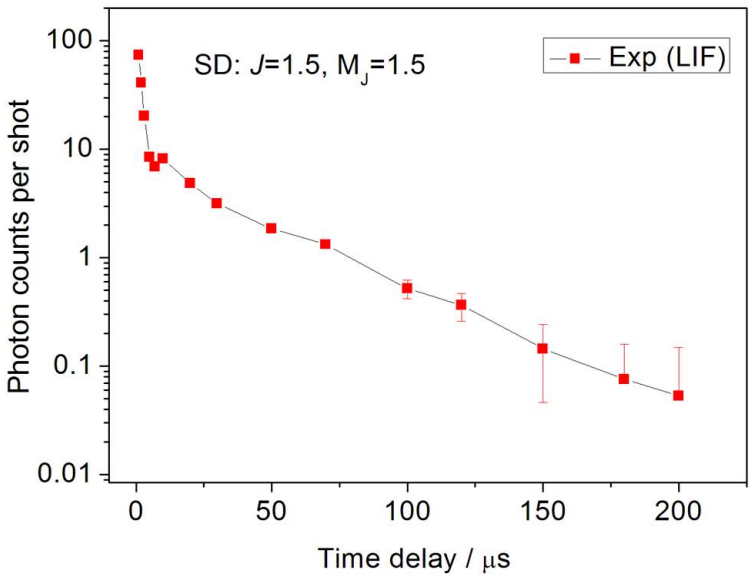

Fig. 2.6 Photon counting signal from the LIF detection of SD molecules in the probe volume as a function of time delay up to 200 µs between the dissociation and probe lasers.

a new dedicated chamber from scratch. With the foreknowledge of the issues that have arisen with the current configuration, this new system was intended to reduce these issues and allow trapping to be demonstrated.

2.3 Limitations of prior experiment

The primary reason behind the inability to detect photostopped molecules at increased time delays is that the signals at the longer time delays tend to be very weak and get lost in noise. There are a variety of sources for this noise and with a new dedicated chamber they can be addressed in turn.

When performing the LIF measurements with SD it became apparent that the primary source of noise that was preventing measurements at longer time delays was a source of stray light from inside the chamber. Despite best efforts the scattering, which we believe was the result of scattering of photons from surfaces and imperfections in the optics as well as fluorescence from impurities in the lens/window materials, could not be sufficiently eliminated. This included using different optical filters in front of the PMT to block out the stray light, use of a gated PMT to remove

the scattered light signal and modifying the beam profile to reduce the scattering. Filtering it out in this manner proved problematic as the wavelength of the scattered light is very close to that of the LIF signal itself. This implies that this signal is the result of scattering from the probe laser as SH has a very diagonal Franck-Condon factor, meaning that a large portion of the florescence emitted will be at the same wavelength as the initial absorption. Hence, the wavelengths of the scattered probe laser and the fluorescence emission are similar, thus producing difficulty in filtering one from the other.

Another issue with the current set up is that the chamber has been re-purposed from previous work, which provides a number of limiting factors for the experiment. First of all the centre of the magnetic trap is displaced from the centre of the ion optics used for the REMPI process. This makes it impossible to detect molecules held in the magnetic trap, which is especially detrimental as REMPI is often the more sensitive of the two measurement techniques that are being used for this experiment and so would more likely be able to detect the photostoped molecules at the longer time delays.

A further issue is that of the number density of the molecules in the trap. The difficulty in detecting molecules at long time delays is not entirely due to noise but also as a result of the small number of molecules in the trap. Thus if the initial number density in the molecular beam is larger the signal at the longer time delays will be stronger. However there is a significant limiting factor to this in terms of the technology available. As such it may be worth experimenting with different molecular beam sources to maximise the number density in the trap. At present this is a secondary concern as we have a reliable molecular beam source but this may be examined in the future.

3. DESIGN OF NEW EXPERIMENT

In order to make significant improvements over the previous experimental apparatus, the new chamber needed to be purpose built to perform photostop and demonstrate the trapping of molecules. With this in mind the focus is of the new design was on the trap itself and maximising the number of molecules that can be trapped and measured. To this end, the following chapter outlines the considerations that were made and how each issue was addressed.

3.1 Magnetic Trap

Arguably the most crucial aspect of the new experimental design is the magnetic trap for containing the photostopped molecules. To fully appreciate this we need to more thoroughly consider the Zeeman effect mentioned in Section 1.3.1 and how it relates to molecular states. For molecules the orbital and spin angular momenta of the electrons as well as the rotational motion of the molecule, couple to give the total angular momentum as denoted by the quantum number J. When the molecule is placed in a magnetic field, it will align itself with the magnetic field direction. The alignment of J with respect to the magnetic field is quantised, and the component of J along the field direction is given by $M_J\hbar$ where M_J can take values of $J, J-1..., -J$. For a diatomic molecule following Hund's coupling case (a)[1], the energy of the molecule in a magnetic field will vary with M_J according to the equation [100]:

$$\Delta E = \frac{(\Lambda + 2\Sigma)(\Lambda + \Sigma)}{J(J+1)} M_J \mu_B B, \tag{3.1}$$

[1] A more thorough description of this is given in [100].

where Λ is the projection of the total orbital angular momentum of the electrons onto the internuclear axis, Σ is the projection of the total spin angular momentum of the electrons onto the internuclear axis, μ_B is the Bohr magneton, and B is the applied magnetic field.

For this investigation, the target molecule is SH($X^2\Pi_{\frac{3}{2}}$) and we are looking to trap the $J = \frac{3}{2}$ state, which we can approximate as following Hund's coupling case (a). This allows us to simplify Equation 3.1 to

$$\Delta E = \frac{3M_J\mu_B B}{J(J+1)}. \tag{3.2}$$

The upshot of this is that an increasing magnetic field results in an increase or decrease in the molecule's internal energy depending on the orientation of J in the magnetic field. A representation of this is shown in Fig. 3.1. Molecular states for which an increasing magnetic field results in a decrease in internal energy are referred to as high-field seeking states and those whose energy increases are known as low-field seeking states. Molecules in a low-field seeking state will gain internal energy when entering a magnetic field and therefore will be repelled by it and hence can be confined within a region of space (i.e. trapped) by a magnetic field.

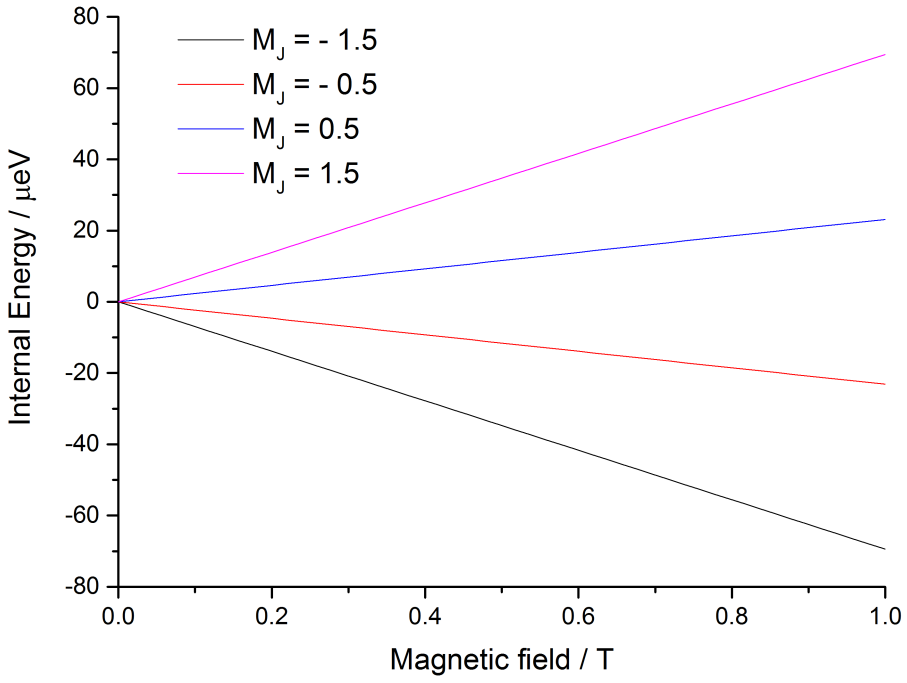

Fig. 3.1 The Zeeman effect for a SH molecule with $J = 1.5$.

The goal in designing the magnetic trap was to produce a deep quadrupole magnetic trap from two magnets in an anti-Helmholtz configuration which maximises the strength of the magnetic field whilst allowing easy access to the trap volume so that the molecular beam and the dissociation/probe lasers can pass through it (as well as to allow for fluorescence/ions to escape from it for detection, see section 3.8 for more details). From earlier investigations in the group, rod-shaped magnets have been shown to produce the largest possible magnetic field by maximising the amount of magnetic material present. However, using a closed rod restricts at least one axis of access to trap volume so we instead opted for ring magnets. Additionally, although decreasing the separation between magnets is an effective way to increase the magnetic field, a compromise must be reached to allow the aforementioned accessibility to the trap volume. As such, a minimum separation of 4 mm between the magnets was decided upon.

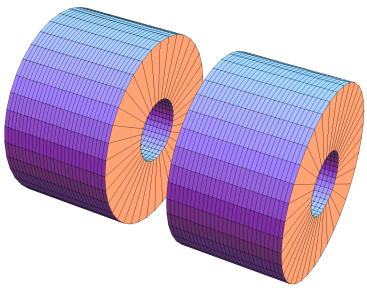

Fig. 3.2 Simulated magnet configuration from Mathematica.

To design the magnet configuration of the trap a number of alternatives were simulated by another member of the group using the Radia magnetostatics computation package with Wolfram Mathematica 9.0. The final configuration was formed from two permanent NdFeB ring magnets. The magnets, as shown in Fig. 3.2, have a residual magnetisation along their cylindrical axes of 1.46 T, an outer diameter of 12.0 ± 0.1 mm, an inner diameter of 4.0 ± 0.3 mm and a thickness of 7.0 ± 0.1 mm. For clarity in these simulations, we define the z-axis as the cylindrical axis through the bore of the magnets and the x and y axes as radial.

Using Mathematica, the root mean square (RMS) magnetic field strength of this

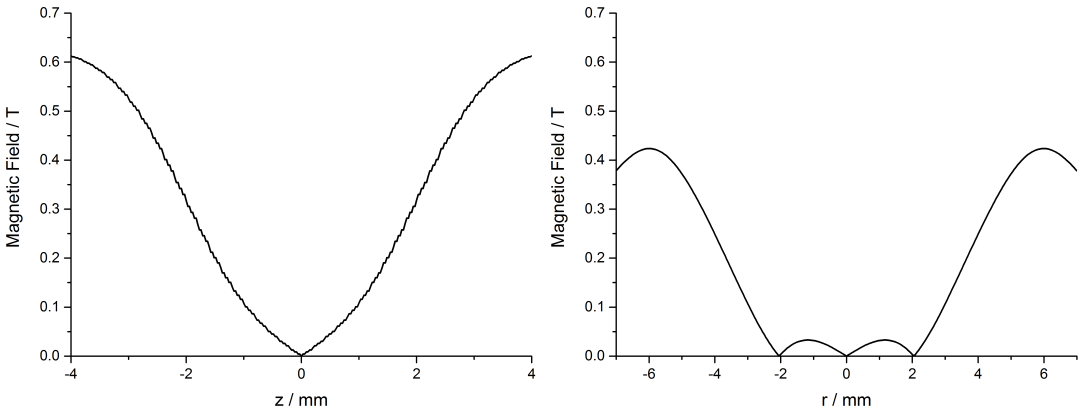

(a) (b)

Fig. 3.3 Simulated RMS magnetic field strength of the permanent magnet configuration both axially (a) and radially (b). For these graphs the magnets are spaced 4 mm apart.

configuration was simulated both axially and radially as shown in Fig. 3.3. The cylindrical symmetry of the magnets means that this magnetic field is radially symmetric. In the radial direction (Fig. 3.3(b)) the magnetic field reaches a maximum of 0.41 T at the outer rim of the magnets after which it rapidly decays to zero as we leave the trap volume. Also there are two subsidiary maxima in the centre of the potential well due the central bore in the magnets. Axially (Fig. 3.3(a)) the potential well reaches a maximum of approximately 0.62 T at a distance of 4.5 mm from the trap centre. The significant difference between this and the radial magnetic field strength ensures that molecules exiting the trap will be far more likely to do so radially. The axial magnetic field reaches the maximum at approximately 2.5 mm into the bore of the magnet. This is an unavoidable consequence of using ring magnets but should have little effect on the trapping of the target molecules.

To give a more complete picture of the trap we have also derived a contour plot of the full trap volume as shown in Fig. 3.4. On this graph the minimum of the expected trap volume is shown in the centre in blue at the bottom of the magnetic potential well and the trap itself extends as far as the outer rim of the magnets. Also shown on the plot are a number of artificial discontinuities (shown by the black marks). This is a known issue for field computation for subdivided objects in Radia and results from the assignment of constant magnetisation values to each sub-object which make up the magnets.

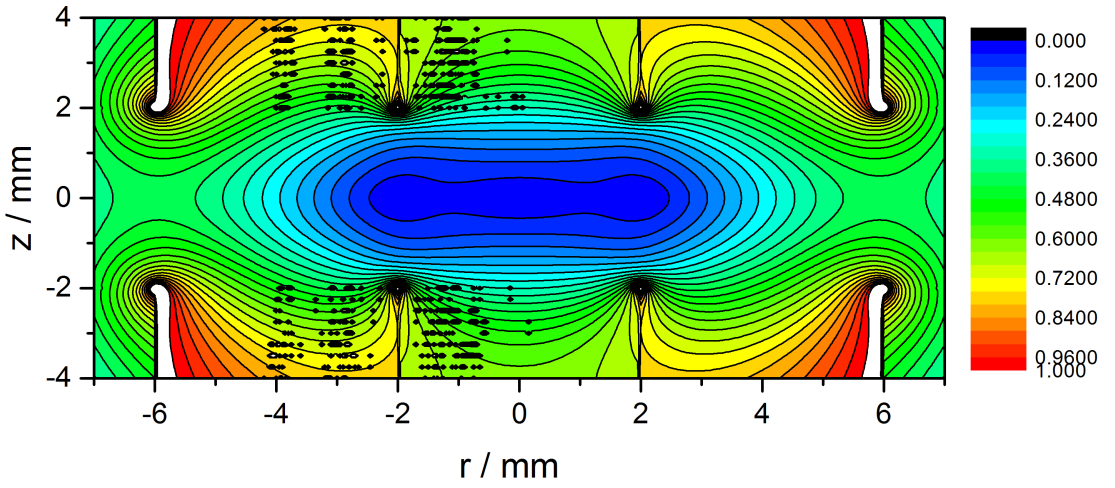

Fig. 3.4 Simulated contour plot of the RMS magnetic field strength in the one of the axial planes. Contours increase in size from blue to red in even steps.

3.2 Pumping the Trap Volume

In order to maximise the lifetime of any molecules held in the magnetic trap, the trap volume needed to be evacuated to a high (approx 10^{-7} mbar) or ultra-high (below 10^{-9} mbar) vacuum. Given the small size of the trap, fully evacuating it between repetitions of the experiments could become problematic. To directly counter this issue we decided early on that the magnetic trap would be housed on the cold head of a cryostat. For this experiment, to make the cryostat we re-purposed a cryopump (Leybold-Heraeus, RPK1500) in its entirety. When properly cooled, this cold head could potentially reach temperatures less than 20 K, effectively turning every surface in the trap housing into a pump and thus more efficiently pumping the trap volume. However, the cryostat could not be used as the sole pump because over time adsorbed molecules would build up on the surfaces effectively saturating them and these would be released en masse when the cryostat is turned off. Thus we supplemented the cryostat with a large turbopump (1200 L s^{-1}, Pfieffer HiPace 1200 U) backed by an appropriate two stage rotary vane pump (65 m^3 s^{-1}, Leybold, Trivac D65B), that would provide a base level of high vacuum, which would then be improved upon with the operation of the cryostat as well as providing a means to remove adsorbed gases when the cryostat is warmed up after operation. Further, in order to achieve the best possible vacuum, efforts were made to utilise copper-sealed

flanges throughout the chamber design (as opposed to o-rings) due to the better quality of seal made by them.

3.3 Experimental Apparatus Overview

Before addressing the individual components of the experimental apparatus in detail we should first consider the structure as whole so that a better picture can be drawn of how it fits together. As previously mentioned, the focus of this experiment is the magnetic trap which we have elected to house on the cold head of a cryostat. As we have re-purposed a cryopump (Leybold-Heraeus, RPK1500) to serve as this cryostat this inherently entailed some restrictions on the design. Namely, the cryopump has a permanent chamber structure with a 200 CF flange as the main vacuum connection. On account of this we have utilised a specialised 10" spherical octagon (Kimball Physics) to allow for the required laser access (which will be explored in Section 3.7) as well as a further extension piece to allow for sufficient time of flight for the ion optics (which will be discussed further in Section 3.8.2). Further, to account for the fact that the cold head of the cryopump is withdrawn from the flange face, extension pieces were required for the trap housing and outer shield (as will be explored in Sections 3.4 and 3.5). Details of the design will be explored further in following sections, but a complete cross-sectional overview is presented in Fig 3.5.

3.4 Magnetic Trap Housing

In order to be able to position the magnets to form the magnetic trap a permanent housing is required. As previously mentioned, the cryostat was the base of the entire machine and its inner stage lay at its centre. This meant that the housing for the magnets needed to be built on the inner stage to ensure that it is centralised and to maximise the benefits of the cryostat.

Within the magnetic trap housing shown in Fig. 3.6 there are several components in addition to the magnets themselves (as can be seen in Fig. 3.7). These additional

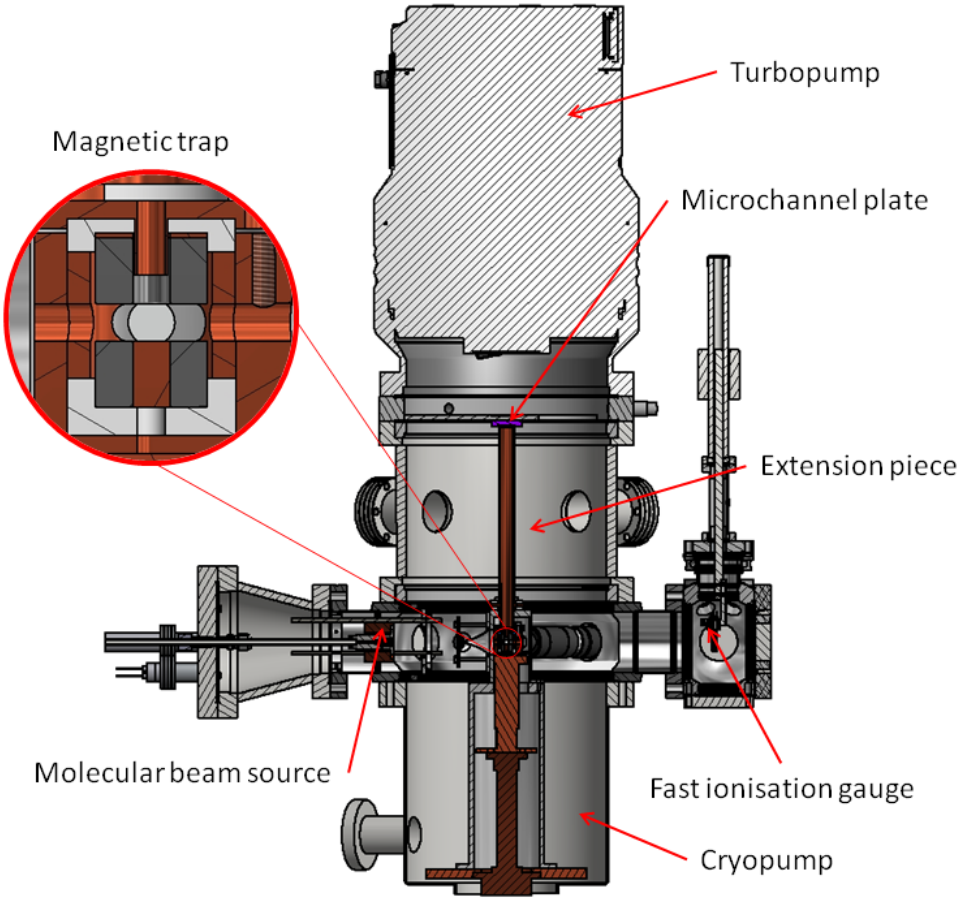

Fig. 3.5 Cross-sectional schematic of the new vacuum chamber for the photostop experiment.

pieces are required for use in the ion optics as will be outlined in 3.8.2. For the ion optics the magnets need to possess a voltage that is independent of the housing. Thus, in order to maintain the cooling effect of cryostat a material that is thermally conducting but electrically insulating is required to separate them. For this purpose we elected to use the ceramic boron nitride which has a high thermal conductivity but is electrically insulating.

For the trap, as outlined previously, the two permanent magnets needed to be held 4 mm apart in order to produce the required magnetic fields. In the trap housing along this 4 mm gap there is a long 4 mm slit. This slit is to allow access for the molecular beam and lasers as well as an avenue where fluorescence can escape from the trap centre.

In terms of assembly, as shown in Fig. 3.7, the individual components can be slotted

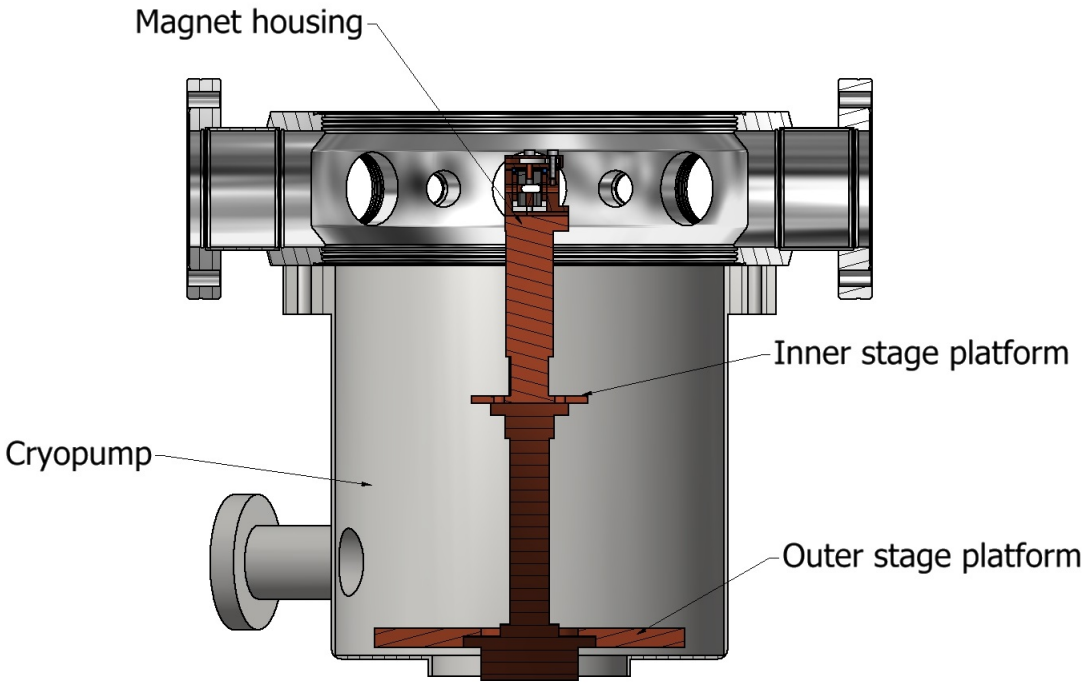

Fig. 3.6 Cross-section view of magnetic trap housing mounted on the cryostat.

in sequentially to form the configuration shown. The repulsive forces between the magnets kept them separated and therefore allowed them to be held in the correct configuration. In cases where dummy pieces are used to replace the magnets the upper piece will be reconstructed to incorporate the electrodes and dummy pieces separated by an insulator.

3.5 Outer Shielding

In order to maximise the efficiency of the cryostat it is best to reduce the number of direct lines of sight to the inner stage as much possible. The purpose of this is to minimise the heating effect of black-body radiation from room temperature surfaces on the cold head of the cryostat. This was achieved by use of the outer stage of the cryostat, from which an outer shield was built to form a thermal shield. As the outer stage was also being cooled by the cryostat, the amount of thermal contact with room temperature equipment was reduced as much as possible[2].

[2] Some thermal contact was unavoidable due the requirements for power supplies to the ion optics, but this was minimised using long thin wires.

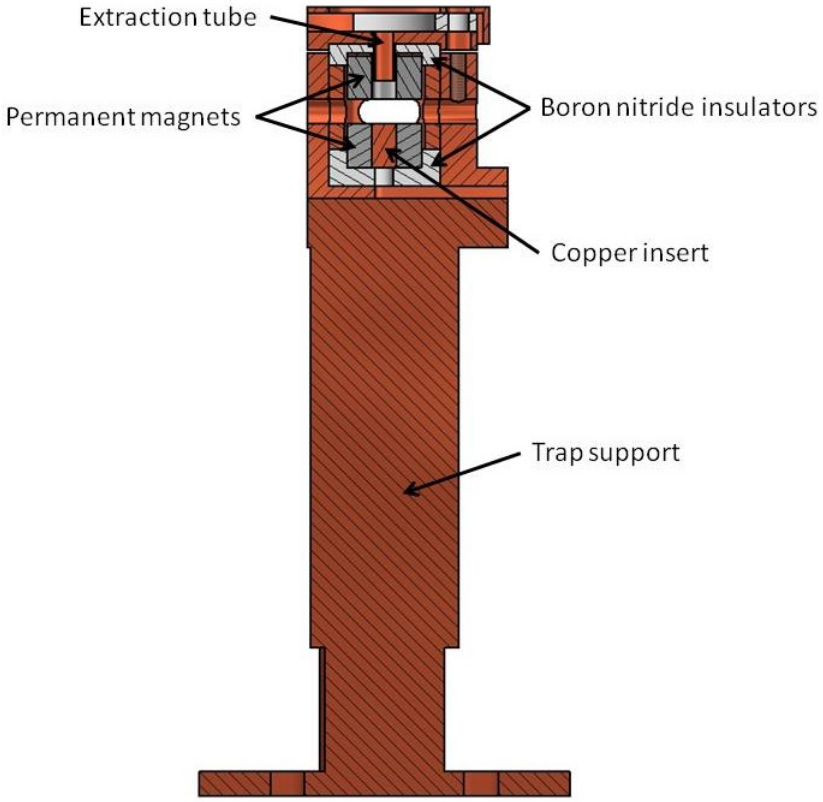

Fig. 3.7 Magnetic trap support cross-section.

As shown in Fig. 3.8, the primary support for the outer stage comes from the base which is attached directly to the outer stage of the cryostat. This provides a large platform upon which different components can be mounted, for instance monitoring components like thermocouples.

The upper piece of the outer stage consists of several components to facilitate different aspects of the experiment. In the structure of the core piece there are a number of different holes on the cylindrical surface to allow for access for the lasers and molecular beam. In addition to this there are two cylindrical extrusions with tapped holes that lead into the centre of the trap. The purpose of these was that the tapped holes allow for components to be mounted onto the cryostat in order to facilitate different monitoring methods (this will be expanded upon in section 3.8). In addition to this, there was a planar surface that has been cut into the main cylindrical structure. The purpose of this was to allow the molecular beam skimmer to be mounted as close as possible to the centre of the magnetic trap in order to maximise the portion of the molecular beam which enters the trap and therefore

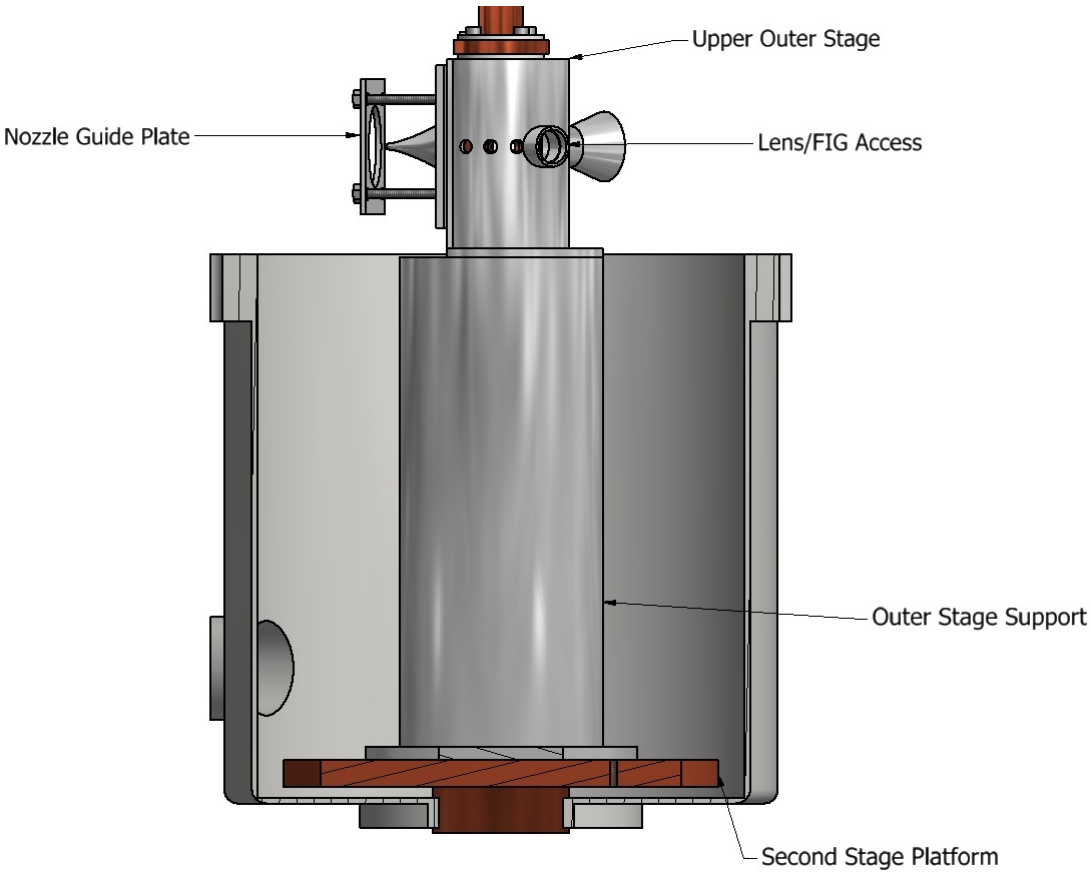

Fig. 3.8 Cross-section view of outer stage assembly mounted on the cryostat.

potentially increase the number of molecules that enter the trap volume and are dissociated. On the top of the core of the outer shield there is a hole to allow for the time-of-flight tube to be fixed to the outer stage. The time-of-flight tube forms part of the ion optics as outlined in section 3.8.2.

The skimmer was held onto the central piece by what was known as the skimmer plate. This piece sandwiches the skimmer to the outer stage to hold it in place. The bolt holes used to secure the skimmer plate have been designed to be deliberately too large in order to allow for adjustments to be made in the position so that the skimmer is properly aligned with the centre of the trap.

3.6 Molecular Beam Source

For the purposes of generating a molecular beam, the experiment predominantly utilised a pulsed solenoid valve (Parker, General Valve, series 9 with IOTA ONE pulse driver) to give short pulses of gas for the molecular beam. However there are many other different types of valves and molecular beam sources so it is preferential to allow for the greatest adaptability in the design.

The initial intention for the design was to utilise a custom built piezo valve for our molecular beam source. As this has a diameter of 46 mm this meant that 35 CF flanges on the aforementioned spherical octagon needed to be replaced with 63 CF half nipples. During construction of this valve there were some issues with sealing so it was not used in this experiment. However, given the size of the valve it was used as a benchmark from which to work from as other molecular beams sources/valves tend to be smaller.

To accommodate the operational requirements of the molecular beam source a specialised 100 CF flange was commissioned. At the centre of this flange was a cajon fitting to secure a $\frac{1}{4}$" pipe which served as the connection from the external gas line to the valve as well as a means to alter the position of the valve by simply adjusting the pipe (i.e. pulling it in or out or turning it). To facilitate the required electrical inputs to the nozzle a number of 16 CF half nipple extensions were added to the flange.

Another important factor to consider is how to ensure that the nozzle of the molecular beam source is aligned with the centre of the octagon. For this a support structure is required to guide the nozzle and ensure it does not move as result of vibrations from the cryostat. With this in mind the design of the structure shown in Fig. 3.9 was chosen. This utilises a unique feature of the spherical octagon, namely the grabber grooves, which are small recesses in the walls of the chamber upon which components can be mounted. The rods shown both support the nozzle and guide it into the right position. The points at the ends of the rods are pointed in order to allow them to be guided to a plate that centred the nozzle with respect to the

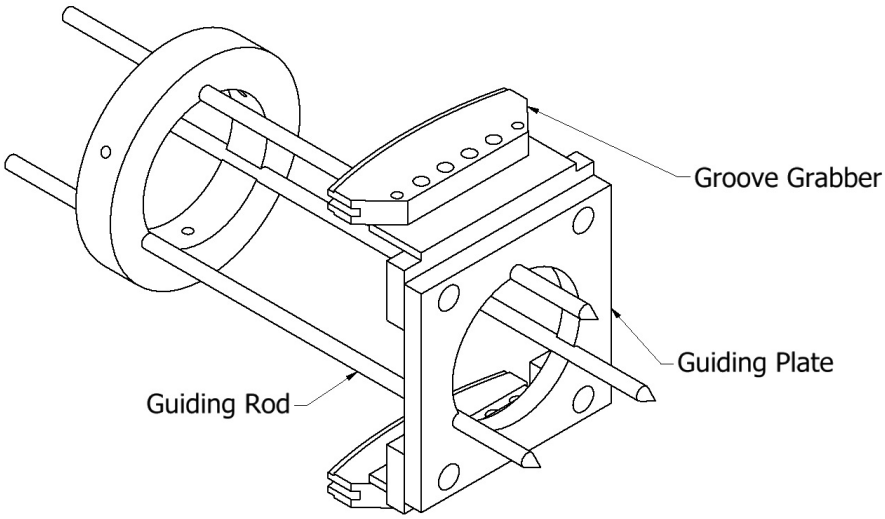

(a) Grabber Groove Support Structure

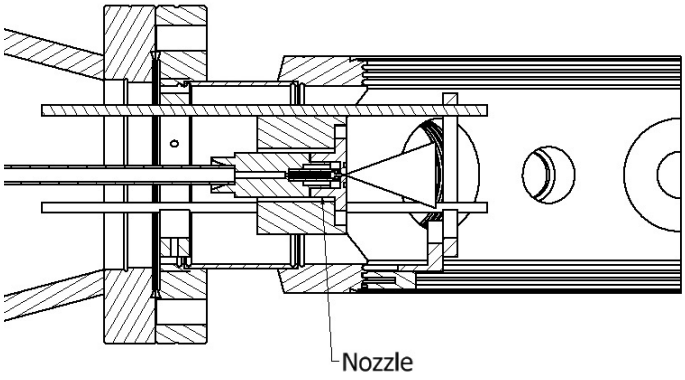

(b) Nozzle Support Structure Mounted on Spherical Octagon

Fig. 3.9 Grabber Groove Support Structure for guiding and securing the nozzle

skimmer (see section 3.5).

3.7 Laser Systems

Both the photodissociation and the measurement of trapped molecules require the use of specialised laser systems as well as access for these lasers to the trap volume. To accommodate these requirements available equipment was utilised to produce the laser sources needed.

For the dissociation laser, from Fig 2.2 it is clear that in order to obtain the highest yield of our dissociated SH a dissociation wavelength of around 190 nm should be

used. In this experiment a dissociation laser with a 213 nm wavelength was generated from the fifth harmonic of a pulsed Nd:YAG laser (Continuum, Surelite I-10). The fifth harmonic was generated by combining the fourth and first harmonics of the laser using a specialised BBO crystal. The other harmonics were separated out using a series of dichroic mirrors and prisms. The final output of this resulted in a 5 ns output with a pulse energy of around 2 mJ at a repetition rate of 10 Hz.

For the probe laser, vastly different wavelengths would be required for the different measurement processes (LIF and REMPI), which would likely need to be tunable to account for the finer rotational structure of the target molecule. To accommodate this, the probe laser was generated from a pulsed dye laser (Sirah, CobraStretch with frequency conversion unit) pumped by a Nd:YAG laser (Continuum, Surelite I-10). As the wavelengths for each measurement method were so different, different dyes and pumping wavelengths (i.e. the second and third harmonics of the Nd:YAG) were used for each process as will be outlined in the experimental sections in later chapters.

One of the main goals of this new experimental set up is to allow for multiple measurement methods to be applied to the molecules in the trap volume. This ultimately requires that the dissociation and probe laser intersect in the trap centre and that the trap allows for such an intersection. In a lot of experiments when lasers need to be overlapped in this manner they can be aligned to be on the same axis but counter-propagating to each other. However, this configuration can be problematic as with high powered lasers the optical elements involved can quickly become damaged. Thus for this experiment we adopted a different approach in having the laser axes intersecting from different angles as shown in Fig. 3.10.

The vacuum chamber part shown in Fig. 3.10 is a custom made 10” spherical octagon (Kimball Physics) which has been modified to accommodate the particular requirements of this experiment. Specifically, a pair of 16 CF ports were added to each side of the piece at an angle of 22.5° from the central axis to allow for laser access and two of the 35 CF ports were replaced with 63 CF extensions to accommodate the molecular beam sources.

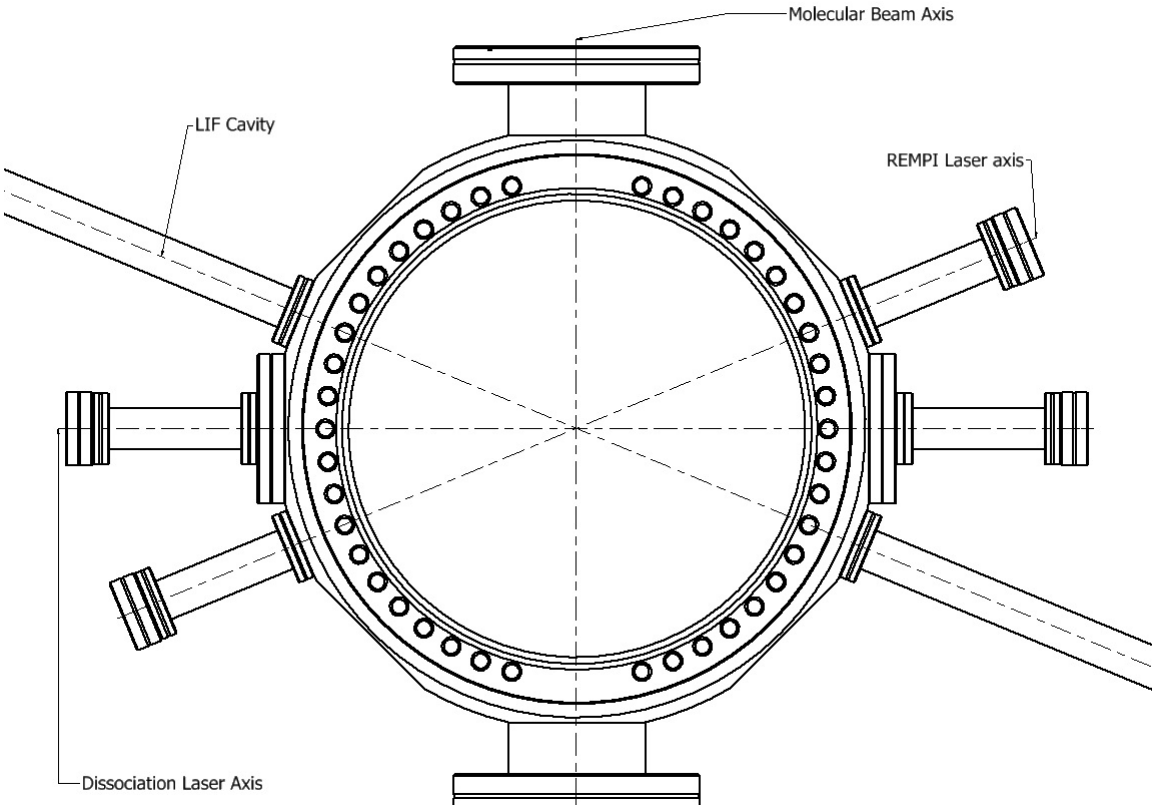

Fig. 3.10 Custom spherical octagon configuration for laser axes. In this picture only the ports used directly for laser access are shown, the unoccupied ports in this diagram will serve other purposes as outlined later. Further, the aforementioned laser baffles are fitted into the 16 CF full nipples on the dissociation and REMPI axes. The LIF axis has longer extensions in order to facilitate a cavity as outlined in Section 3.8.1.

Another consideration for the laser access is that of the potential sources of noise from scattered light and fluorescing components. To reduce unwanted fluorescence, the windows used for laser access were made from UV-grade fused-silica or CaF_2 which are not strongly absorbent at the wavelengths used and so are less likely to fluoresce. For the reduction of scattered light we allowed for the introduction of laser baffles on the laser axes. Laser baffles are essentially a series of absorbing cone shaped surfaces orientated along the laser beam path. For lasers propagating from the apex of the cones to the base, the baffles block the extremities of the laser beam profile as well as any scattered light [101].

3.8 Measurement Techniques

3.8.1 Theory

During the course of this project a number of different measurement techniques have been applied. Here, a brief summary of theoretical background of some of the techniques is presented[3].

Laser Induced Fluorescence

Since we are building from the previous experiments it is natural that the use of LIF as a detection method for the photostopped molecules will continue in some form. As outlined previously in Section 1.4.2, LIF is a highly sensitive technique that detects molecules by exciting them with a laser and measuring the fluorescence produced. For single-pass LIF the magnitude of the recorded output signal is given by [102]

$$S^{\mathrm{LIF}} = I^{\mathrm{LIF}} \cdot \alpha \cdot \Gamma \cdot g, \tag{3.3}$$

where S^{LIF} is the magnitude of the fluorescence signal, I^{LIF} is the intensity of the excitation light source[4], α is the molecular absorption coefficient, Γ is the fluorescence quantum yield of the excitation and g is an instrument dependent factor. As the only measurements taken are of the fluorescence of the target molecule this technique is, in principle, background free meaning it can be used for a large range of α (i.e. for both large and small numbers of molecules). However, in practice there can be issues with stray light which make the detection of very small numbers of molecules problematic. Another issue with this technique is that the instrument dependent factor g is defined by the nature of the measurement, the instrument (i.e. how the light is being measured and the efficiency of the detector) as well as the nature of the optical collection system (i.e. how many of the fluorescing molecules are actually seen)[5]. These factors are hard to determine and so precise absolute

[3] The theory behind REMPI has already been outlined in Section 1.4.1.
[4] This corresponds to the number of probe laser photons interacting with the sample
[5] It should be noted that the g factor is highly dependent on the nature of the measurements taken both in terms of magnitude and the units of the factor itself.

density measurements are difficult to do with LIF so this technique tends to be used in experiments where only relative numbers are significant. That said, recent work has, with great effort, been able to calibrate this detection efficiency for a given experiment with an error of 30% [103].

Cavity Ring-Down Spectroscopy (CRDS)

As outlined in section 1.4.3, CRDS is a form of absorption spectroscopy for measuring absolute number densities which uses the Beer-Lambert law and measures very small losses of light by weak absorbers. In these experiments a pulsed laser is coupled into a cavity that encloses an absorption cell. At the end of the cavity there is a light detector (often a PMT) which measures the light escaping the cavity. As the laser is pulsed, the amount of light escaping the cavity will decay over time. This is because, as there is no additional light input into the cavity when the pulse is switched off, with each round trip of light inside the cavity more light is lost, hence the amount of light escaping will decay exponentially over time following the equation

$$I(t) = I_0 \cdot \exp\left(-\frac{t}{\tau_0}\right) \tag{3.4}$$

where $I(t)$ is the intensity of light at time t, I_0 is the initial light intensity and τ_0 is the time required for the initial intensity to decay to $\frac{1}{e}$ of its original value; this is known as the ring-down time (RDT). In an evacuated cavity with highly reflective mirrors, the RDT is related to the reflectivity of the cavity mirrors by [98]:

$$\tau_0 = \frac{L}{c(1-R)} \tag{3.5}$$

where L is the distance between the mirrors, c is the speed of light in vacuum and R is the mirror reflectivity. If there is a gas that absorbs the wavelength in the cavity, the RDT will reduce as the light in the cavity is reduced more rapidly.

By measuring the reduction in RDT and with an application of the Beer-Lambert law the particle density in the cavity can be measured. If we take the Beer-Lambert

law as defined by

$$I(t) = I_0 \exp(-\sigma \rho c t), \tag{3.6}$$

where σ is the absorption cross section of the absorbing particle and ρ is the particle density. The decay in intensity will occur simultaneously to the ring-down decay defined in equation 3.4, meaning that they can be combined thus

$$I(t) = I_0 \exp\left(-\frac{t}{\tau_0} - \alpha c t\right), \tag{3.7}$$

with α as the molecular absorption coefficient $\alpha = \sigma\rho$. This can be rewritten as

$$I(t) = I_0 \exp\left(-\frac{t}{\tau}\right), \tag{3.8}$$

where τ is the reduced RDT of the filled cavity defined by

$$\frac{1}{\tau} = \frac{1}{\tau_0} + \alpha c. \tag{3.9}$$

This can be rearranged to give

$$\alpha = \frac{1}{c}\left(\frac{1}{\tau} - \frac{1}{\tau_0}\right) = \sigma\rho. \tag{3.10}$$

From this, provided that σ is known, absolute values of the particle density of the cavity can be measured.

Cavity Enhanced Laser Induced Fluorescence (CELIF)

To combat the background signal due to scattered light we considered the use of an optical cavity along the LIF probe laser axis to perform cavity-enhanced laser-induced fluorescence (CELIF). In essence optical cavities are simply a set two mirrors whereby the laser light enters through one mirror and reflects back and forth between them and would assist in reducing stray light in the chamber.

The reason that an optical cavity will reduce the stray light is that the only light

that is coupled into the cavity will remain in the cavity. The resonant modes of a cavity are those of the wavelengths that are capable of producing standing waves in the cavity. Light entering the cavity which is not resonant with a cavity mode will destructively interfere with reflections from the mirrors and therefore will be removed. This will significantly reduce the potential occurrence of stray light from the probe laser thus reducing the background level.

CELIF combines CRDS and LIF by placing the fluorescence probe laser in an optical cavity and essentially performing both techniques simultaneously. The full description of this method is given in [102, 104] but in basic terms, a probe laser, as used in conventional LIF, is coupled into an optical cavity and the fluorescence produced measured. Simultaneously the ring-down decay from the cavity is measured and provides a measure of the intensity of light used in the fluorescence process such that $I^{\mathrm{LIF}} \propto I^{\mathrm{CRD}}$ where I^{CRD} is the time integrated light intensity as measured by the CRD detector. From this we can define the CELIF signal as [102]:

$$S^{\mathrm{CELIF}} = \frac{S^{\mathrm{LIF}}}{I^{\mathrm{CRD}}} = \alpha \cdot \Gamma \cdot \frac{2g}{T}, \tag{3.11}$$

where T is the transmission of the exit cavity mirror. This is effectively the LIF signal normalised with the shot-to-shot integrated CRD intensity. By using this measurement, the shot-to-shot fluctuations in the probe laser intensity are directly accounted for and the instrument dependent $\frac{2g}{T}$ factor can be determined by calibrating the recorded CELIF signal with absolute absorption measurements from CRDS. Additionally, as the probe laser is coupled into cavity, only longitudinal and transversal modes of the cavity can exist within it, meaning that there is a significant reduction in stray light from the probe laser.

3.8.2 Application

The measurement techniques described above require some specialist equipment to be used. Here an outline of the apparatus used for these measurements are

presented[6].

LIF Detection Apparatus

If the previous experiments are to be improved upon it will require a careful consideration of a number of factors. First and foremost there is the issue of background signal that has hampered the previous investigation. One of the more significant issues was that of stray light, which we define as a background level of light signal that arises as a consequence of imperfections in the optical aspects of the experiment; for instance back reflections of the probe laser from an optical element could contribute to this stray light. This clearly needs to be significantly reduced in order to reduce background levels and hence improve upon the limit of detection. In addition to this, a reduction in the electrical noise would also increase the signal to noise ratio and allow for readings of smaller number densities of molecules.

In order for the LIF detection to be as efficient as possible one must consider where to place the light detection device in relation to the centre of the magnetic trap. As with previous investigation we will be utilising a PMT as the photon detector.

The photons are emitted from the fluorescence process isotropically, meaning that the PMT can be placed at any position provided that there is a line of sight to the centre of the trap. In principle the PMT could also be mounted inside the vacuum chamber. However if this was the case the PMT would detect all light inside the chamber and would likely have greater issues with stray light.

As an alternative to mounting the PMT inside the chamber a lens system can be used to focus the light from the fluorescence onto the PMT. As shown in Fig. 3.11, with a lens placed at a distance larger than the lens' focal length, the light emitted from the trap is focused into an image behind the lens. If an aperture is placed at this distance that is the size of the image then the majority of light from other sources that enter the lens should be blocked by it. Then the light that passes through the aperture can be refocused onto the PMT by a second set of lenses.

[6] Although more detail on the apparatus used will be presented as required in later chapters.

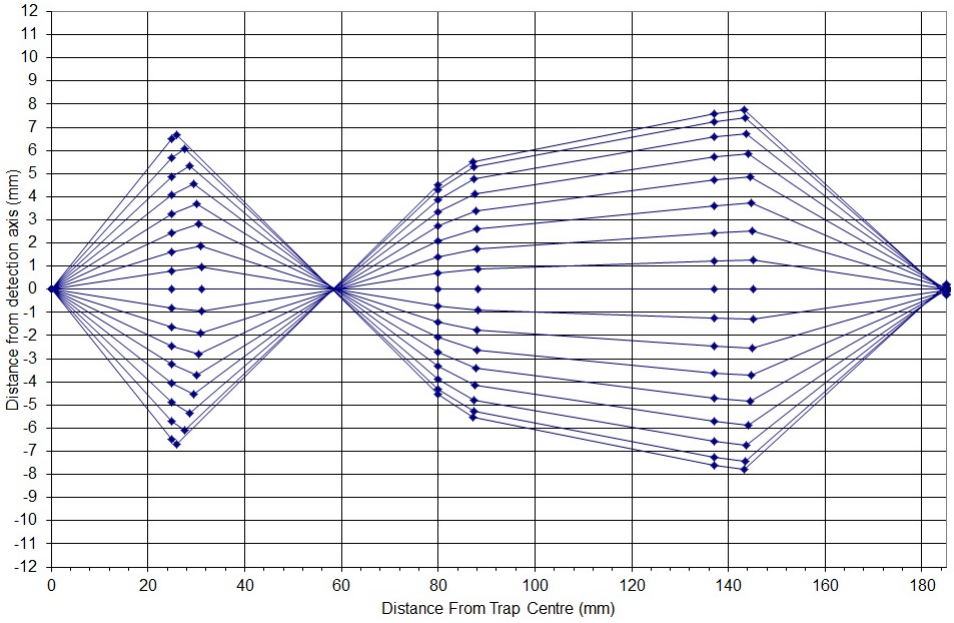

(a) On axis Ray Tracing

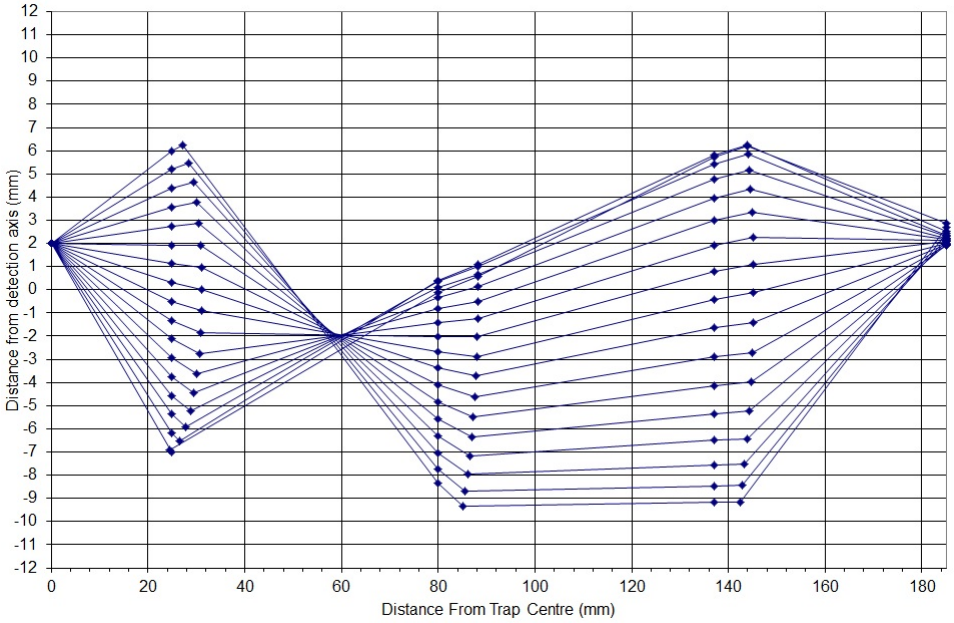

(b) Off axis Ray Tracing

Fig. 3.11 Ray tracing diagrams for the LIF detection both on and off axis. The first lens has a 1/2" diameter and a focal length of 14.3 mm and the other two are both 1" diameter with a focal length of 33.3 mm. The PMT in this diagram is mounted at 185 mm. It should be noted that these ray tracing diagrams use the small angle approximation which is not entirely accurate but was used to give a rough outline that was then optimised during construction.

With this configuration the impact of scattered light should be reduced.

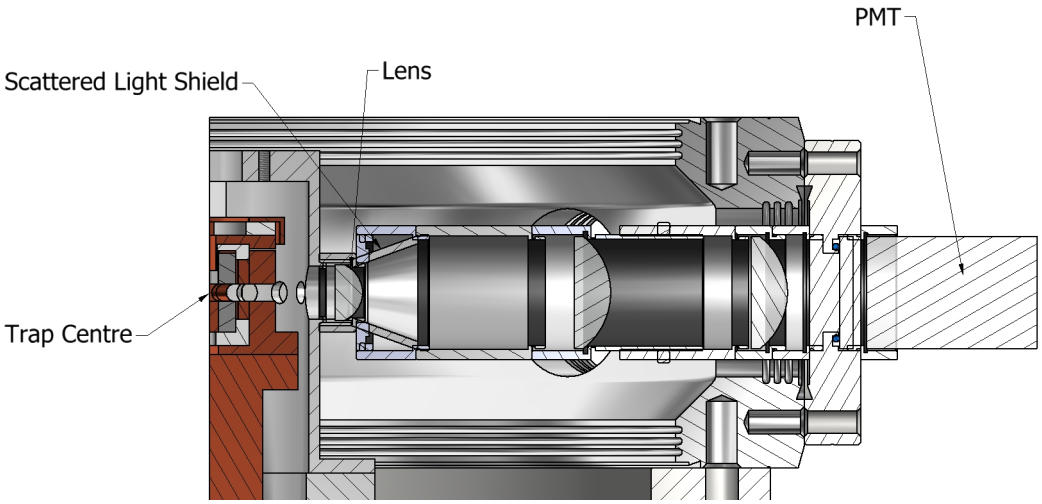

Fig. 3.12 Lens system assembly for LIF detection. Although the first and last lenses are at a fixed position, both the aperture and the second lens can be moved within the lens tube if the lens system needs to be reconfigured. Additionally the last lens can be replaced on the flange with a window allowing for the last lens to be mounted further back.

On account of the improvement in terms of stray light, we decided to utilise the lens system as opposed to mounting the PMT inside the chamber. In order to allow for the greatest ease of access and assembly the most straightforward method to mount these optics is to mount them from the spherical octagon inside a Thorlabs lens tube (see Fig. 3.12). In order to maximise the solid angle collection of the first lens (and therefore examine more of the trap) the first lens needs to be placed as close as possible to the trap centre and hence it was mounted on the outer stage assembly. Although it is feasible to focus the emitted light onto the PMT with two lenses we have opted to use three. The reasoning behind this is that the size of the chamber puts restrictions on where the PMT could be mounted and although a two lens system could focus light onto the PMT, size restrictions of the lens tube and previous experience in the group with two lens systems suggest that a three lens system is preferable. However, the current lens configuration, shown in Fig. 3.11, was designed to be adaptable so that it may be altered if problems were found.

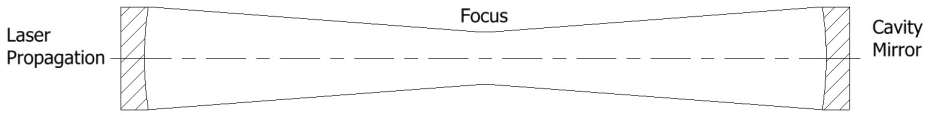

Fig. 3.13 Schematic of confocal optical cavity. This shows the outline of a light beam that fits itself between the mirrors. The rays consisting the outline are curved as a beam of limited width spreads by diffraction.

Cavity-Enhanced Laser-Induced Fluorescence

In terms of constructing the cavity itself, it is not simply a case of mounting and aligning cavity mirrors on each end of the laser axis. In order to maximise the effectiveness of the cavity one needs to consider the behaviour of the laser in the cavity. First if we consider the shape of the cavity mirrors, it is preferable to use confocal mirrors as this will trap the maximum amount of light into the cavity (see Fig. 3.13). The exact shape of the pathways shown in Fig 3.13 is determined by the nature of the laser beams themselves. Laser beams that couple into optical cavities are usually of Gaussian-Hermite form. As these beams propagate the curvature of their wavefronts and the diameter of the beam will vary as function of distance. This is described by the equations [105]

$$R(z) = \frac{z^2 + z_R^2}{z}, \tag{3.12a}$$

$$\omega(z) = \omega_0 \left(1 + \left(\frac{z}{z_R}\right)^2\right)^{1/2} \tag{3.12b}$$

where z is the direction of propagation, R is the radius of curvature of the wavefront, ω is the radius of the spot size (where the intensity of the spot has dropped to $1/e$ of the maximum), ω_0 is the minimum radius of the beam (known as the beam waist) and z_R is the Rayleigh range which in turn is defined by the equation

$$z_R = \frac{\pi\omega_0^2}{\lambda} \tag{3.13}$$

where λ is the wavelength of the laser light. For a symmetric cavity in order to maintain low loss modes the cavity must obey the condition

$$0 < \left(1 - \frac{L}{R_M}\right)^2 < 1 \tag{3.14}$$

where L is the length of the cavity and R_M is the radius of curvature. As shown in Fig. 3.13 in the symmetric cavity the beam waist lies in the centre or at $\frac{1}{2}L$, which means that $R(\frac{1}{2}L) = R_M$ for a cavity mode. Substituting this into Equations 3.12a and 3.12b we find that the beam waist is given by

$$\omega_0 = \sqrt{\frac{\lambda}{2\pi}} \left(2R_M L - L^2\right)^{\frac{1}{4}}. \tag{3.15}$$

As we wish to probe as many molecules as possible it is advantageous to maximise the size of the beam waist. If equation 3.15 is differentiated with respect to L and set to zero we get

$$\frac{\partial \omega_0}{\partial L} = \sqrt{\frac{\lambda}{8\pi}} \left(R_M - L\right) \left(\left(2R_M - L\right) L\right)^{-\frac{3}{4}} = 0. \tag{3.16}$$

From this it appears that there are three solutions for the optimised length namely $L = R_M$, $L = 2R_M$ and $L = 0$. The latter is obviously not viable but the first two can both be used. If we consider the first two scenarios along with equation 3.15 by setting $R_M = L$ the revised equation for the beam waist is

$$\omega_0 = \sqrt{\frac{\lambda L}{2\pi}}, \tag{3.17}$$

and by setting $R_M = \frac{L}{2}$ the beam waist is given by

$$\omega_0 = \sqrt{\frac{\lambda}{2\pi}} \left(2\frac{L}{2}L - L^2\right)^{\frac{1}{4}} = 0. \tag{3.18}$$

Hence based upon this the optimum cavity length and mirror radius of curvature is $R_M = L$. Additionally this shows that for longer cavities and mirrors with larger radii of curvature we will produce a larger beam waist. However there are still limits

in terms of the practicality of constructing the cavity itself and the availability of the mirrors with the required radius of curvature. On account of this we elected to use a 1 m long cavity and a beam waist of approximately 227 µm.

In order for this cavity to be realised there needs to be some method to mount the cavity mirrors in place. For this, specialised cavity mirror mounts have been designed as shown in Fig. 3.14. This mount not only holds the mirrors in place but also allows for the alignment of mirrors using fine adjustment screws.

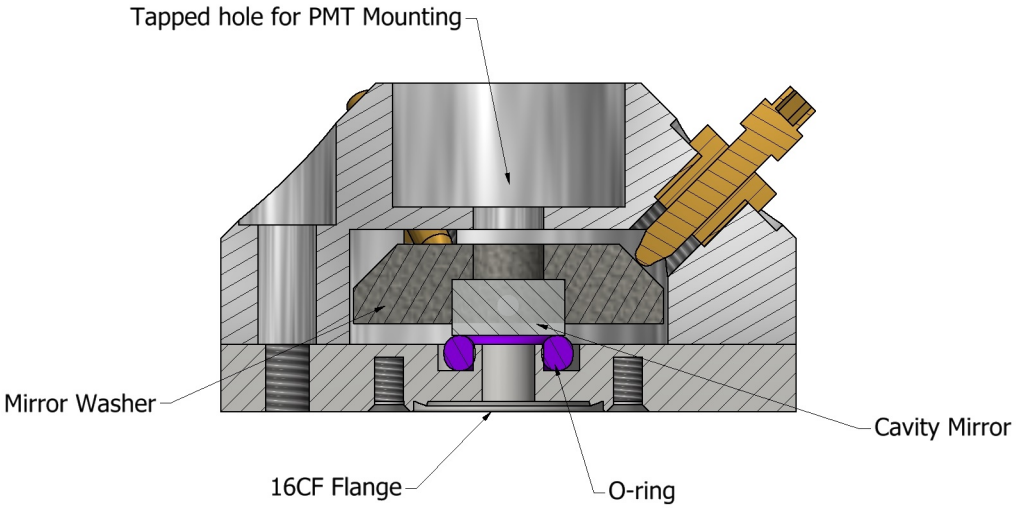

Fig. 3.14 Schematic cross-section of cavity mirror mount. This assembly can be directly mounted onto a 16 CF flange and the mirrors aligned with the precision screws. There are three precision screws arranged 120° from each other. As they are tightened the screws will push on the mirror washer and adjust the angle of the mirror. The mirror washer serves to protect the mirror and precision screws from damage by over-tight contact and allows for space to mount the PMT directly into the mount.

Resonance Enhanced Multi-photon ionisation (REMPI)

For the REMPI measurements a specialised configuration of elements is required in order to optimise the ion detection. As previously mentioned, the primary element is a specialised set of ion optics in order to guide the ionised molecules to the detector. To design these ion optics, specialist simulation software (SIMION) was applied and a variety of configurations simulated until a final configuration was decided upon.

The simulations indicated a preferred configuration of ion optics which incorporated the magnets as electrodes (see Fig. 3.15). During the simulation process efforts were

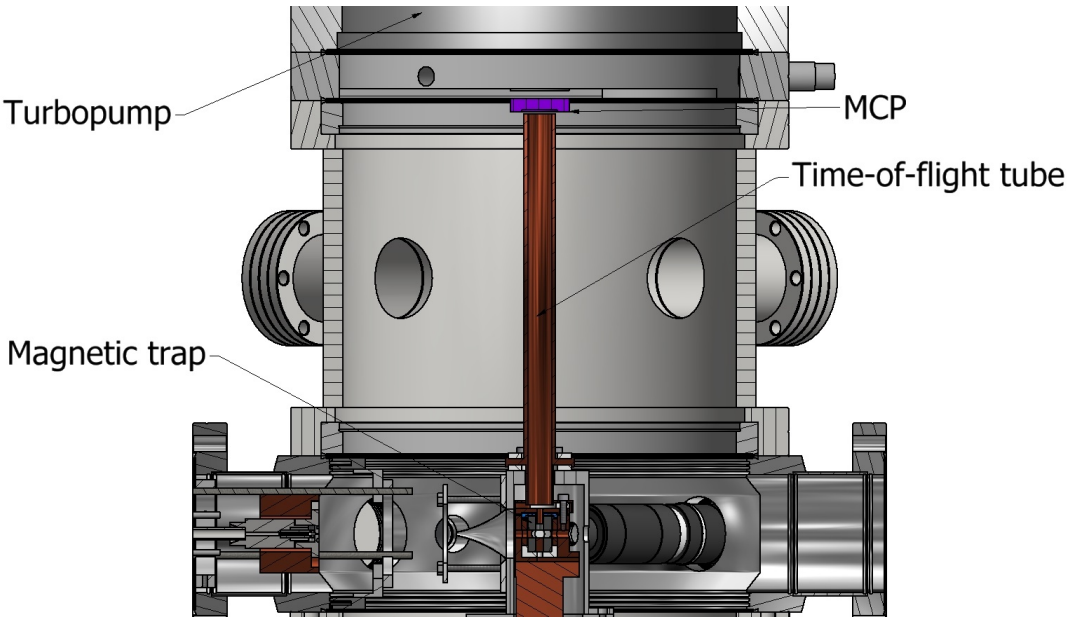

Fig. 3.15 Ion Optics assembly used for REMPI detection. Each component is electrically isolated using boron nitride and the electrical feedthroughs are fed into the chamber via dedicated ports.

made to both maximise the number of ions from the trap that reach the detector along with the mass resolution of the ions. However in practice this was not found to be fully feasible and so we have opted to provide the utility of two different modes of operation: a signal maximising configuration and a mass resolving configuration (see Fig. 3.16). To illustrate the differences between these two modes of operation simulations were performed by generating a 10 mm line of SH and SD molecules perpendicular to the direction of the extraction and recording the time of arrival at the microchannel plate (MCP). The results of this are shown in Fig. 3.17.

Table 3.1 Voltages applied to each of the components for the two ion-optics settings. V1 and V2 are the lower and upper magnets respectively, V3 is the extraction tube and V4 is the ion shield (also referred to as the time-of-flight tube).

	V1	V2	V3	V4	MCP
Signal Maximising	0 V	0 V	−100 V	−400 V	1 kV
Mass Resolving	1 kV	400 V	−300 V	−400 V	1 kV

As shown in 3.17 there are significant differences between the ion times of flight using the different configurations. The most notable difference is in the magnitude

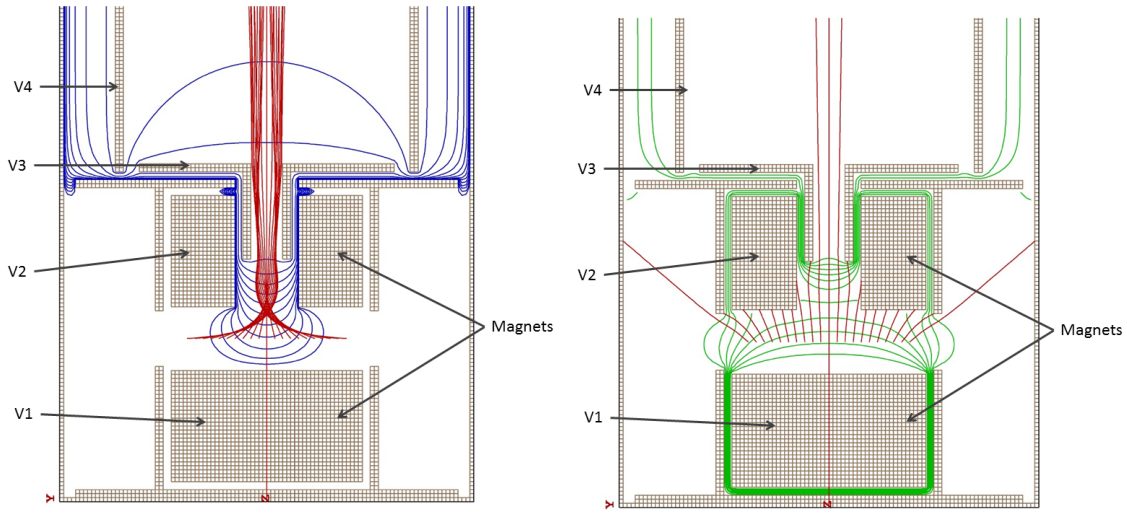

(a) Signal-maximising configuration (b) Mass resolution configuration

Fig. 3.16 SIMION simulations of the ion optics configuration with potential contours and example ion trajectories. The blue contours halve in size from top to bottom starting at $-320\,\mathrm{V}$ and the green contours are evenly spaced from $-200 - 800\mathrm{V}$, increasing from top to bottom. With the configurations shown there are two modes for either maximising the signal or allowing mass resolution and for each, different voltages are applied to each of the electrodes.

of the flight times as the signal-maximising configuration gives ions a much longer time of flight. This is a result of the relatively shallow potential gradient that the ions experience from the extraction tube as shown in Fig. 3.16. This results in a slower extraction from the trap and onto the MCP, ultimately leading to longer flight times. Additionally the spread in ion arrival times is much larger when using the signal maximising mode with a long tail of ions at longer flight times. This is also likely due to the slow extraction of the signal maximising mode which means that the ions at the wings of the extraction volume take significantly longer to reach the detector. In any case it is clear from this that given the temporal breadth of the signal maximising configuration and minimal difference between the different mass peaks, it is not suitable for distinguishing different mass peaks, hence the necessity of the mass-resolving configuration.

In order for this configuration to be applicable, the MCP needs to be mounted directly above the centre of the magnetic trap at a sufficient distance to allow for the TOF signal to distinguish between different masses. In order to meet the length requirement a custom built extension piece is required as shown in Fig. 3.15, with

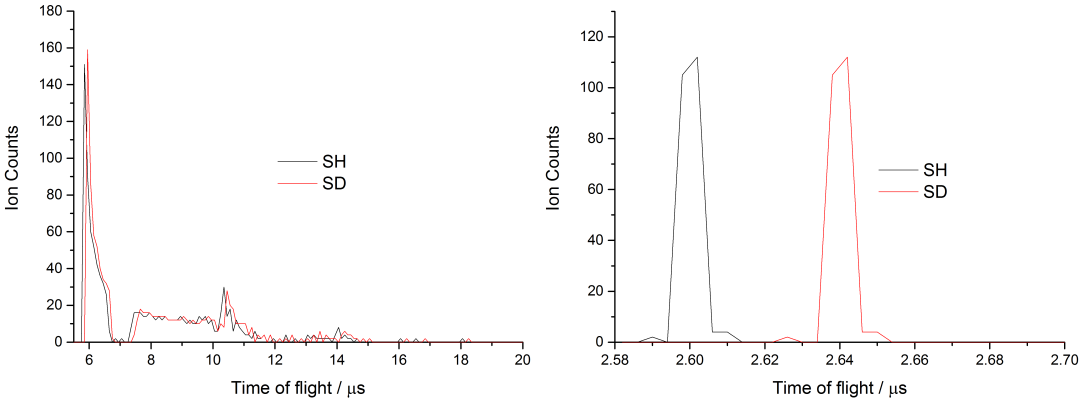

(a) Signal maximising (b) Mass resolution

Fig. 3.17 Time of flight SIMION simulations for the signal maximising and mass resolving configurations of the ion optics.

additional 35 CF ports added to provide additional access for other monitoring processes (see Section 3.8.2). It was decided early on that in order to maximise pumping and minimise the volume of the chamber that the turbopump would be mounted directly above the cryostat. This means that the MCP needs to be mounted in-between the two, thus making it impossible to perform VMI without mounting the phosphor screen and camera in vacuum. Instead, as shown in Fig 3.15, the MCP needed to be mounted on a double-sided 200 CF flange with the electrical feedthroughs required connected radially through the flange.

As with the PMT, in order to consider the potential for noise in the system we must examine the workings of the MCP. A microchannel plate is a slab of highly resistive material typically of $< 2\,\text{mm}$ thickness with a regular array of tiny tubes or mirochannels through it which are densely distributed over the surface. The microchannels are in the order of $10\,\mu\text{m}$ in diameter with spacings of around $15\,\mu\text{m}$. They are also parallel to each other and often enter the plate at a small angle to the surface. Each microchannel acts as an electron multiplier in the presence of a strong electric field. Due to the angle of the channel in relation to the plate, particles or photons that enter the channel are guaranteed to hit the channel wall. This impact starts a cascade of electrons that propagates through the channel, thus amplifying the signal. The electrons produced exit the channels on the opposite side where they are detected by another means.

Often two microchannel plates are used to achieve the required gain of electrons and they are arranged in a chevron configuration so that ions cannot fly through them without impacting the channels and generating an electron signal. In this case the electrons that exit the first plate start the cascade on the second. This gives greater gain than a single plate configuration and reduces ion feedback.

For our MCPs we elected to use a Hamamatsu F12334-11 model, which was mounted on a specialised double-sided 200 CF flange with electrical and output connections fed in radially. The internal electronics of the MCPs were configured such that there is a negative potential bias at the face of the MCPs and the emitted electron signal is collected by a grounded anode.

In terms of noise considerations, assuming any ion gauges in the chamber are switched off, there is unlikely to be very many ions in the chamber that are not produced by the REMPI process and so the background noise on this front should be reduced. As with the PMT, the output voltage from the MCP was fed into an oscilloscope using coaxial cables to reduce noise from external electrical signals.

Molecular Beam Profiling

In order to test the efficiencies of different molecular beam sources it would be highly advantageous to allow for some mechanism to monitor the molecular beam profile. To this end this design incorporates a number of different monitoring devices to fulfil this function.

The primary molecular beam monitoring components are all housed on a Kimball Physics spherical square (see Fig. 3.18). It was the intention to allow the incorporation of three different methods for monitoring the molecular beam in this structure, namely: an optical cavity, a MCP and a fast ionisation gauge (FIG). It should be noted that for the course of this experiment only the FIG apparatus was constructed, although the other components could easily be added later.

For the optical cavity, as is the case for the LIF measurements, both CRDS and CELIF can be performed on the beam as it passes through. CRDS can be used to

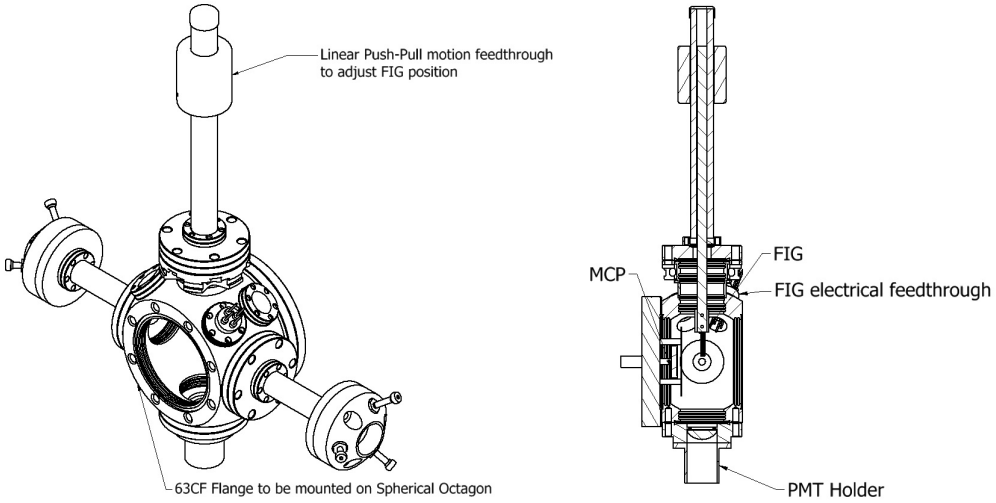

(a) Spherical Square Assembly (b) Spherical Square Cross-Section

Fig. 3.18 Schematic of the proposed Spherical Square assembly for molecular beam monitoring. For 3.18(b) this is a half section view from a plane perpendicular to the cavity axis.

monitor the molecular beam profile by taking readings of the change in RDT (when compared to vacuum) at different delays between the nozzle and the laser. This will allow measurements of the number density of molecules in the cavity as a function of time and thus show the shape of the molecular beam. Additionally it could be potentially feasible to perform CELIF on the beam to allow a direct comparison between the beam and the molecules held in the magnetic trap.

As shown in Fig 3.18 an MCP is situated directly on the molecular beam path. In a similar fashion to the use of CRDS, the MCP could be used to monitor the molecular beam by measuring the output in voltage over a set time period to give the longitudinal shape of the molecular beam.

The most direct approach to monitoring the molecular beam would be to use the FIG. The FIG is a Bayard-Alpert hot filament gauge consisting of a filament, a grid and a collector wire. An electron current is emitted from the heated filament and the electrons are attracted to the grid by a potential of around 160 V. Most of the electrons pass through the grid and collide with gas molecules in the enclosed volume, which ionises some of them. These ions are attracted to the collector and the current that results from their impact is amplified to give a measure of the number

of gas molecules. In distinction to the standard Bayard-Alpert gauges, the FIG is specially optimised to give a fast response time by having a smaller grid so that it can effectively measure the changes in pressure in detail along the length of the molecular beam. If the FIG is placed in the path of the molecular beam it can give a measure of the number of gas molecules passing through it as a function of time and hence gives a molecular beam profile. Instead of mounting the FIG in the molecular beam path permanently, it is mounted on a linear push-pull feedthrough to allow for the greatest flexibility. Additionally we are incorporating into the design the capability of mounting an additional FIG onto the outer stage shielding to monitor the pressure near the trap centre.

Additional monitoring methods

In addition to the primary measurements that have already been outlined there are a number of other parameters that need to be monitored in order to optimise the experiment. The most significant of these is the vacuum pressure of the chamber as this has a major role in the experiment. Additionally the temperature of the two stages on the cryostat should also be measured. Another factor to be considered is that of leak detection for the chamber and how to monitor the contents of the chamber (i.e. to determine if there is contamination in the molecular beam).

For the sake of vacuum measurement we adopted a number of Pirani and ion gauges. A Pirani gauge consists of a metal filament suspended in a tube that is connected to the system to be measured. The filament is heated and when gas molecules collide with it the filament will lose heat. As the rate of heat loss is directly related to the number of gas molecules present measuring it is a direct indication of the pressure. Ion gauges operate using the same operational principles as the FIG outlined above. The primary pressure measurement of the chamber used a combination Pirani and ion gauge mounted on an unused port of the spherical octagon or on the extension piece. It should be noted that this will measure the ambient pressure in the chamber, but in the trap itself this is likely to be much lower on account of the pumping factor of the cold surfaces of the cryostat.

In order to monitor contamination and detect leaks we opted to use a Hiden Analytical (HALO 201-RC) residual gas analyser (RGA). A RGA is a small mass spectrometer that can be connected directly to a vacuum system and analyses the gases inside it. There are three main components to the RGA: an ion source, a mass analyser and a detector. The ioniser consists of a hot emission filament which produces an electron beam for ionising the gas in the system. After the ionisation the ions are sorted according to mass by the mass analyser. This is commonly performed by use of a radio-frequency quadrupole which prevents the ions with the incorrect mass-to-charge ratio for the given frequency from passing onto the ion collector, thus sorting the masses of the ions. These sorted ions are then measured using the detector, which may be either a Faraday cup or an electron multiplier depending on the sensitivity of the frequency range used. The RGA produces a mass spectrum which allows us to observe what gases are in the chamber and thus if there is an unexpected reading on the RGA (e.g. large amounts of N_2) or by performing a He leak check then it will be apparent that there is a leak. Both of these options are viable and they may be used in combination.

In terms of temperature measurements of the cryostat, the ideal method to monitor this would be to use a calibrated resistor. Essentially this would be a resistor where the resistance had been measured for cryogenic temperatures and therefore a direct measurement of the resistance will provide a means to determine the temperature. However, realistically the exact temperature of the cryostat is not, at this stage, vital to the experiment so precise measurements would not be required. Therefore, for the sake of simplicity, we opted to use a flange mounted K-type thermocouple, which was secured onto the outer stage of the cryostat.

Part II

CAVITY-ENHANCED LASER-INDUCED FLUORESCENCE

4. N_2 RAYLEIGH SCATTERING CROSS-SECTION MEASUREMENTS

4.1 Introduction

The initial experiments performed were focused on the measurement of the Rayleigh scattering cross-section of N_2 (σ_{N_2}) between 320 nm to 325 nm using cavity ring-down spectroscopy (CRDS). At first, the reasoning for this at the time was to complement a concurrent experiment which utilised cavity-enhanced laser-induced fluorescence (CELIF) for absolute density measurements of SD molecules [104]. However, these measurements could not be taken within sufficient time for use in that experiment. These experiments continued after the aforementioned paper had been sent for publication as it was deemed that accurate values for σ_{N_2} could be useful for the calibration of CELIF detection systems in circumstances where there is insufficient molecules for a measurable change in ring-down time (RDT).

4.2 Experimental

The vacuum chamber was set up as shown in Fig. 4.1. The chamber was evacuated using a rotary pump (Oerlikon Leybold DC65), allowing the chamber to reach pressures in the order of $\approx 10^{-4}$ mbar (measured using a Pfeiffer Vacuum Compact Fullrange BA gauge). A nitrogen supply was attached to the chamber with a regulating valve to provide a nitrogen supply to the chamber with a dry ice trap to remove any water from the system and ensure purity. With the nitrogen line filled with a high pressure (≈ 2 bar) and the valve to the rotary pump closed, the valve to the N_2 supply was partially opened. This allowed for N_2 to slowly fill the chamber

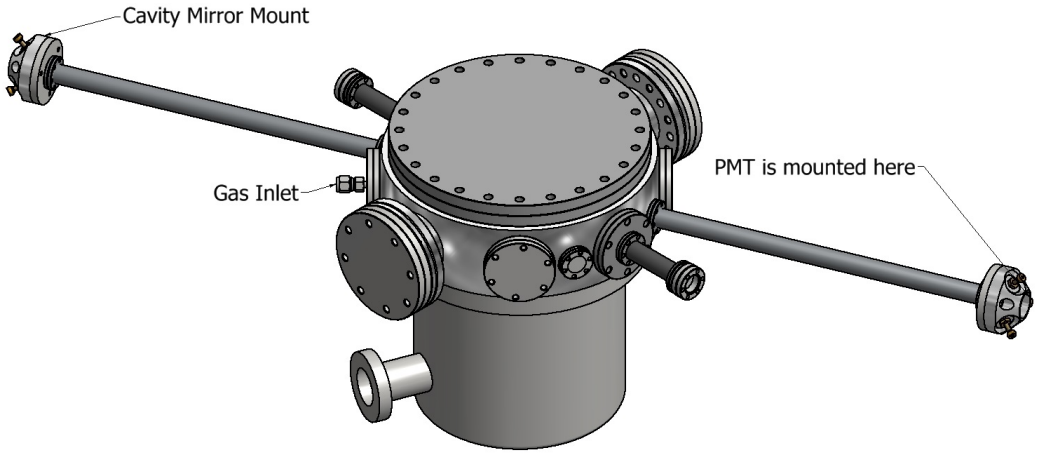

Fig. 4.1 Schematic diagram of chamber used for the Rayleigh Scattering Cross-section measurements.

which would slowly increase the round trip losses from the cavity ring-down process. As this leak was occurring, the ring-down transient was recorded and measured simultaneously with the chamber pressure (measured using a Pfeiffer APR260 piezo gauge). From this the ring-down time was recorded as a function of pressure and hence the Rayleigh scattering cross-section could be determined.

Laser wavelengths used were between 320 nm to 325 nm and generated using the aforementioned dye laser (Sirah, CobraStretch). A DCM laser dye (Exciton) was used and pumped using the second harmonic (532 nm) of a Surelite Continuum Nd:YAG laser with a 10 Hz repetition rate. The emitted light was frequency doubled using a frequency conversion unit from Sirah. The doubled light was guided into the cavity with the use of a set of three UV-enhanced aluminium mirrors. Additionally the size of the probe laser was reduced using a 2:1 telescope and a coupling lens was placed directly in front of the cavity entrance. The purpose of this is to ensure that the majority of the laser is coupled into the central transverse mode of the cavity (the TEM_{00} mode) and the coupling lens is placed at a distance to ensure that the laser light enters the chamber at an angle that matches the shape of the TEM_{00} mode.

A major issue with previous experiments using this method is that of the cavity mirrors moving with pressure changes in the chamber. To counter this the new mirror mounts were specifically designed to hold the mirrors as tightly as possible

and during the experiment the mirrors were secured as tightly as possible so that a good vacuum tight seal is maintained but the mirror positions cannot significantly move. A more detailed overview of these mounts was given in 3.8.2.

The ring-down photomultiplier tube (PMT) was mounted inside a Delrin cylinder that was screwed into the mirror mount to avoid detecting ambient light. The ring-down signal was digitised by a 12-bit digitiser PCI card (National Instruments PCI-5124, 150 MHz, 200 MS s^{-1}). A LabVIEW program processed the signal to ensure any baseline voltage is compensated for as well as selecting particular portions of the trace for measurement. More specifically, to remove the baseline, a portion of the trace on the oscilloscope from before the laser was fired was averaged and subtracted from the total signal. The measurements of the ring-down time were obtained by using a least-squares exponential fit on a portion of the ring-down trace after the start of the decay so as to remove any biasing contribution from uncoupled light into the cavity[1].

4.3 Results

During the initial stages of the experiment the leak rate of the nitrogen was altered to examine the precision of the different measurements. From this it was found that slower leak rates tended to produce more precise results (which stands to reason as there will be more data points to fit to). An example of one such run is shown in Fig. 4.2. This shows clearly that there is a linear trend as the reciprocal of the RDT increases with pressure. This was fitted using a linear least-squares fit for each measurement which routinely produced uncertainties in the gradient (and thus the measured cross-section) of less than 1 %. However there is a great deal of scatter in the results which is a result of variations in the measurement of the RDT. Although in principle the RDT should not change with the shot-to-shot variations of intensity from the dye laser, there will still be a certain degree of spread in the final results.

[1] This is in reference to an initial spike we observed at the start of the ring-down decay which was a result of not all of the probe laser being coupled into the cavity and therefore not reflecting back and forth between the mirrors and just passing straight through.

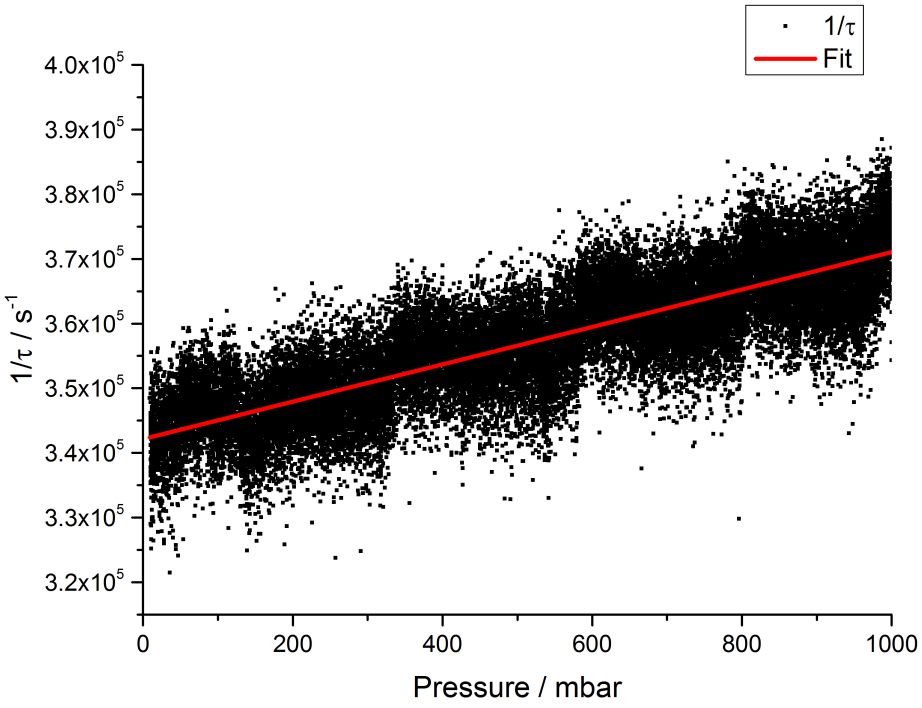

Fig. 4.2 Plot of pressure against $1/\tau$ for a single cross-section measurement taken at 325 nm. The fit line shown is a least squares fit.

A possible reason for this is that the laser beam from the dye laser is not entirely Gaussian. The output from the dye laser has an oval shape meaning that there may be some variations in the beam shape between laser shots thus affecting the shape of the RD trace. During the process of aligning the cavity efforts were made to attempt to minimise this as well as lengthen the RDT in order to counteract this issue. Specifically the telescope was used to adjust the beam profile of the dye laser by focussing the laser to a point and using a 50 µm optical pinhole positioned at this point to reshape the beam profile by blocking the non-circular aspects of the profile.

After a number of attempts at different wavelengths in the given region it was found that although the linear fits on the individual measurements of $\frac{1}{\tau}$ against pressure were precise, repeated measurements at the same wavelength would yield significantly different results as illustrated in Fig. 4.3. On account of this variation it is difficult to definitively observe a distinguishable difference between the higher and lower wavelengths in this region.

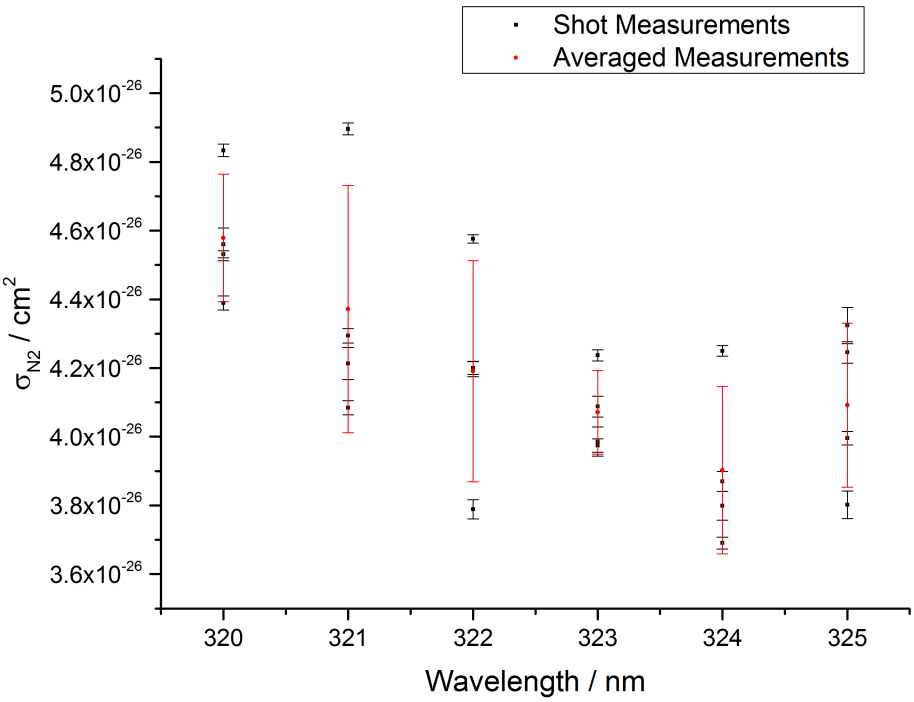

Fig. 4.3 Plot of measured N_2 Rayleigh Scattering cross-sections over the wavelength region of 320 nm to 325 nm. The red vertical error bars represent the standard deviation of the averaged measurements and the black points represent a selection of the individual measurements of σ_{N2} such as the one shown in Fig 4.2.

4.4 Discussion

Owing to the significant variation in the measurements taken at each wavelength there is insufficient evidence here to define a trend in the Rayleigh scattering cross-section or give absolute values for specific wavelengths. The primary reason for this seems likely to be the variation in temperature over time due to cycles in the air conditioning. This is evident in Fig. 4.2 from the periodic spikes and dips in the $1/\tau$ value. The most obvious effect this would have is that it would alter the calculated number density of the molecules from the ideal gas law:

$$P = \rho k_B T, \tag{4.1}$$

where P is the pressure (corrected for the calibration of the piezo gauge) and k_B is the Boltzmann constant. However, if we consider this further, it is unlikely that small changes in temperature will have a significant impact on the pressure. Another

possibility is that slight changes in temperature may result in a change in alignment on account of the thermal contraction/expansion of the chamber. Although this effect would be small, the CRD signal is highly sensitive to the laser/cavity mirror alignment so even on this small scale subtle changes may have had a significant impact.

Unfortunately due to the heat generation from the rotary pump the air conditioning could not remain off for a significant time without leading to an increase in the chamber temperature and thus the same effect. An alternative would be to make continuous measurements of the temperature in the chamber along with the RDT and pressure measurements. To do this a USB thermocouple adapter was obtained but not in time to be incorporated into these measurements.

Another issue with this experiment is that of small movements of the mirrors as a result of pressure changes in the chamber. Although some steps were taken to reduce this (namely by tightening the mirrors to the point where the would not move) there is still some evidence of a small amount of movement in the mirror positions. A simple way of reducing this would be to construct the optical cavity in such a way that the cavity mirrors remain secured in vacuum. If the cavity is pre-aligned before pumping out, the effects of pressure changes in this circumstance should be minimal as there are no flexible o-rings involved. However in order to be able to align this effectively the mounts themselves would have to be far larger than the current photostop chamber will allow. Also for a system to incorporate such a cavity it would require an increased amount of volume over a long distance in order to facilitate long RDTs and hence provide a lot of volume which will make the chamber harder to evacuate effectively.

4.5 Conclusions and next steps

To summarise, although each set of results is highly precise the lack of accuracy and repeatability mean that definitive values for the Rayleigh scattering cross-section in this region could not be obtained. However with a few alterations, namely the

continuous measurement of temperature or some form of temperature stabilisation, the accuracy and repeatability of these results could be significantly improved thus allowing for more precise measurements to be made. Unfortunately the time was not available to further pursue this enquiry at this time, but this experiment (or a variation on it) may be revisited in the future. Despite the difficulties in this measurement the possibility of calibrating the absolute number density measurements from CELIF remains via a direct calibration using cavity ring-down spectroscopy. Therefore we proceeded to undertake CELIF measurements of a molecular beam.

5. CELIF OF SO_2

5.1 Introduction

To serve as an initial test for the measurement apparatus of the machine we decided to perform cavity-enhanced laser-induced fluorescence (CELIF) on a molecular beam of SO_2. The primary purpose of these experiments was to test the limits of sensitivity of the CELIF technique, however we also took the opportunity to further characterise the nature of the fluorescence signal as well as determine the accuracy of the absolute number density measurements taken using CELIF when compared to cavity ring-down spectroscopy (CRDS).

5.2 Experimental

The probe laser set up was altered from the previous Rayleigh scattering measurements (in chapter 4) on account of difficulties with alignment that occurred from small changes in the telescope lens position. To compensate for this, the telescope was moved from being positioned directly in front of the first cavity mirror, to reside in-between the first and second alignment mirrors. This meant that the second and third alignment mirrors were used to centre the telescoped laser beam on the cavity axis. The primary addition to the optical arrangement was the inclusion of a second photomultiplier tube (PMT) with a lens system mounted on a specialised 35 CF flange on one of the 45° 35 CF ports of the spherical octagon. This additional detector was for the measurement of the emitted fluorescence and shall be henceforth referred to as the fluorescence PMT. Further it should be noted that at this point in the experiment the internal structure of the chamber was not installed and the

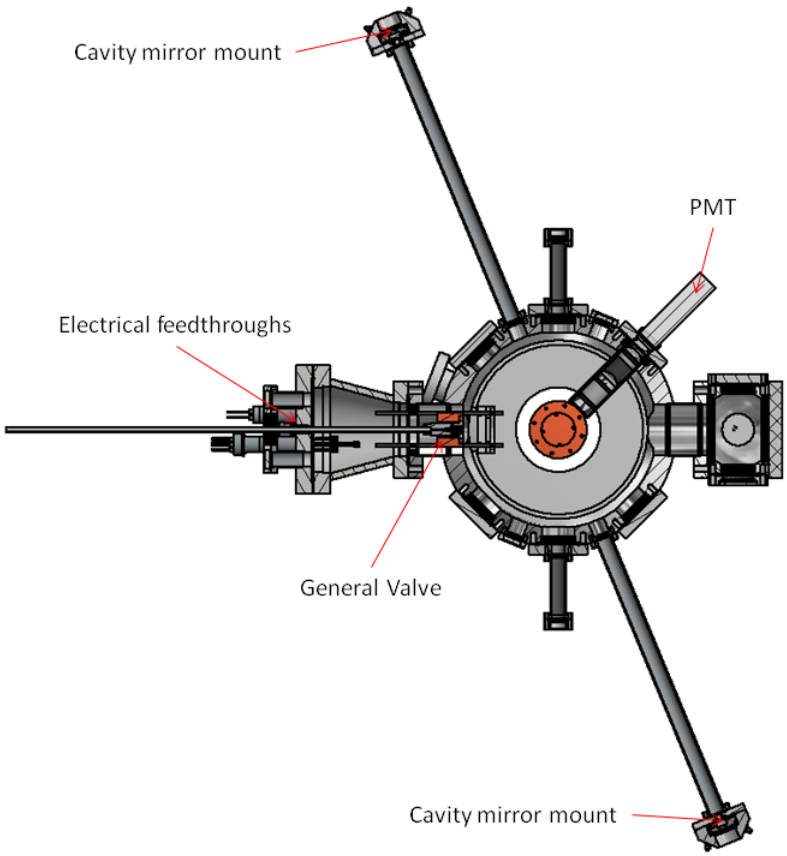

Fig. 5.1 Schematic diagram of chamber used for CELIF of SO_2. The lenses in the LIF optics are positioned to be in the equivalent position as for the fully constructed photostop chamber (see Fig. 3.11).

molecular beam is unskimmed.

The molecular beam for these measurements was provided by a Parker Series 9 General Valve controlled by an Iota One control box. The SO_2 was supplied using a specialised gas mixing system and was used pure for the majority of measurements with a consistent 1.5 bar backing pressure at the nozzle.

A Quantum Composers series 9000 pulse generator was used as the primary control source for the experiment. Specialised LabVIEW software was written to allow for each channel of the pulse generator to be manipulated in an automated process.

The fluorescence signal was measured from the output of the fluorescence PMT, which was connected to the digitiser card and processed to remove the baseline (as with previous CRDS measurements) with a section isolated for measurement of the fluorescence signal. The magnitude of the fluorescence signal was measured using two methods; first by taking a numerical integral of the trace and the second by mea-

suring the event (or photon) count of the signal. The photon count of the signal was determined by distinguishing individual spikes on the PMT which were attributed to single photons and counting the number of spikes in a given fluorescence measurement. To distinguish the photons from the background a threshold limit was set above the background noise so that only spikes in signal above this point would be counted. These individual counts could then be averaged over a number of shots to give an clearer picture of the fluorescence signal. Additionally, from an averaged measurement over several shots a temporal picture of the fluorescence can be built to form a photon counting histogram. This entails recording the time point in the trace that each photon is detected at the PMT and, by segregating the fluorescence signal into discrete time bins, generating a histogram of the temporal locations of incoming photons over several shots.

Another addition to the experimental apparatus was a gas mixing cell for preparing different mixtures of the target gas (in this case SO_2). In essence this consists of a 1 L gas cylinder which forms a part of two circuits of 6 mm stainless steel pipes. These two circuits are of different sizes so that when gas enters this systems it will flow around the two different parts and they will return to the central gas cylinder at different times, depending on which path is taken. This will allow for gas mixtures to be more effectively mixed as the different gases will return from each channel at different times, thus allow more a uniform mixing.

For this experiment we examined the fluorescence and absorption properties of SO_2 between 320 nm to 315 nm. This corresponds to transitions from the $^1A_1$ ground state to the $^1B_1$ excited electronic state with a number of distinct vibrational and rotational states contained therein [106].

5.3 Results

In order to perform the required measurements the molecular beam needed to be optimised in order to ensure that the opening of the nozzle produced a short sharp pulse of gas of a high density. To this end the intention was to utilise a fast ionisation

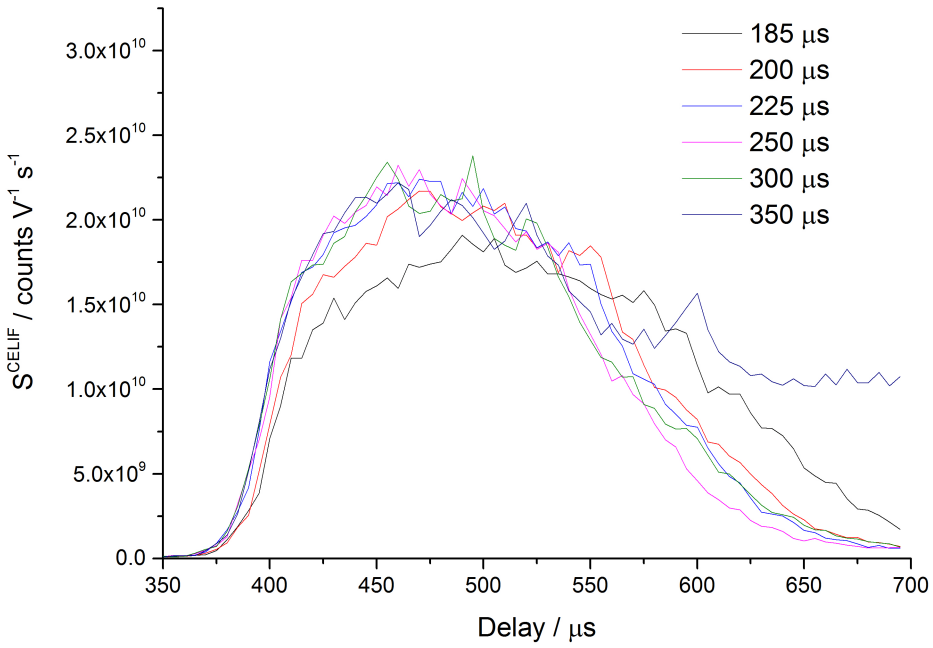

Fig. 5.2 Molecular beam profiles of a pure SO_2 beam at 1.5 bar backing pressure measured using CELIF with different pulse durations. This was measured using a 318.05 nm laser by altering the delay between the firing of the nozzle and probe lasers using the pulse generator and recording the average signal over 10 laser shots at each point.

gauge (FIG) to allow for active manipulation of the pulse width and nozzle position to maximise the number density at the peak of the molecular beam. However technical issues with the FIG prevented this so scans using the fluorescence signal from the probe laser were performed to trace the shape of the molecular beam. This was achieved by altering the delay between the triggering of the General Valve and the firing of the probe laser.

An example of this optimisation process is shown in Fig. 5.2. By altering the nozzle pulse width the length of the current pulse used to open the nozzle changes and therefore, in principle, increasing the pulse length should result in a longer beam pulse. However, the degree that the nozzle will open during the current pulse is also determined by the tightness of the nozzle connection[1]. Thus, by adjusting the pulse width and observing the shape of the pulse from the measured fluorescence signal, the molecular beam profile can be optimised. Performing the optimisation in this manner is not ideal as in order for it to be valid one must assume that the

[1] This refers to an internal component of the General Valve where a spring is used to push a teflon seal (known as a poppet) into the output orifice of the valve. The construction of the valve allows for the tension of this spring to be adjusted by tightening/loosening a threaded connection from the valve face to the valve body.

wavelength being used for the scan corresponds to an absorption/fluorescence from a state that is uniformly distributed in the molecular beam.

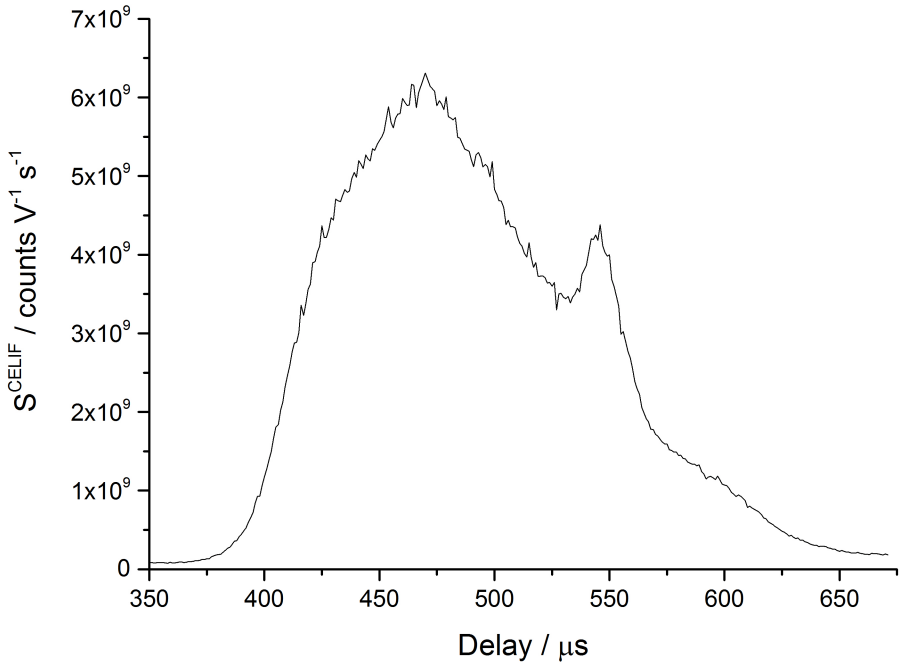

Fig. 5.3 Molecular beam profile of a pure SO_2 beam at 1.5 bar backing pressure measured using CELIF with a 250 µs nozzle pulse duration. This was measured using a 319.74 nm laser by altering the delay between the firing of the nozzle and probe lasers using the pulse generator and recording the average signal over 100 laser shots at each point. The significant artefact here is the secondary peak 100 µs after the main peak.

Another issue that arose from the molecular beam generation is illustrated in Fig. 5.3. The secondary peak occurring around 100 µs after the primary peak was an artefact that would occur for some measurements and not others and the exact nature of this is not certain at this point. One possibility is that, as previously mentioned, the distribution of molecules in the necessary quantum state for the absorption/fluorescence to occur at the given laser wavelength may not be uniform hence producing several peaks across the molecular beam profile. Another potential source for this secondary peak could be a function of the mechanical action of the General Valve itself. Specifically, when the current pulse is switched off the poppet of the nozzle is pushed back to the seal by a spring. It is possible that the poppet may recoil after being pulled back in place, hence effectively giving a second smaller gas pulse superimposed upon the initial pulse. However without a more direct method

of measuring the number density across the molecular beam profile (i.e. with a FIG) the exact nature of this secondary peak cannot be confirmed.

5.3.1 Absolute Number Density Measurements

In previous CELIF experiments [104], the initial number densities of the SD molecules were not sufficient for the CELIF signal to be calibrated with CRDS. Hence for these tests the primary goal is to test this method of calibration. In order to perform this calibration we need to re-examine equations 3.10 and 3.11. By substituting 3.10 into 3.11 we obtain

$$S^{\mathrm{CELIF}} = \frac{1}{c}\left(\frac{1}{\tau} - \frac{1}{\tau_0}\right)\Gamma \cdot \frac{2g}{T}. \tag{5.1}$$

From this the unknown factor $\Gamma \cdot \frac{2g}{T}$ can be found simply by plotting S^{CELIF} against $\frac{1}{\tau}$ and performing a linear fit. Admittedly this could also be done with measurements of α directly from CRDS, however to do this one would have to measure both τ and τ_0 whereas in this method only the RDT with the analyte present is required. This should speed up the process and reduce the uncertainty in the measurement as a calculated value of α would contain the propagated uncertainties of both τ and τ_0 whereas with the single measurement only the error in τ remains. Additionally, using the fit, a value of τ_0 could be obtained from the y-intercept and compared to a measured value to assure the accuracy of the fit.

Using the pure SO_2 molecular beam, the fluorescence signal measured was relatively weak and seemed to vary between a photon counting (a series of individual photon spikes) and a time integrated signal where photons are coming so rapidly that it becomes difficult to distinguish between them on the detector. On account of this the CELIF calibration was performed on both the integral and photon count of the same signal to see if they could both be calibrated in this regime. To perform the calibration, a section of the temporal molecular beam profile was selected where the S^{CELIF} signal drops at a steady rate indicating a slow decline in the number density in the probe volume[2]. Although this calibration could be performed using the entire

[2] In this case we took a section of the tail of the molecular beam, e.g. from 520 µs to 600 µs in Fig. 5.2.

molecular beam profile, if this was done it would be unlikely that there would be an even distribution of measurements over a range of number densities, thus the linear fit would likely be biased.

The fit itself was performed using a linear least-squares fit in much the same manner as the Rayleigh scattering cross-section measurements. This was attempted a number of times with varying degrees of success in terms of the precision of the measurements. One such measurement of the calibration factor is shown in Fig. 5.4. For both the photon counting and integral measurements it is clear that S^{CELIF} is showing a linear trend for increasing $\frac{1}{\tau}$ (and hence α). This data was fitted using a least squares fit, and estimates of the $\Gamma \cdot \frac{2g}{T}$ calibration factors were found to be $(\mathbf{7.1 \pm 0.3}) \times \mathbf{10^{14}}$ m counts $\mathrm{V}^{-1}\,\mathrm{s}^{-1}$ for photon counting CELIF and $(\mathbf{1.01 \pm 0.04}) \times \mathbf{10^{4}}$ m for integrated measurements which corresponds to a $\mathbf{4.06}\%$ and $\mathbf{4.43}\%$ error respectively[3].

Using these calibration factors and spectroscopic measurements of the absorption cross-section from [107], absolute density measurements across the molecular beam profile were taken simultaneously with both CRDS and CELIF to examine the accuracy of these calibration factors as shown in Fig. 5.5.

This graph clearly shows that on the rising and falling edges of the molecular beam profile the CELIF measurements are in a reasonable agreement with the measured CRDS densities. However, at the peak of the molecular beam the photon counting CELIF number densities are significantly lower than the corresponding CRDS measurements. This is likely a result of the limited sampling rate of the digitiser (200 MS/s) which means each sample point is taken at 5 ns intervals. Additionally in this high signal regime there is the possibility that two photons would hit the PMT in a very short time interval apart, meaning that the photon counting algorithm could not distinguish the two photons and hence the photons are under-counted.

[3] In terms of the units for these values, as previously stated, this is dependent on the nature of the measurement. So, for the integrated measurements, we take a value of the integral of the PMT signal and calibrate it with the integral of the CRDS trace (by dividing the former by the latter). These units cancel each other out, leaving the m term to cancel the m^{-1} from the value of α in order to give an arbitrary value of CELIF signal. Similarly, the units of the instrument dependent factor for the photon counting measurements have been chosen to cancel out the other units in the same manner.

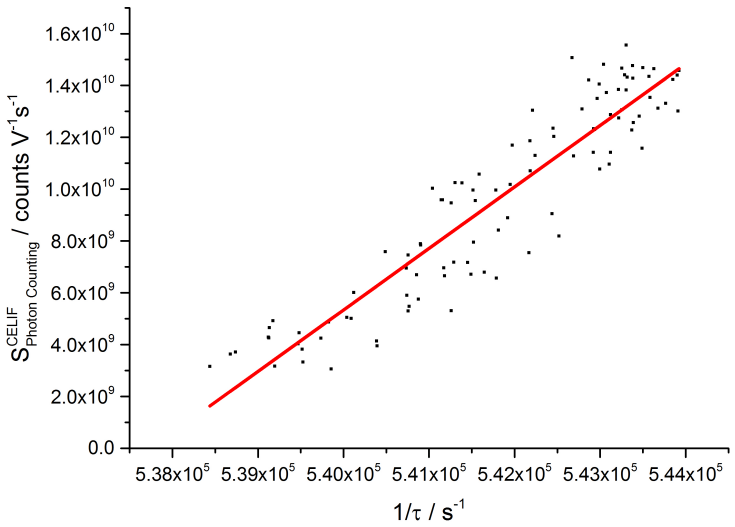

(a) Photon Counting Calibration

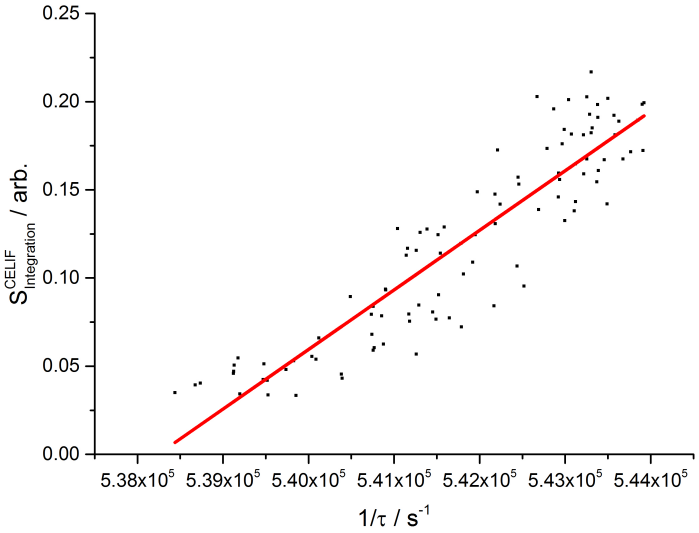

(b) Integral Calibration

Fig. 5.4 $\frac{1}{\tau}$ against S^{CELIF} using the SO_2 molecular beam with a 318.05 nm probe laser. This was performed with both the measured integral and photon counting CELIF signals by measuring the CELIF signal over the falling portion of the molecular beam profile.

The effect of this under-counting is also made evident by the fact that the integral CELIF is marginally more consistent with the CRD measurements than the photon counting signal. However there is still an inconsistency between these results, which is most likely a result of the high uncertainty in measurement of what amounts to a noisy signal, i.e. a multitude of photons.

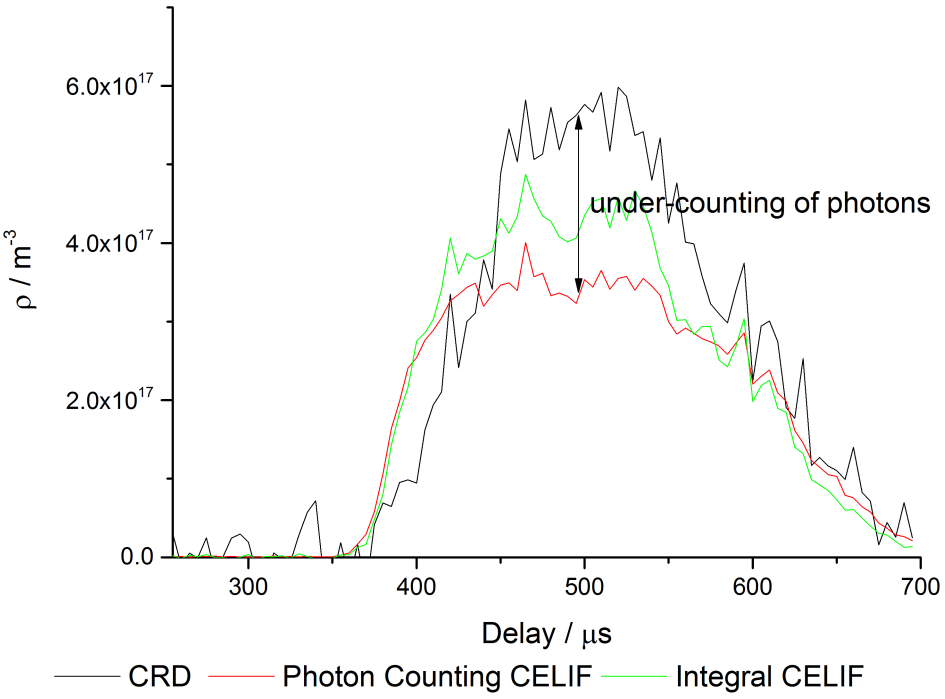

Fig. 5.5 Measured number densities using CELIF (with the measured calibration factors) and CRDS across the molecular beam profile using a 318.05 nm probe laser.

5.3.2 Characterising the CELIF Signal

In order to fully characterise the CELIF signal one must consider exactly how it is formed. In essence one can consider the cavity ring-down trace as a series of single passes back and forth through the sample. This being said it would be reasonable to assume that the fluorescence signal that arises from this would simply be a summation of fluorescence signals generated from each round trip in the cavity. Therefore the CELIF fluorescence signal should take the form of a convolution of a single-pass fluorescence signal and the ring-down trace.

Based upon this assumption, averaged ring-down traces as well as CELIF photon counting histograms were recorded at several peaks in the spectrum of SO_2. Additionally the chamber was reconfigured by replacing the cavity mirror mounts with windows so that conventional single-pass LIF could be performed and traces from this were also recorded at the aforementioned peaks. The recorded LIF and ring-down traces are shown in Fig. 5.6.

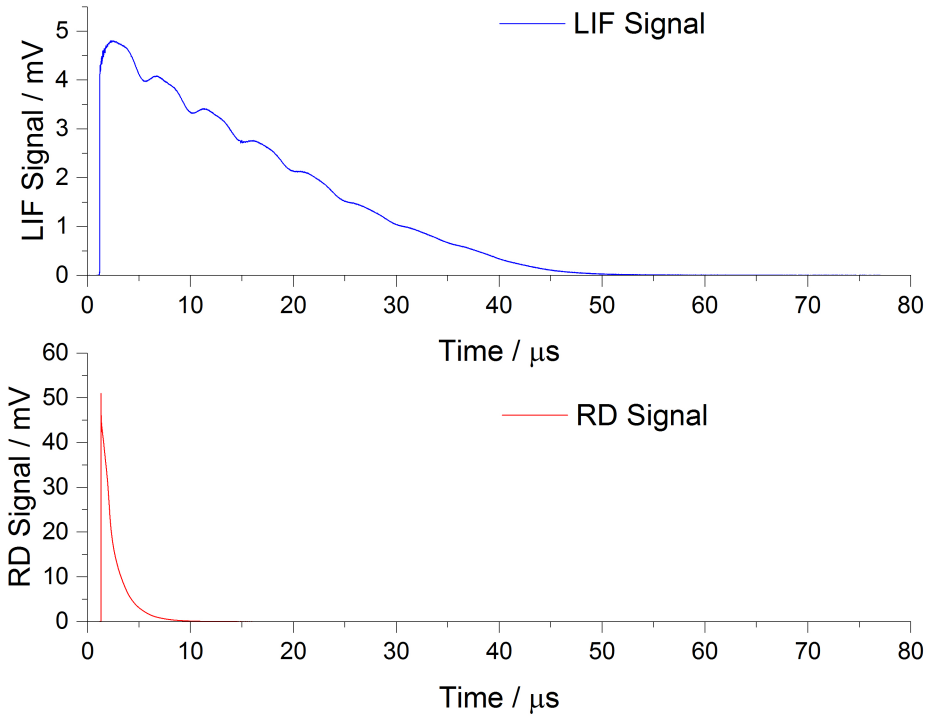

Fig. 5.6 Recorded LIF and RD traces at 318.05 nm.

A point of interest in the fluorescence signal is the apparent oscillations on the decay. This appears to be the result of a phenomenon known as quantum beating whereby the wavepackets from transitions in each fluorescence pathway interfere with one another generating some variation in the fluorescence intensity at a 'beat' frequency. This has been shown to be indicative of rotational level mixing between the $\tilde{A}^1A_2$ and the $\tilde{B}^1B_1$ vibronic states which are near resonant and observed in SO_2 previously within this region [108].

Taking these recorded signals, a numerical convolution was performed as can be seen in 5.7(a). Upon a qualitative comparison with the recorded photon counting histogram shown in Fig. 5.7(b) it is clear that there are significant differences between the two traces. Of particular note is the fact that the CELIF photon counting histogram has a significantly faster initial decay before a seemingly slower decay occurs.

To further examine this a convolution of the mathematical definitions of both the RD trace and the LIF trace was performed. For this the RD trace was defined by

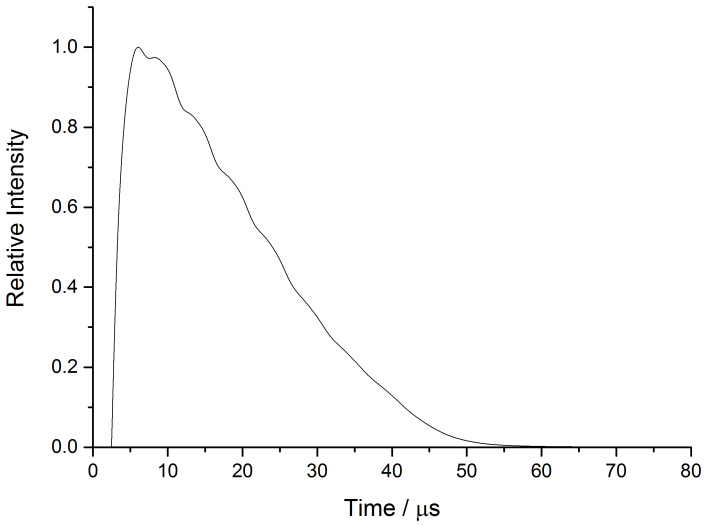

(a) Convolution of RD and LIF traces

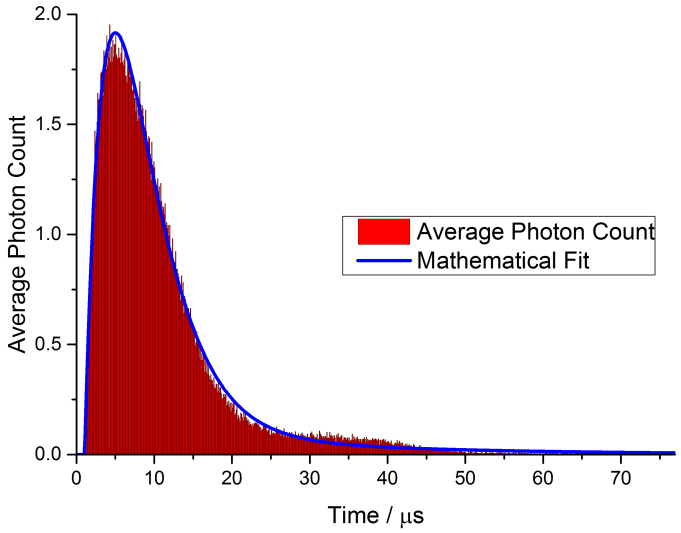

(b) Recorded CELIF Photon Counting Histogram

Fig. 5.7 Comparison of the numerical convolution of LIF and RD traces and recorded CELIF photon counting histogram.

equation 3.8 and the LIF signal was defined by

$$I^{\mathrm{LIF}}_{\mathrm{Fluorescence}} = A_1 e^{-\frac{t}{\tau_1}} + A_2 e^{-\frac{t}{\tau_2}}, \tag{5.2}$$

where $I^{\mathrm{LIF}}_{\mathrm{Fluorescence}}$ is the intensity of the fluorescence signal, A_1 and A_2 are relative amplitudes of each fluorescence pathway and τ_1 and τ_2 are the fluorescence lifetimes of each pathway. Using Wolfram Mathematica these equations were convoluted and

the resulting function was fitted to the recorded photon counting histogram as shown by the blue line in Fig. 5.7(b).

The mathematical convolution appears to be a good match for the shape of the photon counting histogram with no major deviations. However the fitted parameters produce a value of the τ of 3.89 µs which is significantly different from the measured value of 1.62 µs. On account of these discrepancies these results cannot be said to have fully characterised the CELIF signal.

5.3.3 Probing the Detection Limit

In order to examine the effectiveness of the optical system as well as the potential utility of the CELIF technique as the detection method for Photostop it was prudent to attempt to probe the detection limit of the CELIF system. This could be achieved by sequentially diluting the SO_2 molecular beam using Ar and measuring the recorded CELIF signal until it reached background levels. Initially the gas mixing system was filled with 150 mbar of SO_2, which was then topped off to 1.5 bar with Ar and this gas was left to mix in the system for 10 min with heating tape wrapped around the mixing gas lines to speed up the mixing. For each dilution the initial SO_2 mixture was diluted by a factor of 10 so that the number of molecules would reduce by an order of magnitude. Additionally averaged photon counting histograms were recorded at each dilution to ensure that the fluorescence signal could be distinguished from background.

As can be seen in Fig. 5.8, the initial measurement show a significant decrease in S^{CELIF} with each dilution. However this soon begins to level off after around 10^{-6} dilution. The reason for this appears to be that the SO_2 has been adsorbed onto the walls of the gas mixing and delivery system ultimately meaning that the measured dilutions were inaccurate. Unfortunately this ultimately meant that the detection limit could not directly be examined in this manner as the calculated dilution from the gas mixing is ultimately meaningless and despite repeated dilutions and evacuation of the gas line with a rotary pump the presence of SO_2 was still

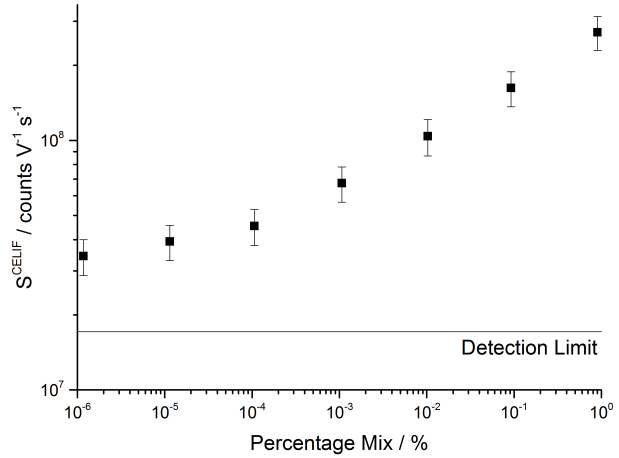

(a) Dilution Curve

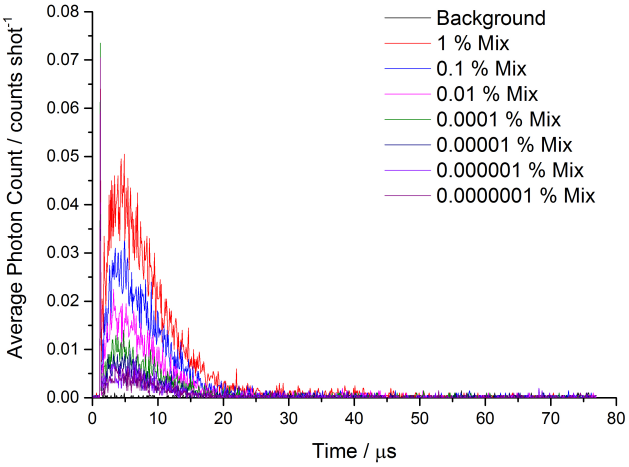

(b) Dilution Photon Counting Histograms

Fig. 5.8 Plot of S^{CELIF} for increasing dilution of SO_2 with Ar along with the measured photon counting histograms at each dilution.

evident and with little change in magnitude.

5.3.4 Comparison of CELIF, single-pass LIF and CRDS

Given that during this experiment CELIF, single-pass LIF and CRDS have been used to measure the absorption/fluorescence spectra of SO_2, it seems to prudent to make a direct comparison of these techniques.

It is consistently demonstrated by the spectra recorded and shown in Figs. 5.9, 5.10 and 5.11 that both single-pass LIF and CELIF have significantly better signal-to-noise ratios than CRDS. This is to be expected given the high sensitivity of both CELIF and LIF as well as the fact that CRDS requires two measurements, τ and

τ_0 thus propagating the uncertainties in both measurements, particularly when the measurements approach the limit of detection. As a result of this, in most cases the CRDS measurements could not definitively display the majority of the peaks shown by the other methods.

In comparing the spectra from the two different CELIF signals (photon counting and area integration) we can observe effects of the aforementioned region of crossover between the two regimes. Looking at Fig. 5.9 there appears to be little discernible difference between the two spectra, although the signal to noise ratio of the photon counting spectrum does appear to be improved. However, Fig. 5.10 shows significant differences between the two spectra with regards to the most intense peaks, which is further compounded in Fig. 5.11. This appears to be the result of under-counting of the photons in regions with high signal (as described in 5.3.1) and the reasons this becomes more prevalent for decreasing wavelength are twofold. First it has been previously shown that the peaks at lower wavelengths of this region have a more intense fluorescence [108]. Second, the reflectivity of the cavity mirror coating has its peak at 330 nm meaning that the transmittance of the mirrors is higher for these shorter wavelengths. This ultimately means that the intensity of the probe laser light is greater and hence there will be a stronger fluorescence signal. Although the CELIF process does compensate for changes in intensity by measuring the RD signal the issue here is the transition from a photon counting signal to a time integrated signal. If the transmittance of the mirrors or the fluorescence of the molecule increases too much the magnitude of the fluorescence signal may cross between these regimes thus resulting in under-counting of photons, hence the discrepancy shown in Figs. 5.11 and 5.10.

In terms of comparing the LIF and CELIF spectra it is difficult to distinguish major differences. There are of course some variations in relative peak heights between the two as these measurements were taken independently requiring alterations to be made to the chamber and nozzle, hence the SO_2 may not have been at the same temperature for each measurement, hence the different peak heights. In terms of the precision of the two techniques, from these results there is no significant difference

between them. If we examine Fig. 5.9, there do appear to be some smaller peaks in the photon counting CELIF signal in the region of 320.2 nm which are not clear in the single-pass LIF, which may indicate that there is an improvement in sensitivity with CELIF. However to confirm this, a deeper analysis would need to be undertaken such as performing a dilution measurement, which was unsuccessful in this experiment.

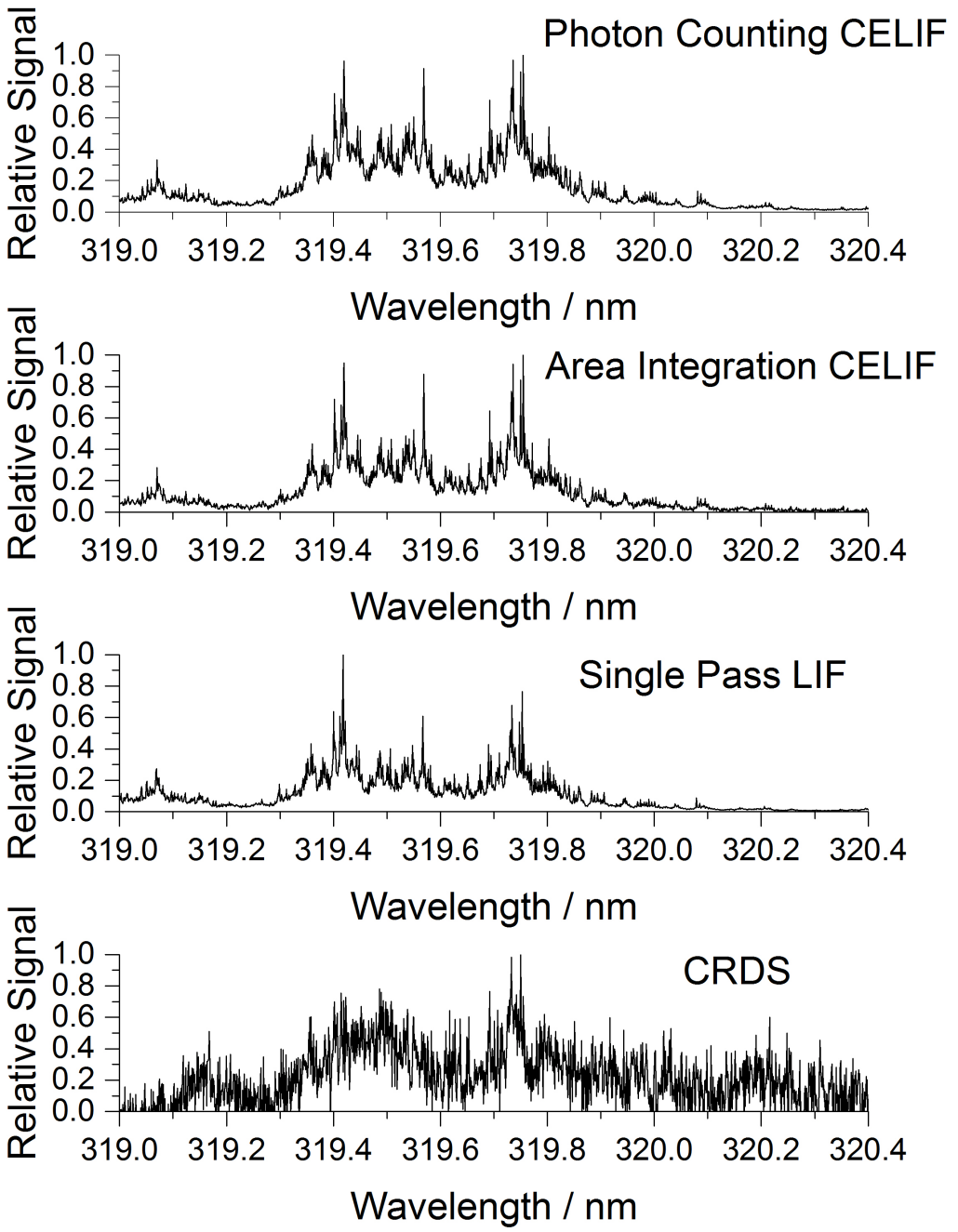

Fig. 5.9 SO_2 spectrum taken between 320.4 nm to 319 nm in steps of 1 pm with l0 laser shots per point using Photon Counting CELIF, Integral CELIF, Single Pass LIF and CRDS. This wavelength range corresponds to transitions from the $^1A_1$ ground state to the $^1B_1$ excited electronic state of the SO_2. It should be noted that the CELIF and CRDS measurements were taken at the same time and the LIF measurements at a later date.

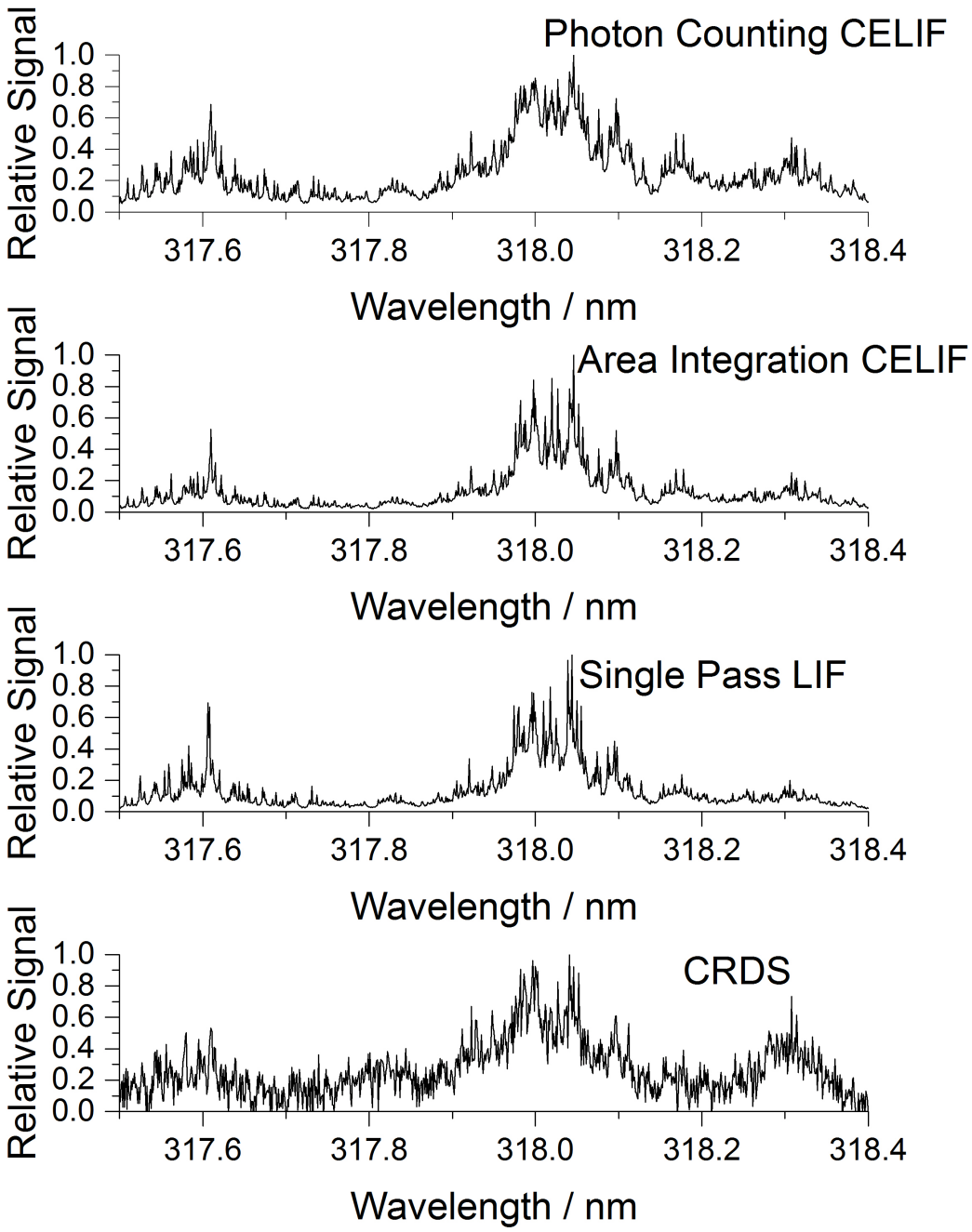

Fig. 5.10 SO_2 spectrum taken between 318.4 nm to 317.5 nm in steps of 1 pm with l0 laser shots per point using Photon Counting CELIF, Integral CELIF, Single Pass LIF and CRDS. This wavelength range corresponds to transitions from the $^1A_1$ ground state to the $^1B_1$ excited electronic state of the SO_2. It should be noted that the CELIF and CRDS measurements were taken at the same time and the LIF measurements at a later date.

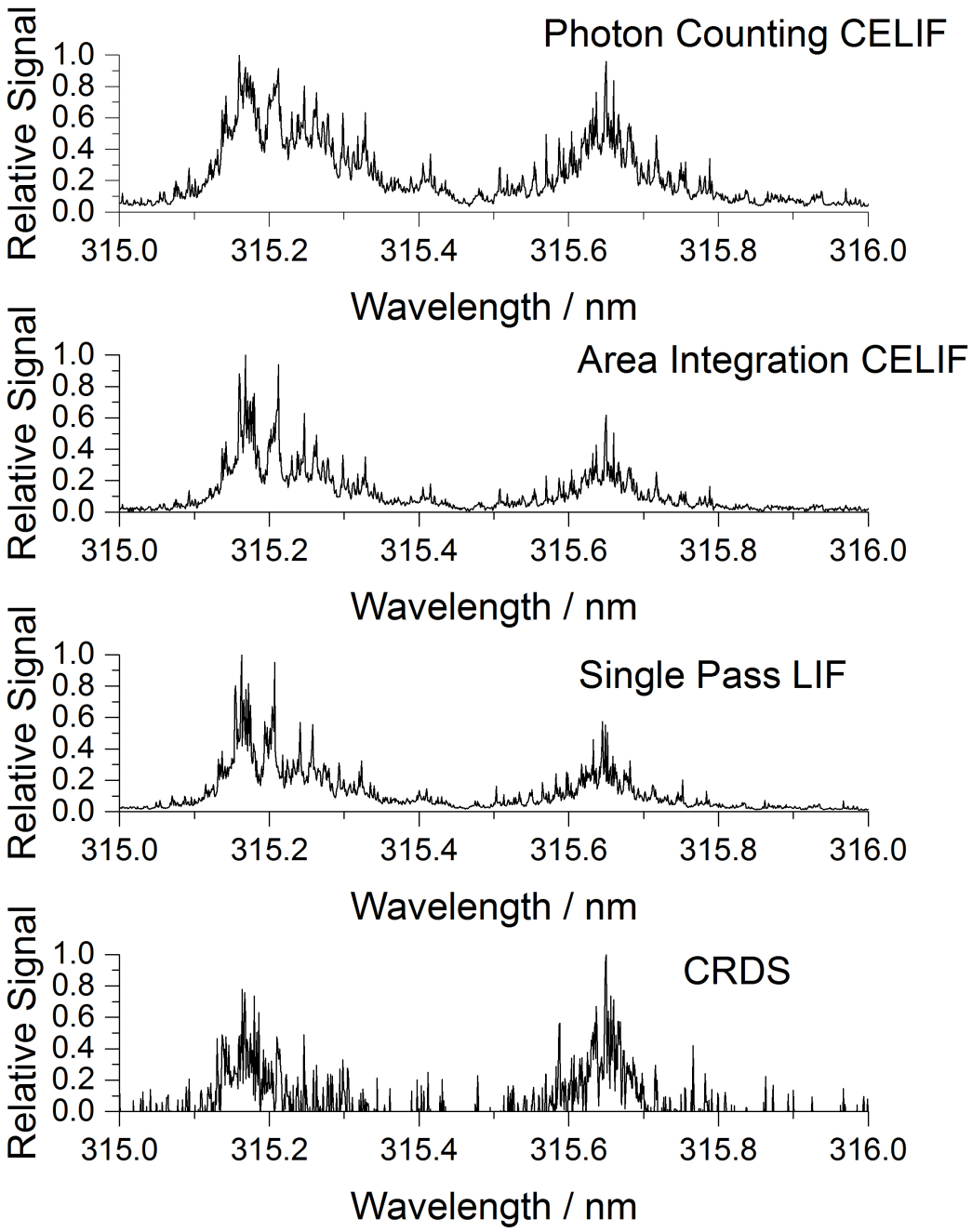

Fig. 5.11 SO_2 spectrum taken between 316 nm to 315 nm in steps of 1 pm with l0 laser shots per point using Photon Counting CELIF, Integral CELIF, Single Pass LIF and CRDS. This wavelength range corresponds to transitions from the $^1A_1$ ground state to the $^1B_1$ excited electronic state of the SO_2. It should be noted that the CELIF and CRDS measurements were taken at the same time and the LIF measurements at a later date.

5.4 Discussion

On the whole the investigation of the CELIF of SO_2 has produced highly mixed results. To some degree it has been shown that absolute number density measurements can be taken with CELIF from a calibration using CRDS. Additionally this calibration appears to have a significantly reduced error compared to directly calibrating single-pass LIF as described in [103]. Additionally this calibration is significantly more rapid and precise than the process required for single-pass LIF. However the effectiveness of this calibration is inhibited by the issue of the crossover between the area integration and photon counting regimes. The nature of the Photostop experiment will likely result in the number density (and thus the signal) decreasing over a large range, thus making it necessary to cross from one regime to another, making this an important issue. In principle this could be compensated for by either reducing the laser power to move further into the photon counting regime, or by increasing the laser power to move the signal into the time integration regime. However to perform this it would require on-the-fly adjustments, which may not be efficient for some circumstances thus it would be much more preferable to find a way to maintain the calibration over this region without such adjustments.

In terms of characterising the CELIF, ultimately the exact form and origin of the fluorescence signal could not be entirely described by these results. The fact that a simple convolution of the RD signal and single-pass fluorescence signal does not provide even a qualitative match to the recorded CELIF signal clearly indicates that a more detailed examination of the processes involved is required, in particular with reference to the excitation of multiple excited states and the effect of the quantum beats. Additionally, given the fact that the fitted mathematical convolution of the equations defining the RD and single-pass fluorescence traces do provide a good match, there may be a case to argue that the signal from particular fluorescence pathways are inhibited by the presence of the cavity, possibly as a result of not being modes of the cavity. Whatever the case may be, it is clear that further investigation will be required if this is to be fully explained.

Unfortunately due to the issue of SO_2 sticking to the walls of the gas line the detection limit of this system could not be effectively probed. This issue was not anticipated but could have been compensated for by applying a Teflon coating to the internal walls of the gas line.

Although some comparison can be made between the recorded CRDS, CELIF and single-pass LIF spectra there are many aspects which require more analysis. Notably, the relative sensitivities of the single-pass LIF and CELIF should be assessed more rigorously. Ideally this could be achieved by performing a dilution measurement using each technique, which could not be performed here for reasons that have been stated previously.

5.5 Conclusions and next steps

The use of CELIF with SO_2 has provided a number of useful insights into the technique which could prove invaluable for future study. Although the CELIF calibration for absolute number density measurements proved inaccurate for high number densities, this did serve to highlight the issue of under-counting of photons with this particular set up. The characterisation of the CELIF signal has proven to be inconclusive with regards to de-constructing the nature of the fluorescence from CELIF in this case. That said, this does potentially provide an interesting avenue for further investigation in the future. Given the promise shown by these measurements the next step was to apply this technique to the photostop experiment.

6. PHOTOSTOP CELIF MEASUREMENTS

6.1 Introduction

Although the CELIF measurements of SO_2 were only partially successful, it was decided to move forward and test the technique for the purpose of measuring the decay of molecules in the probe volume from the Photostop process. As the detection limit was unclear from the previous measurements it was uncertain if the technique would prove to have sufficient sensitivity for this experiment. Thus the initial stages of this experiment was focused on determining and improving upon the detection limit of the CELIF system and so it is only in the later stages that the full trap apparatus is introduced.

6.2 Experimental

The apparatus for this experiment remains largely unchanged from the SO_2 measurements, the only addition being the dissociation laser. The 213 nm dissociation laser is generated from the fifth harmonic of a Surelite Continuum Nd:YAG laser. The laser was equipped with a second and fourth harmonic doubling crystals to produce 266 nm light. Immediately after the exit of the laser this was combined with the fundamental (1064 nm) using a BBO crystal. The fifth harmonic was then separated from the other wavelengths using a set of specialised dichroic mirrors and prisms. For the initial measurements there was no internal structure in place except an extension from the flange, which held the optical elements required for detecting fluorescence signal (as was used in the SO_2 measurements); this however changed during the later stages as will be specified below. The molecular beam source was

once again a pulsed Parker General Valve driven by an IOTA ONE driver and the backing gas was pure H_2S unless otherwise specified below. To compensate for the slow acquisition rate of the digitiser card the outputs from the PMTs of the cavity and fluorescence detection were fed into a LeCroy Waverunner 610Zi (which shall henceforth be referred to as the fast scope), which in turn was connected to the main PC by an Ethernet cable for further signal processing and data acquisition.

6.3 Results

6.3.1 Rayleigh Scattering calibration of CELIF

As the production of SH/SD by necessity requires the dissociation of H_2S it was reasonable to assume that the number of molecules may not be sufficient to produce a definitive change in ring-down time. Thus it seemed prudent to first determine some form of calibration using Rayleigh scattering in a manner similar to the one used in [104] and using the same wavelength. More specifically, we need to determine the instrument calibration factor $\frac{2g}{T}$ as outlined by equation 3.11 and as was measured in the previous chapter. The principle of this is to measure the Rayleigh scattering CELIF signal for increasing pressures of N_2 and thus by measuring the pressure (and therefore the number density) the CELIF calibration factor can be determined. This is similar to the measurements taken in Chapter 4 and in fact the measurements taken there were repeated to supplement this calibration. An example of one of these measurements is given in Fig. 6.1.

In order for this calibration to be valid there must also be a consideration of the differences in the processes of Rayleigh scattering and fluorescence. If the fluorescence occurs faster than the expected rotation of the molecule (as it does in this case) the light will be emitted isotropically, whereas Rayleigh scattering is dependent on the polarisation of the excitation photons. This is because during Rayleigh scattering the absorbed photon acts as a perturbation on the electronic orbitals of the target molecule. In simple terms, the electric field of the absorbed photon causes the elec-

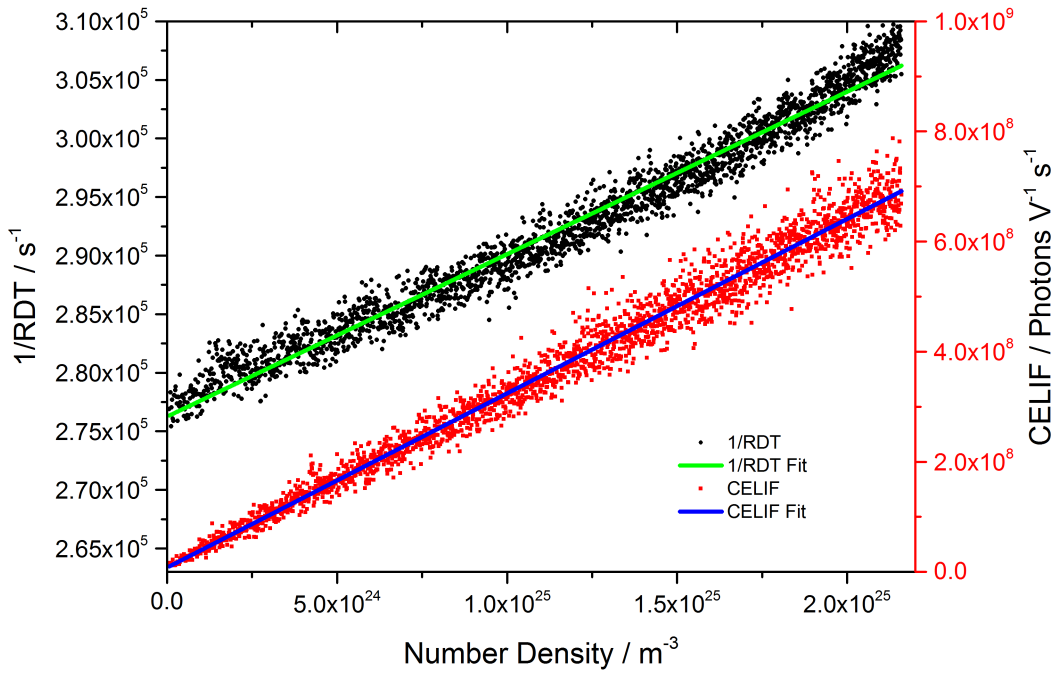

Fig. 6.1 Calibrated CELIF signal vs number density of N_2 along with CRDS measurements taken simultaneously. These measurements were taken using a probe laser wavelength of 323.17 nm.

tronic orbital of the molecule to oscillate in the direction of the polarisation of the photon (i.e. the orientation of the electric field). This oscillation gives rise to the production of photons perpendicular to this direction as a result of the changing electric field of the molecular orbitals. The ultimate result of this is the production of photons in a $\sin^2$ distribution perpendicular the orientation of the polarisation of the absorbed photon.

To examine this effect a combination of a quarter-wave plate and linear polariser was added to the probe laser beam path. The purpose of this was to first make the initially linearly polarised light circularly polarised with the waveplate and then isolate a selected linear polarisation using the linear polariser. The linear polariser was mounted on a rotating mount so that a range of linear polarisations could be isolated. This combination does result in the loss of probe laser intensity but as the CELIF measurements are calibrated against probe laser intensity, this is not an issue for these measurements. The different CELIF calibration factors found for varying polarisation angles are shown in Fig. 6.2.

From these results, the CELIF calibration factor corresponding to the detection of

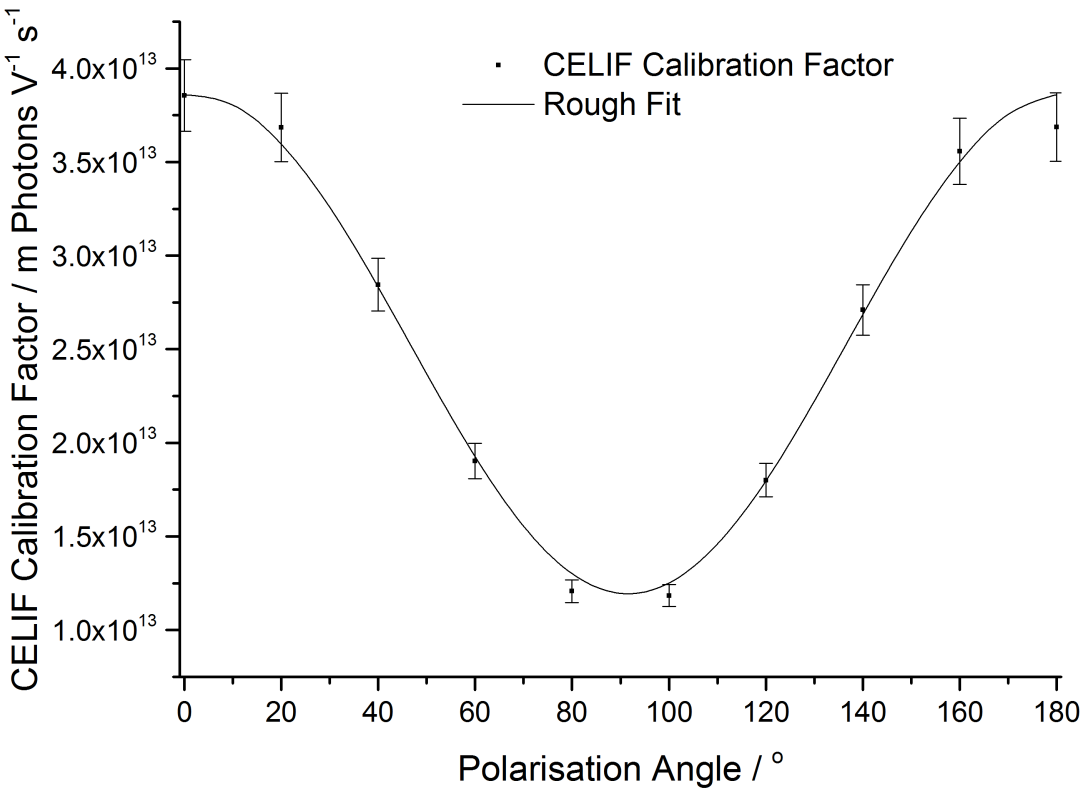

Fig. 6.2 Angular dependence of Rayleigh scattering CELIF calibration factor. Polarisation angle in this case is measured from an initial vertical orientation (i.e. 0° is vertically polarised light).

fluorescence signal can be determined on consideration of the angles of the detection optics. For instance, if the detection optics were perpendicular to the orientation of the laser propagation in the plane of the polarisation then the amount of light detected would be reduced as the scattered light is predominantly produced perpendicular to this. Thus in order to obtain the correct calibration factor the angle of polarisation must be such that the intensity of the distribution from Rayleigh scattering is equivalent to the distribution of fluorescence. This is known as the 'magic angle' and has a value of 54.7°. The effect of this is that a measurement at this angle is independent of the angular distribution of the outgoing photons from either Rayleigh scattering or fluorescence. This assumes that the angular distribution can be described via $I(\theta) = I_0(1 - \beta P_2(\cos\theta))$, where $P_2(x) = \frac{3}{2}x^2 - \frac{1}{2}$ is the 2nd order Legendre polynomial. In our case, the detection optics are not aligned perpendicularly to the laser axis as shown in section 3.7. Given this, the 'magic angle' for our system is not at 54.7° but instead at 38.7° which compensates for the change in orientation. From a measurement at this angle a CELIF calibration factor

Table 6.1 Measured N_2 Rayleigh scattering cross-section and photon counting CELIF calibration factor taken at the magic angle along with corresponding uncertainty (this corresponds to the 1σ standard deviation).

	Value	% Uncertainty
CELIF calibration $\left(\frac{2g}{T}\right)$	$3.9 \pm 0.2 \times 10^{13}\,\mathrm{m\,counts\,V^{-1}\,s^{-1}}$	4.7%
σ_{N_2}	$4.9 \pm 0.2 \times 10^{-26}\,\mathrm{cm^2}$	4.6%

was obtained as shown in Table 6.1.

Given the similarity between this experiment and the previous measurements of the Rayleigh scattering cross-section of N_2, it was prudent to repeat those measurements at our target wavelength to see if any improvements could be made. Additionally, after taking the initial set of measurements shown in Fig 6.2 the detection optics were optimised in order to maximise the calibration factor and thus the sensitivity of the apparatus. The result of this is also shown in Table 6.1 and indicates something of an improvement in terms of uncertainty compared to the previous measurements.

6.3.2 CELIF measurements of SH and SD

Now armed with a CELIF calibration, the initial step was to attempt to measure fluorescence signal from our target molecule. Initially, the chosen target was to be SD produced by the photodissociation of D_2S as this has a significantly higher fluorescence quantum yield than the more readily available SH/H_2S. However, due to the difficulty in procurement, the D_2S needed to be synthesised from the reaction of deuterated phosphoric acid and iron (II) sulphide[1]:

$$2D_3PO_4 + 3FeS \rightarrow 3D_2S + Fe_3(PO_4)_2. \tag{6.1}$$

This process was performed in single batches and with relatively small yields, meaning that the D_2S would need to be mixed with noble gases in order to provide enough backing pressure for a molecular beam. However when we attempted to make measurements of the SD molecules using CRDS/CELIF, we were unable to distinguish any unique signal from the SD molecules. As such we switched to using H_2S as an

[1] More details on this process are given in [109].

alternative as, although the fluorescence quantum yield is much smaller, the ready availability meant that we could use pure H_2S molecular beams. Using a pure H_2S molecular beam, CRDS and CELIF spectra of SH were obtained in the region of interest for the ground state transition as shown in Fig. 6.3. These spectra were produced with a 5 ns delay between the 213 nm dissociation laser and the probe laser.

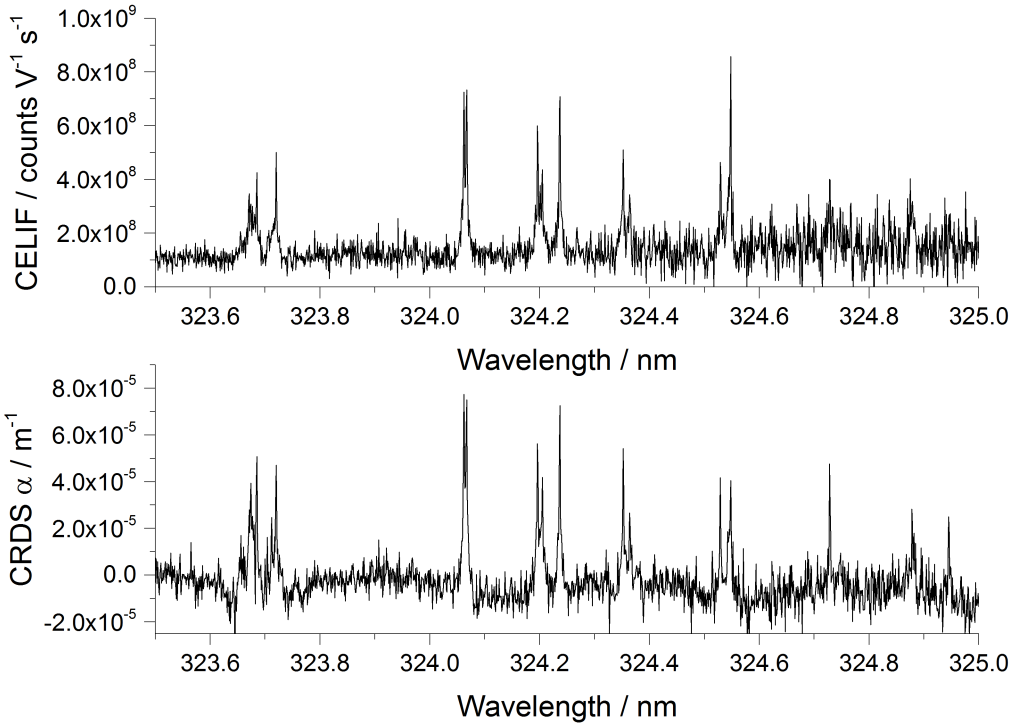

Fig. 6.3 Spectrum of calibrated CELIF and CRDS signal of SH between 325 nm and 323.5 nm, this corresponds to the $A^2\Sigma^+ \leftarrow X^2\Pi_{3/2}$ transition of SH. It should be noted that the CELIF and CRDS measurements were take simultaneously.

It is apparent in Fig. 6.3 that there is significant noise in the CELIF signal from SH, so much so that the signal to noise is comparable to the CRDS measurements. Upon deconstruction of the signal it appeared that this was most likely due to a combination of the contribution of Rayleigh scattering of the H_2S molecules, which was significant and occurred at all wavelengths, and stray light from the dissociation laser. As we believed that this effect would be reduced at longer delays as the H_2S would leave the probe volume, we proceeded to make measurements of the photostop decay from increasing delays between the dissociation and probe lasers using a pure H_2S molecular beam and measuring the decrease in signal with both CRDS and CELIF. The results from this are shown in Fig. 6.4.

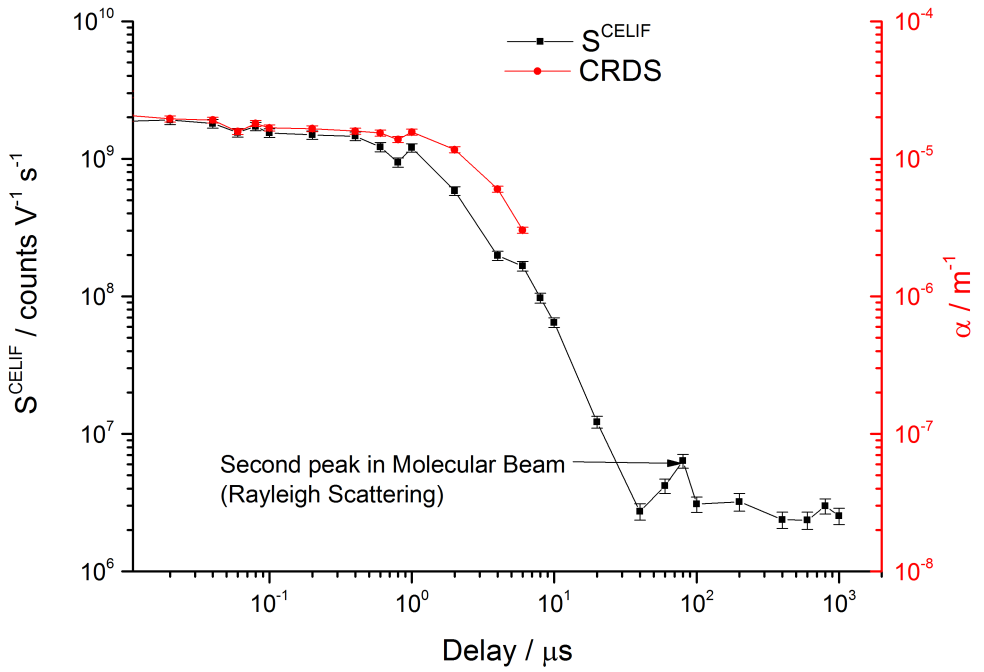

Fig. 6.4 Decay in absorption coefficient (from CRDS) and calibrated CELIF signal for increasing delays between the dissociation and probe lasers for the production of SH from H_2S photodissociation. It should be noted that the CELIF and CRDS measurements were take simultaneously.

Fig. 6.4 clearly shows that using CELIF we have been able to measure a decay in signal of around three orders of magnitude before the signal begins to level off at around 30 µs, indicating that the signal has been lost into the background noise. As this is clearly not at the required sensitivity to measure the predicted trapping of photostopped molecules[2] we decided to de-construct the measured fluorescence signal in terms of the individual contributing factors to the molecular beam, i.e. the dissociation laser, the probe laser and the molecular beam. The result of this is shown in Fig. 6.5.

From 6.5, it is self evident that, of the two lasers, the primary contributor to the measured signal at the fluorescence PMT is the dissociation laser. Initially this could be considered to be the result of scattered light inside the chamber, however the signal remains for significantly longer than one would expect for scattered light and it is also exacerbated by the presence of the molecular beam, indicating that there is some form of fluorescence occurring. Upon examination of the literature, we found

[2] This prediction is based on the results from the previous simulations from the group presented in Fig. 2.5.

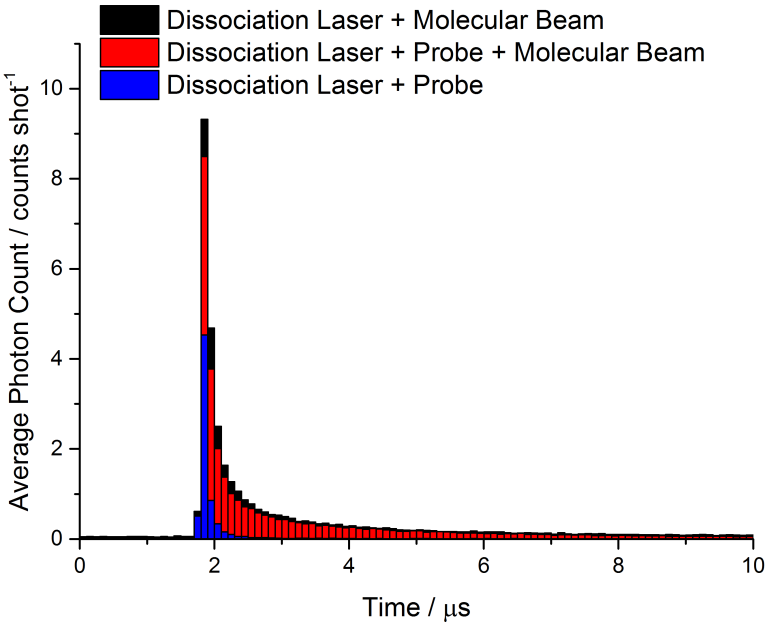

Fig. 6.5 Photon counting histograms showing the breakdown of CELIF signal from probe and dissociation lasers

no such transition for this to occur in H_2S or SH using the 213 nm dissociation laser, but there is such an absorption for SO_2. Evidently some SO_2 may have remained in the gas mixing system from the previous CELIF measurements in spite of the extensive cleaning and evacuation of the chamber.

Another matter for consideration is the ultimate detection limit of CELIF. In principle, CELIF is, by necessity, background free as the probe laser is entirely trapped in the cavity, thus eliminating stray light. To confirm this we measured the CELIF fluorescence signal with and without a molecular beam present in the cavity which is shown in Fig. 6.6. It is evident from this that even without the presence of the molecular beam, there is still a significant amount of background signal which continues during the the entirety of the ring-down decay.

6.3.3 Cooling Effects

As the focus of this experimental design is the cryostat to provide a form of differential pumping, we needed to examine the operation of the cryostat as well as the effects the cryostat may have on the CELIF measurements. For these measurements the internal structure of the chamber was fully constructed with the magnetic trap

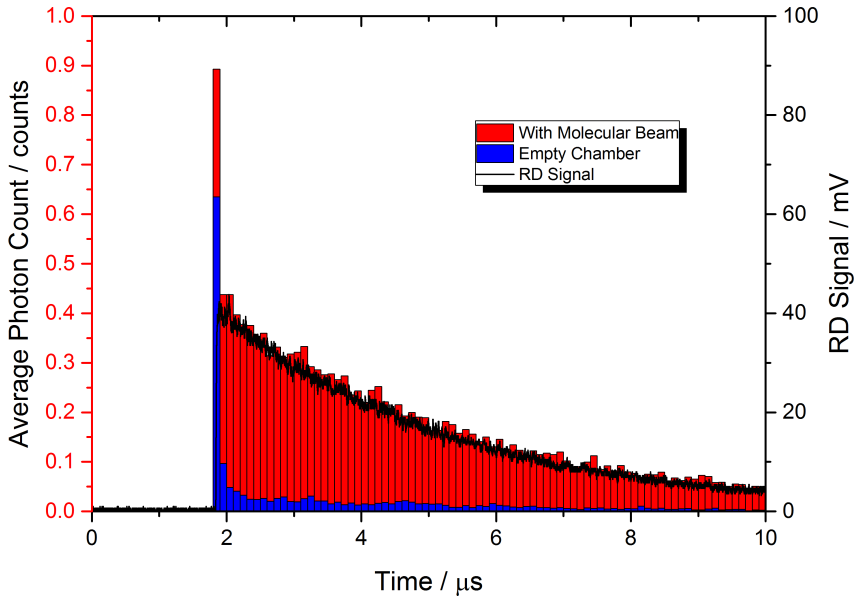

Fig. 6.6 Background signal from the probe laser interacting with the cavity.

secured onto the head of the inner stage of the cryostat. To do this the cryostat was activated and the temperature was measured (using a K type thermocouple mounted on the base of the outer stage) as well as the background CELIF signal. The results from this are shown in Fig. 6.7.

It is clear from this that as the temperature reduces there is a significant increase in the background CELIF signal. Coupled with this is also a reduction in the ring-down time indicating that there are additional cavity losses on each round trip. This suggests that as the internal structure contracts, the gap that the laser is aligned through moves relative to the position of the laser. This means that the cavity becomes partially intersected by the internal surfaces during the cooling process resulting in increased cavity losses (hence a reduced ring-down time) and increased stray light. An additional feature to notice is the discontinuity in the temperature decrease at around 50 min. This is an artefact of the functioning of the cryostat. To make the pumping surfaces cold compressed helium is pumped through internal pipes inside them. The helium is compressed by an external compressor unit which is water cooled and possesses a temperature sensor to prevent overheating. In our case the cooling water flow through the compressor was maximised but the internal sensors of the cryostat detected the compressor was overheating and so stopped the

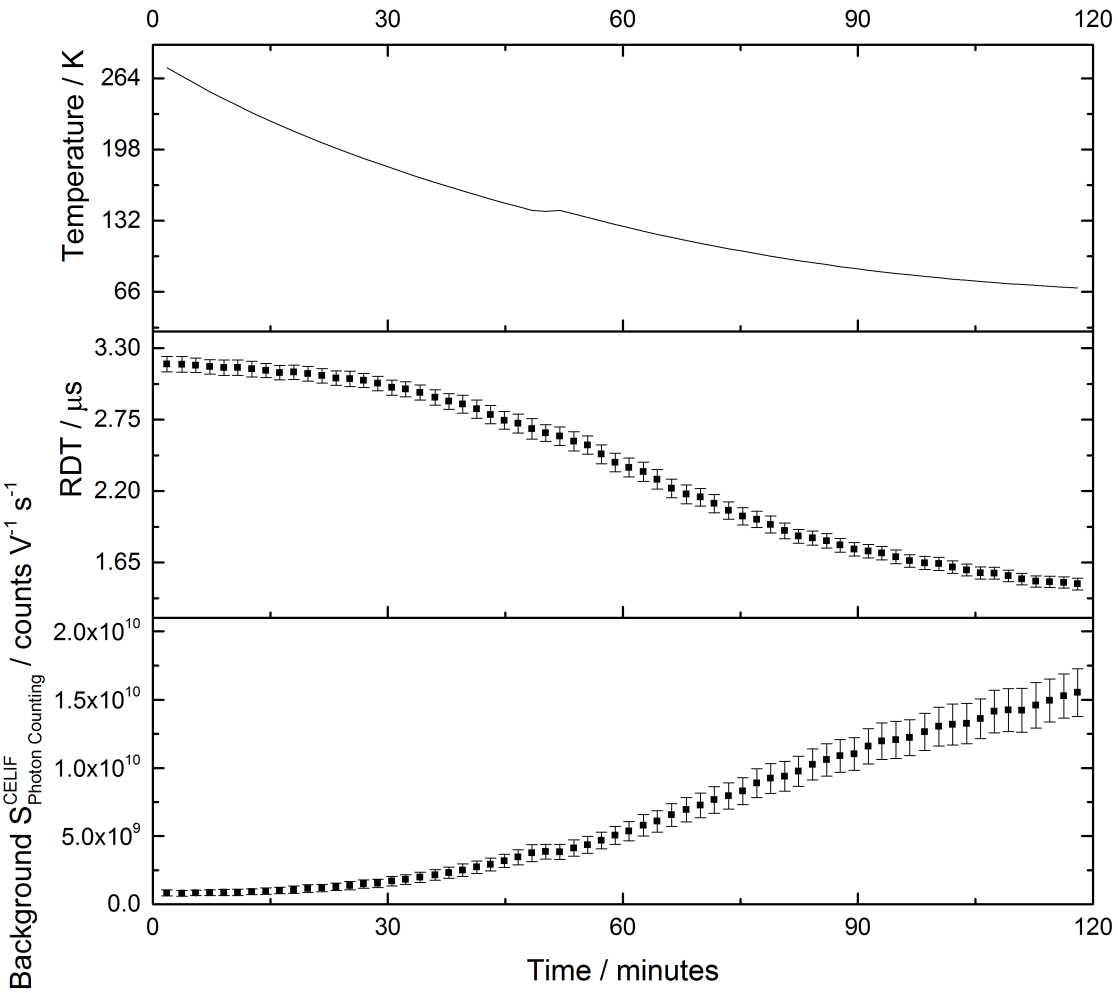

Fig. 6.7 Measured cooling rate of the cryostat using a thermocouple mounted on the base of the outer stage along with the measured background CELIF signal and ring-down time. Each measurement of CELIF signal and ring-down time is an averaged measurement of 1000 laser shots taken at each time point.

pump. As a result of the pump stopping the temperature did not decrease any further and this gave rise to the discontinuity shown.

6.4 Discussion

The initial N_2 Rayleigh scattering measurements have shown some promise with regards to the precision of the absolute number density calibration of the CELIF measurements. Compared to previous work with this method [104], there is an improvement in terms of the precision of both the calibration factor as well as σ_{N_2}. However the limiting factor for projecting this calibration onto the measurements of another fluorescing species is the knowledge of the absorption cross-section/fluorescence

quantum yield of the target molecule. In the case of the Photostop measurements this would be SH/SD, both of which are not widely known and difficult to measure directly. Additionally, a major limiting factor on these measurements remains the uncertainty on the value of σ_{N_2}. When comparing the results given by these measurements and the extrapolated value of 4.12×10^{-26} cm^2 from [104], we can see that very similar values have been found although they rely outside of each other's error. That said, given that the value used in [104] was extrapolated from literature data, this small discrepancy is unsurprising and does not necessarily bring the accuracy of these measurements into question. Although the uncertainty was improved when compared to the prior work in this project, the lack of reproducibility in the measurements is ultimately a result of the range of uncontrolled variables in the experiment and so more stringent controls may be required to reduce this uncertainty further. That being said, when comparing the direct calibration measurements, there is an improvement in precision when compared to the CRDS calibration performed with the SO_2 CELIF measurements. However this increased precision may also be the result the larger number of measurements taken to reach the said calibration factor with the Rayleigh scattering measurements.

The poor performance of CELIF when applied to SD/SH was unexpected, but in hindsight there is good evidence as to why this is. First and foremost is the issue with background signal from the dissociation laser. Given that the probe laser is coupled into a cavity and therefore loses a significant portion of its intensity, it is unsurprising that scattered light from the significantly more powerful dissociation laser would be problematic. Although attempts were made to minimise this with bandpass filters on the detection apparatus to filter out the dissociation wavelength, ultimately, the intensity of this laser was too great to fully overcome the issue in this manner. Another issue that arose from the dissociation laser is the fluorescence of the laser windows from interaction with the dissociation laser. This ultimately lead to a certain degree of background signal that could not be effectively removed using filters and thus provides an additional limiting factor to the experiment. To combat this, plans were made to have the entrance windows to the chamber perpendicular to

the desired propagation of the dissociation laser (see Fig. 6.8). Ultimately however these plans were not implemented as the other difficulties that arose essentially negated the utility of CELIF in this case, but these ideas may be applicable in the future.

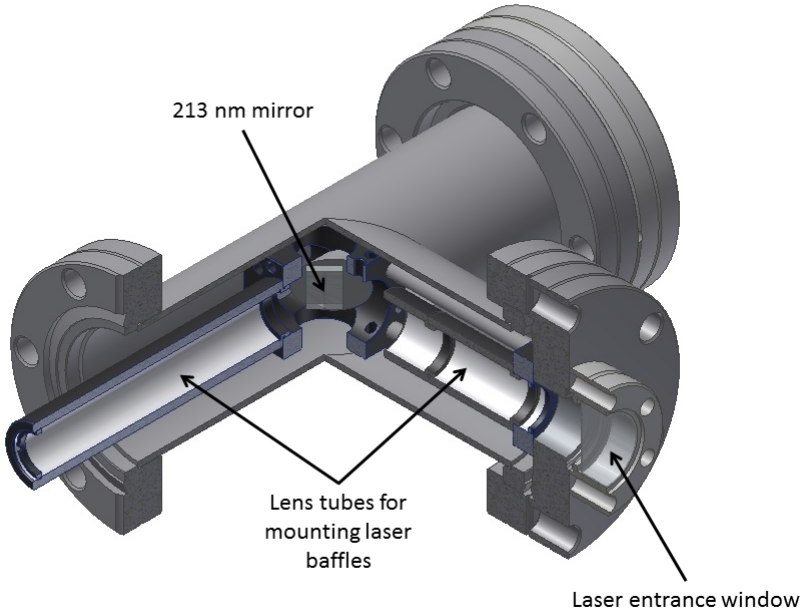

Fig. 6.8 Cut-away schematic of planned system to reduce fluorescence signal from dissociation laser windows.

The fluorescence signal, presumed to be from leftover SO_2 in the pipes, was entirely unexpected as great efforts were taken to clean the gas mixing system after those experiments. In fact the residual gas analyser, which was positioned along the path of the molecular beam, could not detect the SO_2 present. This might lead to the conclusion that the signal was not due to SO_2, however successive flushes of the gas line with pure Ar produced a visible decrease in the signal from the dissociation laser interacting with the molecular beam, suggesting that it must be a contaminant. Ultimately, the only method that seemed to remove the SO_2 entirely was to dismantle the gas mixing system and coat its inner walls with PTFE (DuPont, PTFE dispersion N-3011). This involved heating the components to about 400 °C, which ultimately lead to a much cleaner system as a whole.

The further analysis of the background levels of the CELIF measurements has ul-

timately lead to a far better appreciation of the limiting factors of the technique. Although the CELIF method should be background free, a significant level of background photon counting signal was observed along the full decay of the ring-down signal. The justification for the background free moniker is that if the laser light is fully coupled into the cavity, it can only exist in cavity modes and therefore there should be minimal stray light. In practice, the laser beam is often not a perfect Gaussian shape, so not all of the light from the probe laser would be coupled into the cavity, which leads to a small amount of scattered light at the beginning of the ring-down decay. The additional photons along the full temporal length of the decay cannot be due to this as this would mean scattering over multiple surfaces for a significant pathlength. It is most likely that these photons are in fact a result of the florescence of the cavity mirror substrate. The justification for this is thus, for each round trip in the cavity the photons will interact with the mirror surface. As the probe laser in this case is in the UV range of the spectrum, it is more likely that light can be absorbed by the mirror substrate and thus fluoresce giving rise to a low-level fluorescence signal as long as light remains in the cavity. This effect ultimately determines the detection limit of the CELIF method as fluorescence signals weaker than this background will be difficult to distinguish. However this may only be a limiting factor at this wavelength, as for lower energy photons, the likelihood of the mirrors fluorescing reduces, thus meaning that the background level will be lower.

The cooling fault with cryostat is somewhat problematic but not crippling for the experiment. The main effect of this discontinuity in the temperature drop that was shown is that the cooling process took longer as the compressor recovered. This may however present an issue for future measurements with the cryostat in operation as, when the experiment is in progress if the cryostat stops as it did in this case it may produce an influx of gas into the trap volume as gas trapped on the surfaces starts to desorb. That said, this shut down is less likely to occur when the cryostat has fully cooled down as the heat load at these low temperatures is relatively minimal and so should not cause the cryostat to overheat. Another factor to consider in

the cryostat measurements is the method of measurement method itself. In our case we used a K-type thermocouple to measure the temperature on account of the ready availability of them. In practice the measurements made with a K-type thermocouple are normally only accurate to around 70 K so measurements below this temperature may be unreliable. However in our case the exact temperature of the cryostat is not vital to the operation of the experiment, as long as the background gas is effectively pumped by the chamber surfaces. In practice we are more concerned with the trend in the temperature measurements so when the measured temperature stops dropping (with the cryostat in operation) we can assume that the pump has reached the lowest temperature it can. In the event more accurate temperature measurements are needed, these could be achieved in a similar manner using a calibrated resistor mounted on the outer stage.

The effect of applying the cryostat is a significant concern for any future efforts to reincorporate CELIF into this experiment. The cooling is clearly causing a significant contraction of the inner structure which results in movement of the access points for the lasers as well as the positions of the magnets. This results in light on the edges of the cavity scattering off surfaces of the magnets and other components. Consequently, the RDT decreases, as more light is lost with each round trip, and the scattered light increases the level of background signal. On account of this it may be possible to compensate for this effect by measuring the degree by which the structures shrink and adjusting the cavity alignment appropriately. However exactly how this can be achieved is difficult to visualise as there is little leeway in how the cavity is aligned through the trap. To construct the cavity, the probe laser needs to be aligned through the cavity first and then the cavity mirrors are aligned along the path of the probe laser. As the cavity mirrors form part of the vacuum seal this needs to be performed before evacuating the chamber, so readjusting the alignment of the probe laser with the chamber evacuated is difficult as any significant adjustment is likely to destabilise the cavity. Further, given the small scale of the trap itself, the initial construction and alignment of the cavity with the internal structure can become problematic. In fact, during construction we had a significant

issue with this due to a 5′ wedge on the rear surface of the mirror. The main purpose of this wedge is to reduce the possibility of light exiting the mirror becoming trapped by the rear surface and creating an interference pattern. In our case the wedge shifted the alignment of the beam through our cavity sufficiently that some of the cavity modes scattered off of the surfaces of the trap and outer stage, and caused a noticeable reduction in RDT. At present the only solution to this conundrum that presents itself is for the cavity mirrors to be mounted and aligned on the outer stage of the cryostat and the laser to be aligned into them. This would allow for the cavity to remain optimised as the cryopump cooled, as well as providing a means to reduce scattering of light from surfaces. However as it would be impractical to use a cryostat with an outer shield 1 m long, this would reduce the ring-down time of the cavity and thus likely reduce sensitivity of the apparatus.

6.5 Conclusions and next steps

It was evident from these results that the application of CELIF to Photostop is fraught with difficulties at this stage. The predominant issue, the background noise from the dissociation laser, is unfortunately something that cannot be completely eliminated due to the nature of the experiment. Additionally the background signal from the isolated CELIF process ultimately means that there is a defined detection limit to the method which is dependent on the quality of the experimental setup. Further, sensitivity of the cavity measurements to disturbance means that further accommodation needs to be made to utilise this technique with the cryostat in operation. That being said, the Rayleigh scattering calibration has shown some degree of promise with potential for precise absolute number density measurements as there has been some improvement compared to previous measurements. With all of this taken into account, it was clear that the measurement of trapped SH/SD molecules would not be easily achieved using CELIF and thus we elected to move on to apply REMPI to this task.

Part III

RESONANCE ENHANCED MULTI-PHOTON IONISATION

7. TESTING REMPI APPARATUS

7.1 Introduction

On account of the significant issues that arose from the use of CELIF, we opted to utilise the REMPI technique instead. The incorporation of REMPI was considered during the initial design as outlined in 3.8.2 so alterations to the apparatus were minimal. Although this technique does not give absolute number density measurements, there is significant potential for improved sensitivity as there is reduced influence of scattered light and the potential for mass-resolution to isolate the target molecule which would reduce background noise. Thus after reconstruction of the experiment to facilitate this technique the apparatus needed to be tested and optimised, the results of this process being shown here.

7.2 Experimental

During the process of implementing the REMPI apparatus there were some alterations made to the original design of the trap as shown in Fig 7.1. Although the primary structure remained largely the same, the shown alterations were required in order to ensure that the individual elements could be held in place and electrically isolated from each other. Initially the insulators shown were planned to be made from boron nitride, which is a ceramic material that is electrically insulating while being thermally conducting. However due to the mechanical softness of the boron nitride there were significant issues during construction as the magnets, while repelling each other, would wear away at the material thus causing the electrodes to short out; this was a particular issue with the top magnet and the extraction

tube due to their closeness. With the bottom magnet the shorting issue could be attended to using Kapton tape to insulate it, but for the top section this proved difficult due to the tightness of the structure, thus the top insulator was replaced by an identical piece made from Macor, which has a reduced thermal conductivity but is mechanically more stable.

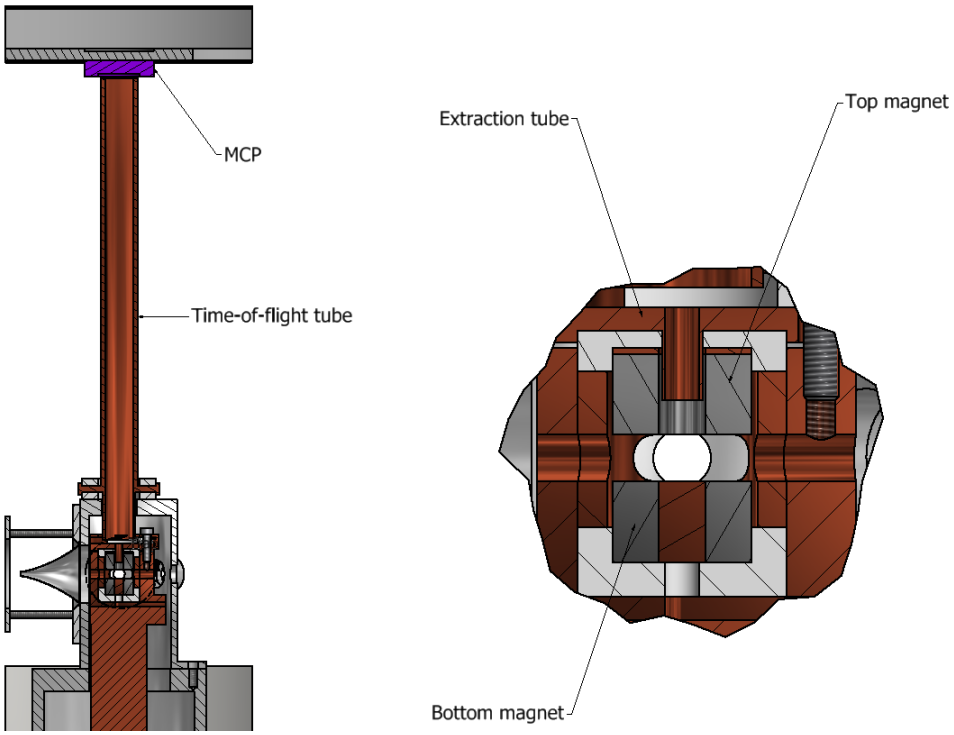

Fig. 7.1 Schematic of altered trap housing for use with REMPI.

The REMPI probe laser beam was generated using the frequency doubled Sirah dye laser with Coumarin 503 dye which is pumped by the third harmonic of a Nd:YAG laser with a 10 Hz repetition rate. The doubled light from this was optimised in the region of $250 - 260$ nm and aligned into the chamber using a set of prisms with a 500 mm focal length UV-grade fused-silica lens in front of the entry window to focus the laser into the centre of the magnetic trap.

Additionally, to aid in the characterisation of the molecular beam, a specialist Fast-Ionisation gauge (FIG) was added to the structure in the spherical square (as previously described in Section 3.8.2), which shall henceforth be referred to as the FIG chamber (see Fig. 7.2). The operation mechanism is outlined in section 3.8.2, but the practical upshot is that it allows for rapid measurement of pressure changes.

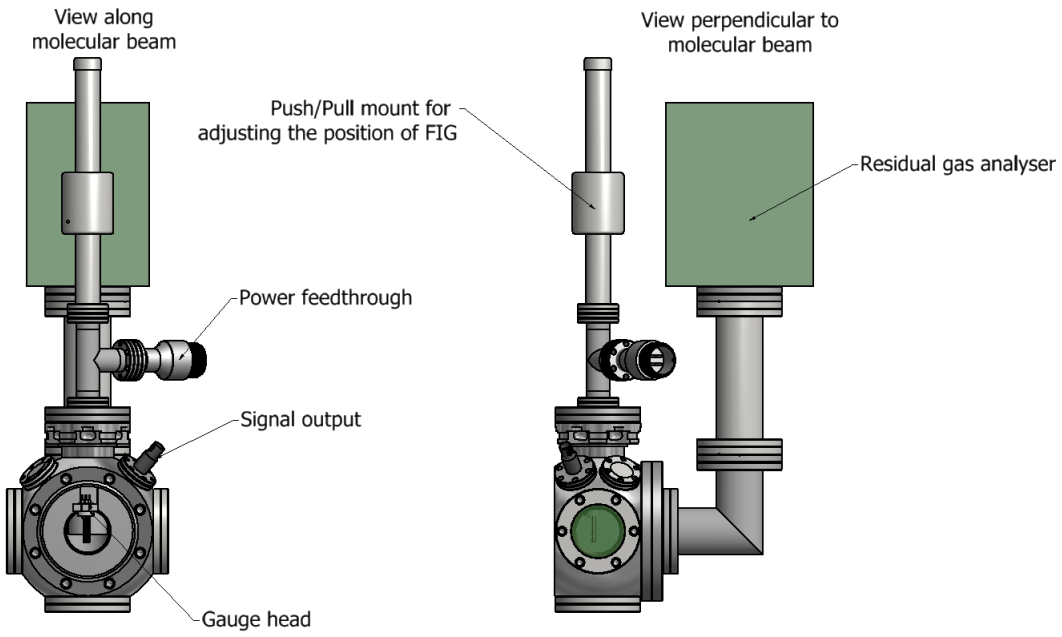

Fig. 7.2 Schematic of specialised mount/chamber for fast-ionisation gauge and residual gas analyser.

This was positioned along the molecular beam axis and was tested along with the REMPI detection apparatus to determine its utility in the larger photostop experiment.

For these initial tests of the REMPI apparatus we decided to use a $2+1$ ionisation scheme via the Xe $5p^5 6p$, $J = 2$ state with a 256.02 nm excitation wavelength. The reasons for this are threefold: first the wavelength required for the excitation itself is in a similar region to the one required for the detection of SH; second, the multiple isotopes of the species allows for the mass resolution of the apparatus to be examined; and finally, we had a ready supply of Xe available as it can be used for gas mixing to alter molecular beam speeds.

The REMPI signal defined here was measured from the output of the MCP which was recorded by the fast oscilloscope and then transmitted to the primary control computer. This signal was then processed to remove a baseline by averaging the MCP signal from before the probe laser fires and subtracting this from the entire trace. The portion of the TOF signal containing the Xe masses was then isolated from the full trace. The magnitude of this signal was measured using two separate methods; first by taking a numerical integral of the trace in the Xe mass region

and the second by measuring the ion count in the region, which also entailed the generating ion counting histograms (using the same numerical method for photon counting outlined in 5.2).

7.3 Results

As outlined previously the REMPI apparatus has been designed to operate in two distinct modes: the signal maximising or "Hoover" mode, which sucks up ions from inside the trap at the expense of mass resolution, and the mass resolving mode, which is akin to more traditional time-of-flight mass spectrometry, but with supposedly reduced signal. As such we will examine each of these methods in turn.

7.3.1 Characterisation of Ion detection

In order to properly understand the operation of the ion detection methods we initially opted to characterise the detection operation of the MCP for detecting individual ions. This is so that future ion detection measurements will have some foundation in regards to distinguishing the nature of signal from individual ions. To perform this initial characterisation we simply turned the voltage on the MCP up to the maximum (at the time $-1500\,\mathrm{V}$) and turned on the combination ion gauge used for measuring the chamber pressure. As outlined in Section 3.8.2, the operation of the ion gauge produces a steady flow of electrons, which ionise gas molecules. These ions were attracted to the strong negative potential on the front of the MCP and produced a continuous steady stream of ions for the MCP to detect. To measure the signal the fast scope was connected to the MCP and set to be triggered by this signal. This meant that the scope would trigger for each ion arrival and so from this the properties of the single ion signal could be found as shown in Fig. 7.3.

A number of things can be learned from these results. First, from the peak height distribution we can see that the ion peaks have a sharp initial rise in height followed by a more gradual decay, with no peaks seen with a magnitude below approx $4.8\,\mathrm{mV}$.

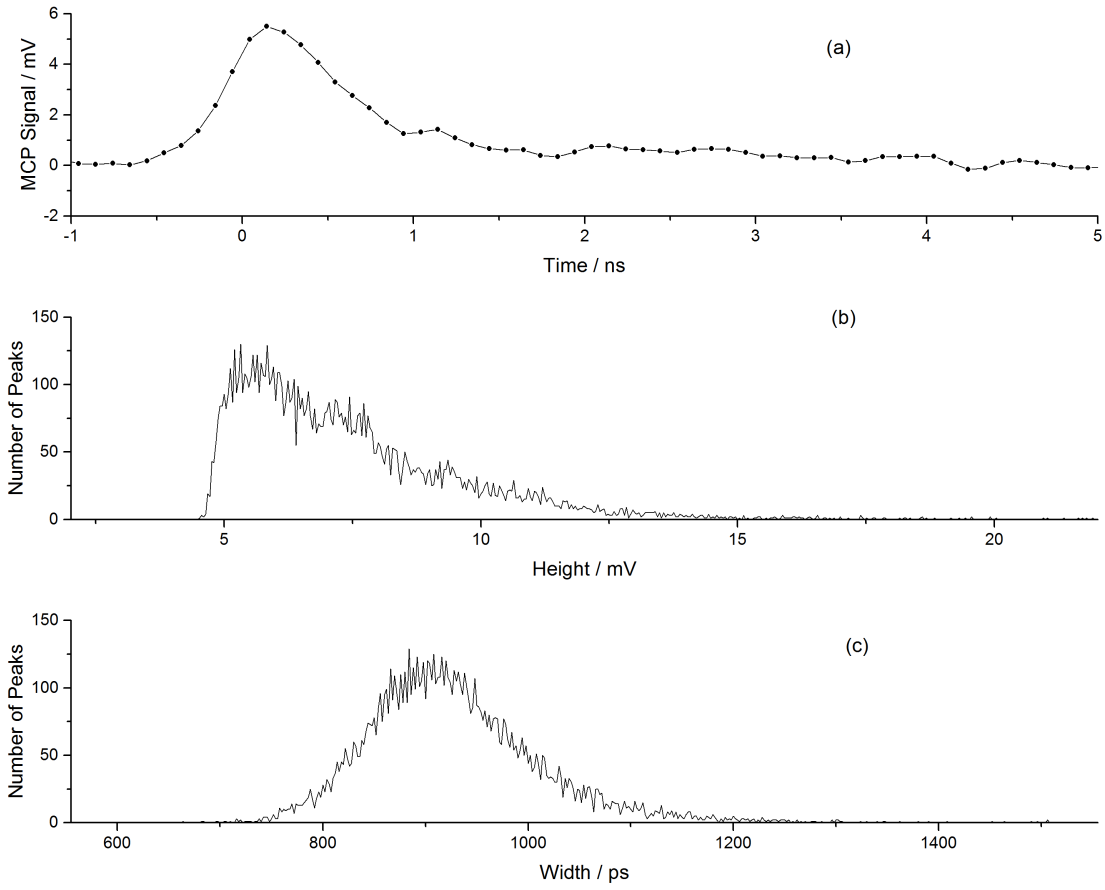

Fig. 7.3 Characterisation of single ion signals showing (a) a single ion peak, (b) the distribution of peak heights over 5000 single ion measurements and (c) the distribution of peak widths over 5000 single ion measurements. For all of these measurements the trigger level on the scope was set to 3.5 mV and the statistical distributions were accumulated using the onboard software of the oscilloscope.

From this, we can say that 3.5 mV will serve as a good threshold value to distinguish signal from background as it remains significantly above the baseline and all of the observed ion peaks are noticeably larger than this. The peak width distribution indicates that on average the detected ion peaks will have a width of approximately 900 ps. This is useful information when it comes to considering the sample rate of the data acquisition for the REMPI measurements as (in this case) if the acquisition rate is above 1 ns per sample it is possible that some ions could be missed in the ion counting regime.

7.3.2 Optimising the mass-resolving mode

As previously mentioned, during the construction process there were significant issues with the extraction tube shorting against the top magnet due mechanical failures of the boron nitride insulators. On account of this we initially tested the apparatus to see if the experiment could effectively operate without these components (i.e. with them both permanently grounded). To examine this, REMPI signal from Xe was compared for increasing voltages on the bottom magnet as shown in Fig 7.4. It should be noted that the voltages used here differ from those specified in the simulations performed for Section 3.8.2 as we encountered issues with the electrodes discharging when high voltages were applied to the magnets.

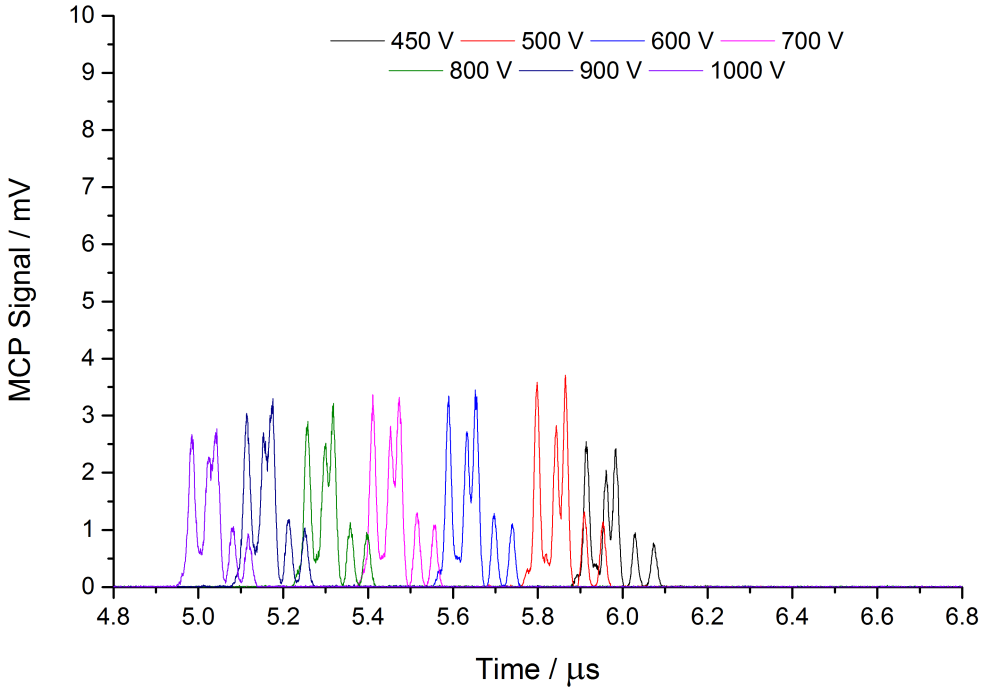

Fig. 7.4 Xe REMPI signals without extraction tube or top magnet active. The voltage on the bottom magnet increases from right to left and the voltages of the other components were fixed at: MCP = −1500 V, time-of-flight tube = −800 V, extraction tube = 0 V, top magnet = 0 V respectively. The signals shown are averaged over 1000 laser shots.

As can be seen in Fig. 7.4, when increasing the voltage of the bottom magnet the time-of-flight of the ions significantly reduces. This stands to reason as with a higher voltage the ions are accelerated more and thus reach the MCP faster. If we look at how the REMPI signal changes for increasing voltage we can see that at higher voltages the individual isotope peaks become less distinct. This also stands to reason

as the faster the ions are moving, the less time there is for the individual masses to separate. In terms of overall signal, there is little difference in the magnitude of the signals for increasing voltages. However, at voltages below 500 V the signal intensity dropped off rapidly. This indicates that there is a minimum amount of energy required to push the ions to the MCP. Thus if the voltage of the bottom magnet is too low the ions are less likely to proceed along trajectories which will result in them reaching the MCP.

From the results shown in Fig. 7.4, it is clear that without the top magnet and extraction tube, the ions can still be detected and mass-resolved. That said, as we were able to fix the shorting issue we also tested the apparatus with the extraction tube active to determine if there would be any improvement. The ion signals obtained with both the top magnet and the extraction tube active are given in Fig. 7.5.

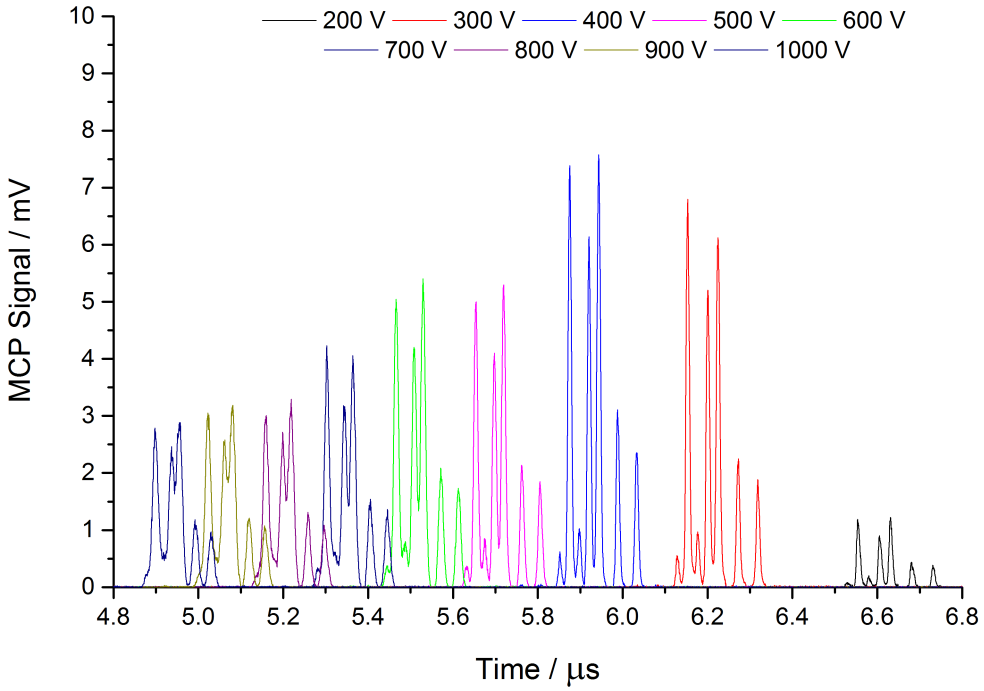

Fig. 7.5 Xe REMPI signals with extraction tube and top magnet active. The voltage on the bottom magnet increases from right to left and the voltages of the other components were fixed at: MCP = −1500 V, time-of-flight tube = −800 V, extraction tube = −200 V, top magnet = 100 V respectively. The signals shown were averaged over 1000 laser shots.

From Fig. 7.5 several trends are clearly apparent. First, as with Fig. 7.4, the resolution between the mass peaks reduces for increasing voltage on the bottom

magnet, which is once again due to the speeding up of the ion path. However, unlike the previous measurements, the intensity of the signal also decreases at the higher voltages, coming to a maximum at around 400 V. Another distinguishing feature of these measurements is that there is still significant ion signal below 500 V. Both of these features are likely due to the influence of the extraction tube. It is likely that because of the additional attraction from the negative charge on the extraction tube that the ions would be accelerated by a greater degree thus allowing extraction of ions from the trap volume with a reduced repulsive voltage from the bottom magnet. Additionally, the shape of the electric field that emanates from the extraction tube could explain why the ion signal reduces at higher voltages. This is because extraction tube acts as a form of funnel sucking in ions from a broader range as opposed to pushing them directly upwards. This means that the trajectories of the ions moving through the time-of-flight tube are no longer linear, which would result in a higher probability of collisions with the walls of the tube.

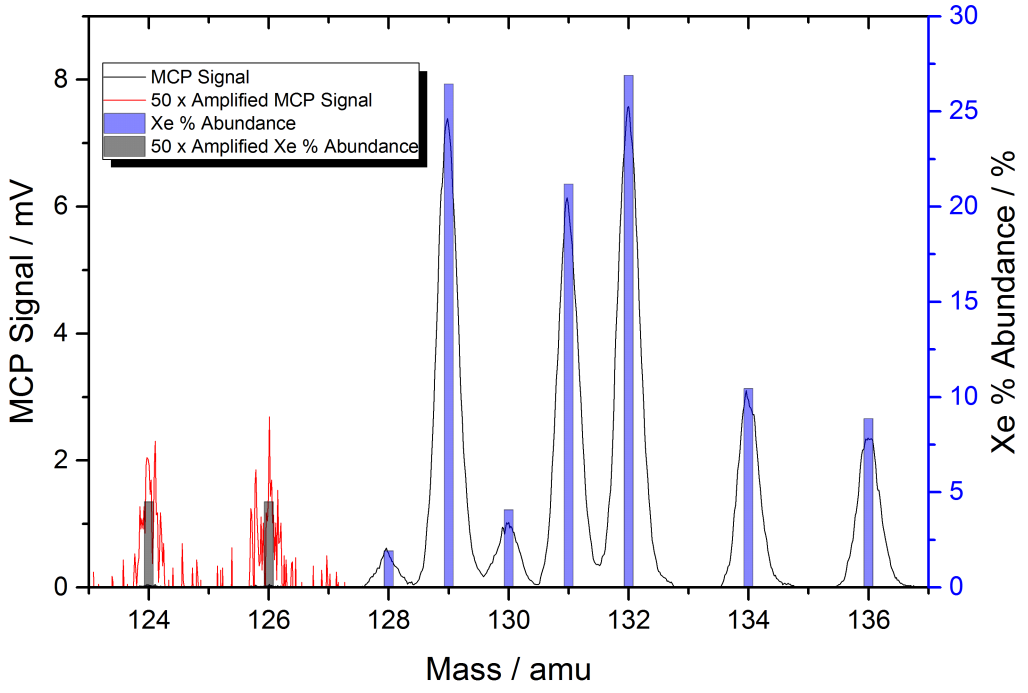

Fig. 7.6 Calibrated mass spectrum of Xe recorded with the REMPI apparatus along with the natural relative isotope abundances of Xe taken from [110]. On the left hand side of the graph for isotopes at 124 u and 126 u the MCP signal and relative abundances have been amplified by a factor of 50. The voltages used for this measurement were: time-of-flight tube = −800 V, extraction tube = −100 V, top magnet = 100 V and bottom magnet = 400 V.

In terms of the mass resolution of the apparatus, the times-of-flight can be calibrated to give a mass value by using a known mass peak in the time-of-flight spectrum, as shown in Fig. 7.6. From this we can see that the neighbouring isotopes of Xe can be distinguished from each other. Additionally, the results show some promise in terms on the sensitivity of the apparatus as the low abundance isotopes ^{124}Xe and ^{126}Xe are measurable from this experiment, which did not approach the limits of detection for the apparatus.

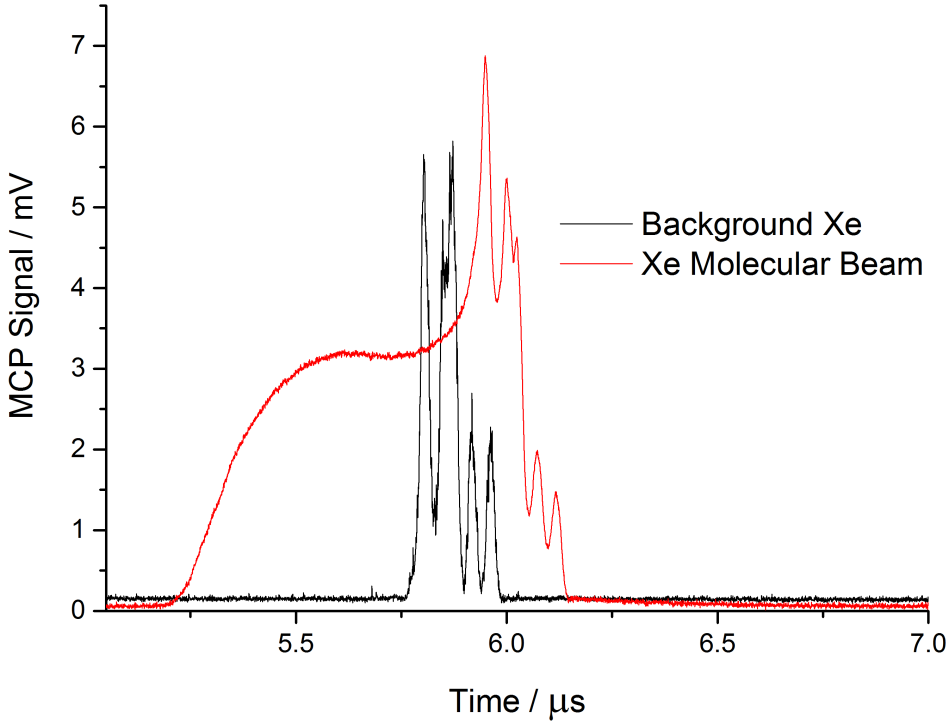

Fig. 7.7 Xe REMPI signal taken to illustrate the effect of the Coulomb explosion. The red line shows the MCP signal taken with full probe laser power at the peak of a molecular beam of pure Xe and the black line shows the signal taken with the residual Xe left in the chamber. In both cases the signals were averaged over 1000 shots.

An important consideration of this detection system is the possibility of Coulomb explosions as shown in Fig. 7.7. This occurs when the probe laser produces a large number of ions in a small volume of space. As a result of the high density of charge, the ions can repel each other resulting in a broadening of the mass peaks. Fig. 7.7 shows an extreme example of this where the faster ions are saturating the microchannels that they hit thus resulting in a flat line with no mass resolution. The slower ions on the tail of this signal have more time to spread out and can thus hit a larger number of channels resulting in a stronger signal and (somewhat)

maintained mass resolution.

7.3.3 Mass-resolving mode vs Hoover mode

As the photostop experiment necessitates the measurement of molecules over several orders of magnitude, the detection method would need to be highly sensitive in order to detect the small numbers of trapped molecules. This is why we conceived the signal maximising or "Hoover" mode, which required both magnets to be grounded and the extraction tube to extract the ions in the trap. However, when tested the signal obtained from the "Hoover" mode is significantly weaker than expected, as can be seen with a comparison with the mass resolving mode in Fig. 7.8.

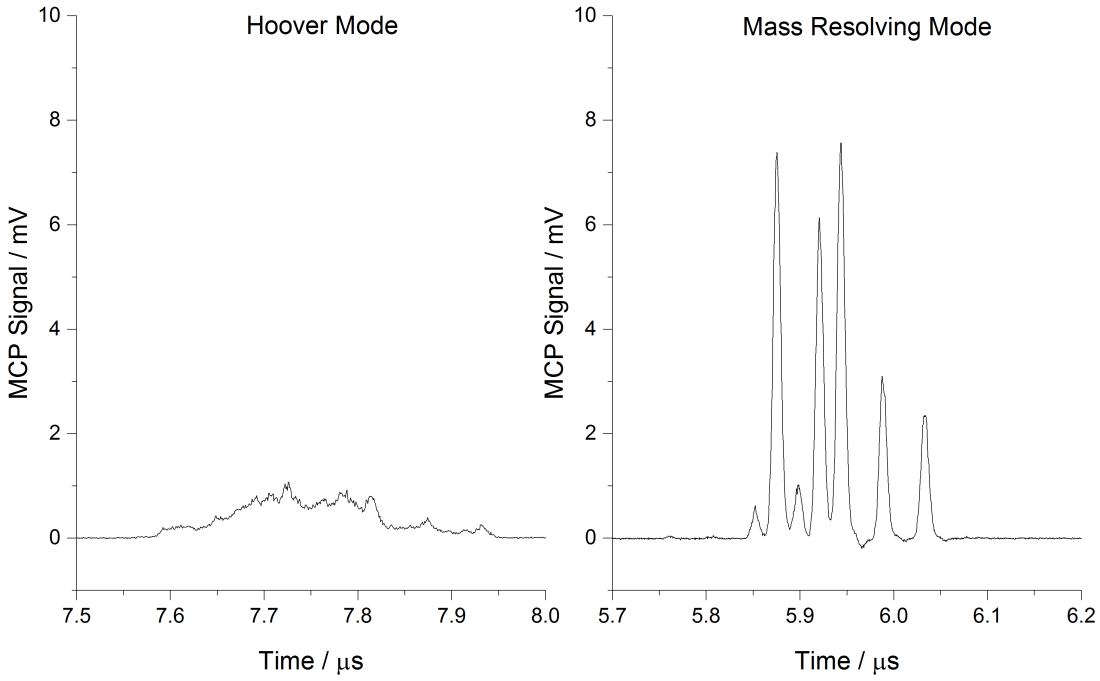

Fig. 7.8 Comparison of "Hoover" and mass resolving mode signals. In both cases the MCP signals were averaged over 1000 laser shots and the voltages of each of the ion extraction components was optimised to maximise the signal shown (within the bounds of the available equipment at the time). The voltages used for the hoover mode were: time-of-flight tube = −800 V, extraction tube = −200 V, top and bottom magnets = 0 V, and for the mass resolving mode: time-of-flight tube = −800 V, extraction tube = −100 V, top magnet = 100 V and bottom magnet = 400 V.

7.3.4 Fast Ionisation Gauge Measurements

With the newly operating fast ionisation gauge, measurements were taken of the molecular beam profile of a beam of pure Ar in an effort to characterise the operation of the nozzle. An example molecular beam profile is given in Fig. 7.9. The profile recorded at the FIG consists of two primary parts, a narrow sharp spike followed by a larger, more gradual rise which then decays. The first component is the portion of the molecular beam which passes through the molecular beam skimmer and hits the FIG directly. The second part is the gas which does not make it through the skimmer, but instead takes a more circuitous route around the outer stage and onto the FIG. As the molecular beam is not sent directly into a pump, there is a certain amount of build up of gas in the FIG chamber, but eventually the gas that remains is pumped away; this is the root of the initial rise and gradual decay on the trace. As shown on the graph, the FIG can be calibrated to give approximate measurements of the number density of gas in the FIG volume by comparing the magnitude of the FIG signal with and without the molecular signal and contrasting this with averaged pressure measurements taken using the chamber's ion gauge. However, in practice the ionisation efficiencies of different molecules by the FIG can be wildly different so this calibration process will largely be species specific. An important feature to note is that the tail of the second part of the molecular beam trace does not reduce down to the initial base level before the second molecular beam pulse arrives. This effectively means that the chamber is not sufficiently pumped by the turbopump to remove all the gas from the previous molecular beam pulse before the next arrives. This issue could easily be combated by reducing the repetition rate of the experiment or providing additional pumping (e.g. using the cryostat).

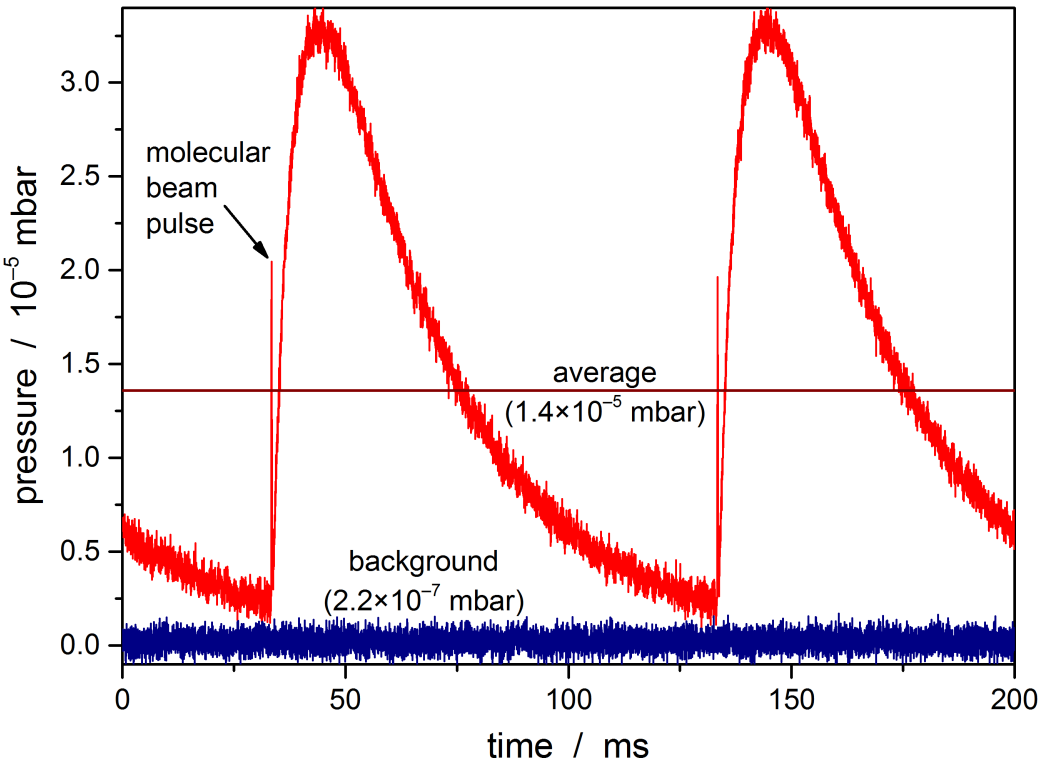

(a)

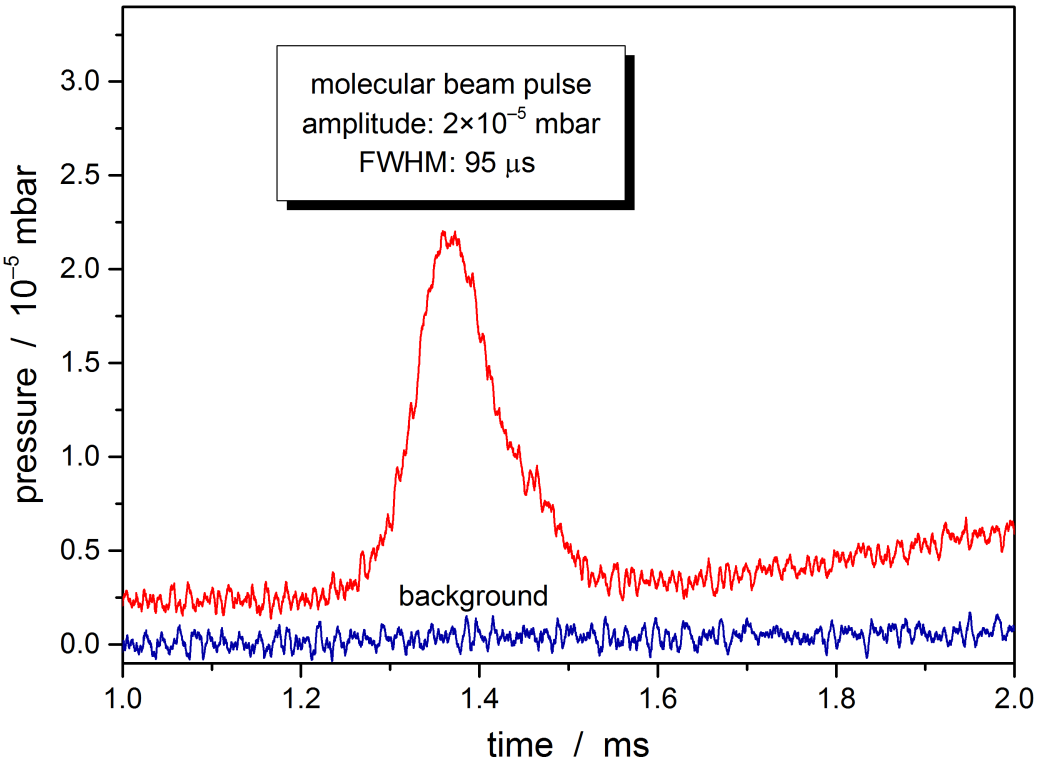

(b)

Fig. 7.9 Measured Molecular beam profiles of a pure beam of Ar fired from a General Valve with a repetition rate of 10 Hz. This has been separated into the full profile over two shots (a) and the isolated profile that passes through the molecular beam skimmer (b).

7.4 Discussion

From the optimisation process it is clear that the apparatus is performing appropriately in detecting ions produced by a REMPI process. Additionally, from the signals obtained using the mass resolving mode, individual Xe isotopes can be distinguished by mass (see Fig. 7.6), meaning that the apparatus is an effective time-of-flight mass spectrometer.

When examining the "Hoover" mode in action the performance appears to fall significantly short of the predictions, as the signal strength from the "Hoover" mode is noticeably weaker than the mass resolving mode. On re-examining the SIMION simulations we have found that there are two potential sources for this discrepancy. The "Hoover" as simulated involves sucking the ions down a very shallow potential gradient which gets steeper as the ions approach the extraction tube; as such the attractive force on the ions in the trap centre with this mode is fairly weak. On account of the weakness of this attraction the effectiveness of the ion extraction is highly sensitive to a number of factors. One such factor, which was not accounted for in the initial simulation was the forward velocity of the molecular beam itself, which would deflect the ions on their path towards the extraction tube thus making them more likely to collide with the walls. Another feature that was not accounted for as the build up of residual charge on the magnets from ion impacts. Although both magnets were grounded for the "Hoover" mode experiments, there remains the possibility that there is some residual charge build up on the magnets from ion impacts which can significantly impede the ion extraction process. In fact, on examining Fig. 7.8, some evidence of mass resolution is present in the "Hoover" mode signal, suggesting that there is some potential difference between the magnets, as from the simulations the "Hoover" mode should not demonstrate mass resolution. Further, simulations using SIMION have suggested that a potential difference of even 0.1 V can significantly disrupt the operation of the "Hoover" mode.

Despite the issues that plague the "Hoover" mode there does remain some potential for its use. Although the velocity of the molecular beam has proved problematic

for these measurements, the velocity dependence of the extraction efficiency could become useful for isolating slower moving molecules; specifically, by decreasing the voltage on the extraction tube to isolate slower moving species. However, by altering the voltage on the extraction tube the trajectories of the ions exiting the tube will also vary meaning that the voltage of the time of flight tube would need to be adjusted as well to ensure proper focussing of the ions onto the detector. This could create a problem when it comes to significantly weaker signals as re-optimising the voltage based on weak ion counting signal could be problematic. Additionally, the current apparatus does not allow for velocity mapping of the detected ions so although it may be possible to select out slower velocities currently there would be no direct way to measure them. That said, if these issues could be directly combated, the potential for the "Hoover" mode to selectively extract slow moving molecules from the trap is a promising prospect that is worthy of further attention.

7.5 Conclusions and next steps

The results from these initial tests have shown that the apparatus is successful in detecting ions from REMPI. Although the initial intention was to use the "Hoover" mode for ion extraction it is clear that there a still some significant issues with this method. As such for future experiments the mass-resolving mode would be used as the signal from this is significantly stronger. Given the success of these tests the next step was to use this apparatus to measure the decay in signal from the photostop process.

8. PHOTOSTOP OF SH AND SULPHUR USING REMPI

8.1 Introduction

Following on from the testing of the REMPI apparatus the clear next stage was to apply this to measure the decay of molecules in the probe volume from photostop. The intention of this is to show trapping of SH molecules from this process, which requires us to identify and isolate SH signal as well as measure the molecular beam speed, which would then be tuned to maximise the potential for producing zero velocity molecules as outlined below.

8.2 Adjustments to experiment

For the initial stages of the experiment, much of the apparatus remained the same as for the initial tests using Xe. However there were issues with cooling and the difficulty in mounting the smaller outer stage without direct contact between the inner and outer stage structures. Due to this we redesigned the outer stage to allow easier access and greater flexibility as shown in Fig. 8.1. This new structure allows easier access to the trap housing so that alterations can be made quickly, as well as giving a greater volume inside the trap housing so that it is less likely that gas will get trapped inside. Further, the inner walls of this new outer stage were coated with activated charcoal using Stycast 2850 FT adhesive. The benefit of this being that it effectively increases the surface area of the inner walls allowing them to adsorb more gas onto them and therefore become more efficient pumping surfaces.

An additional alteration was made to the nozzle mount to allow for adjustment of the tension in the General Valve in vacuo as shown in Fig. 8.2. The intention of

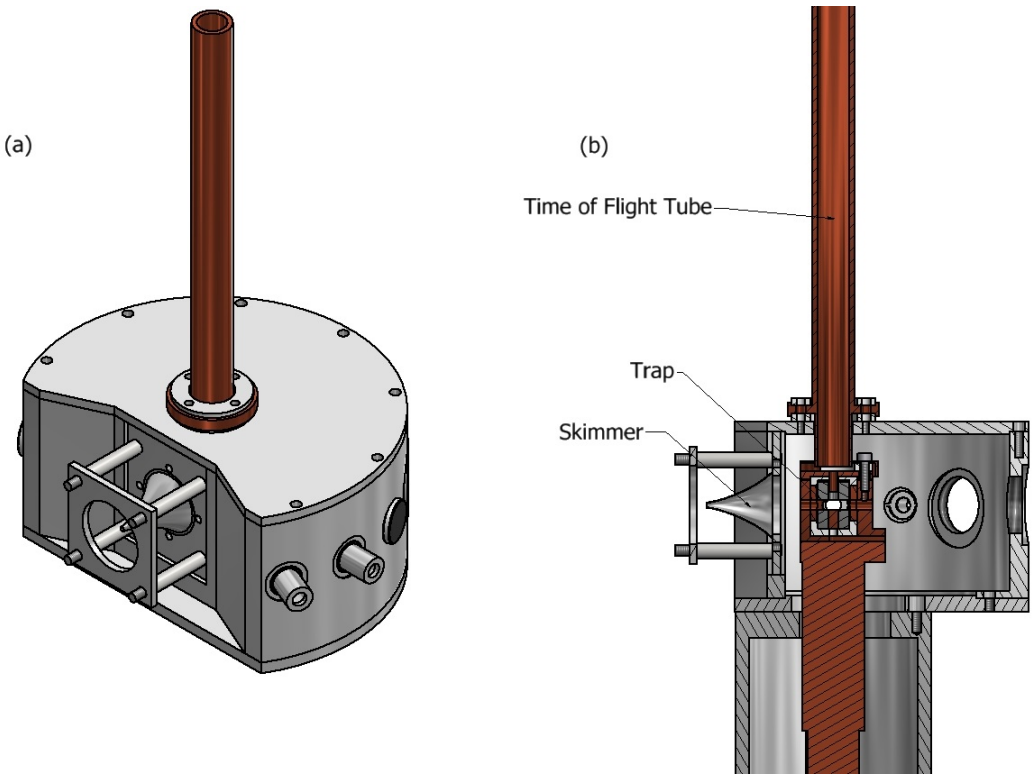

Fig. 8.1 Schematic representation of the larger outer stage. The larger internal volume is to allow for a greater ease of access.

this being to allow for greater flexibility and control of the molecular beam profile in order to obtain a sharp and narrow molecular beam pulse. Additionally, this larger and more sturdy structure will help avert some of the issues with distortion of the components of the previous configuration.

Although it is a reliable and readily available molecular beam source, the Parker General Valve is not necessarily the best molecular beam source available for producing narrow high density beams. On account of this for later stages of this experiment an Even-Lavie valve replaced the General Valve for the majority of the results presented here[1], as this has previously demonstrated the capability of producing very narrow high density beams [111]. On account of the high densities produced by the Even-Lavie valve some consideration needed to be made with regards to how the molecular beam passes through the skimmer. The skimmer we had available was designed for lower density beams and has a relatively narrow angle at the orifice. The upshot of this was that, with a high density molecular beam travelling through

[1] This will be the case for all the results in this chapter unless otherwise specified.

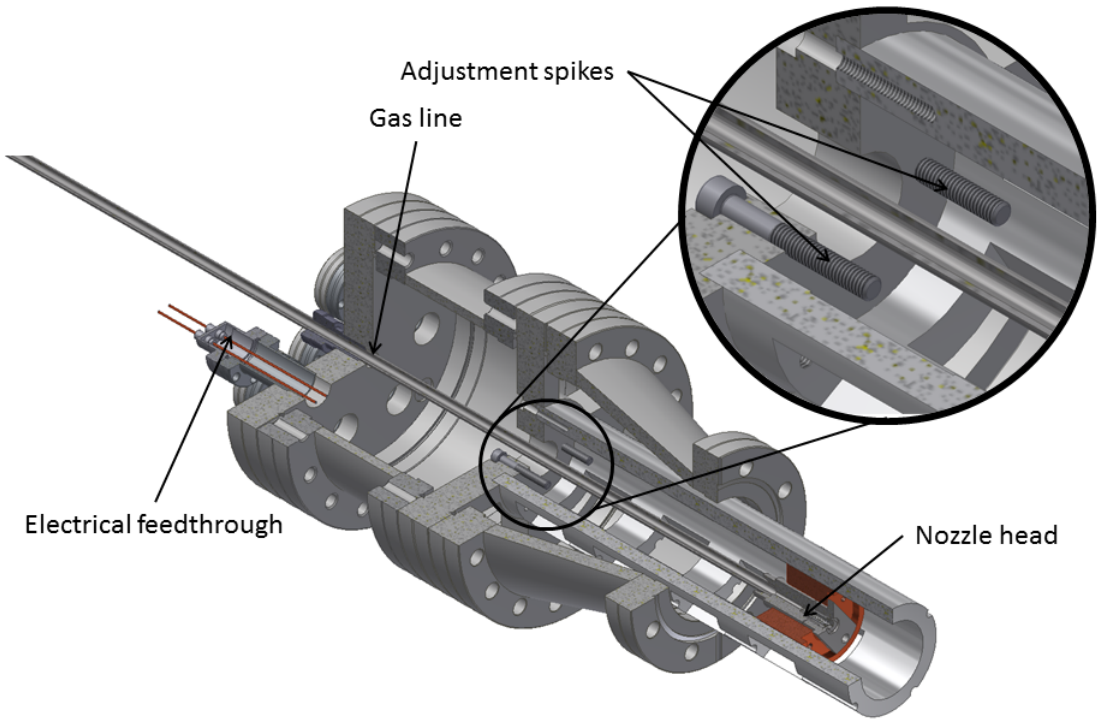

Fig. 8.2 Schematic representation of the adjusted nozzle mounting assembly. To adjust the General Valve tension the nozzle is pulled back onto two screws mounted on the flange, which stick into the nozzle mount and provide resistance so that the nozzle can be adjusted.

a narrow orifice, turbulence may hinder the passage of the beam. To minimise this risk the Even-Lavie valve was positioned at a significantly greater distance from the skimmer than the General Valve in the hopes of reducing the effect. This ultimately meant that the molecular beam would likely be less dense when reaching the trap centre, but as the Even-Lavie is significantly more directional than the General Valve, it was still likely to be an improvement.

8.3 Results

8.3.1 Finding SH signal

The clear first step in performing the photostop experiment is to identify signal from the target molecule in question namely, find SH REMPI signal. To do this we initially set the wavelength of the probe laser to be in the expected region of a band head of SH and (with the delay between the dissociation and probe lasers set to 5 ns) adjusted the delay between the firing of the molecular beam nozzle and the firing of the dissociation laser. From this we were able to obtain sufficient REMPI signal to optimise and then obtain the spectrum shown in Fig. 8.3.

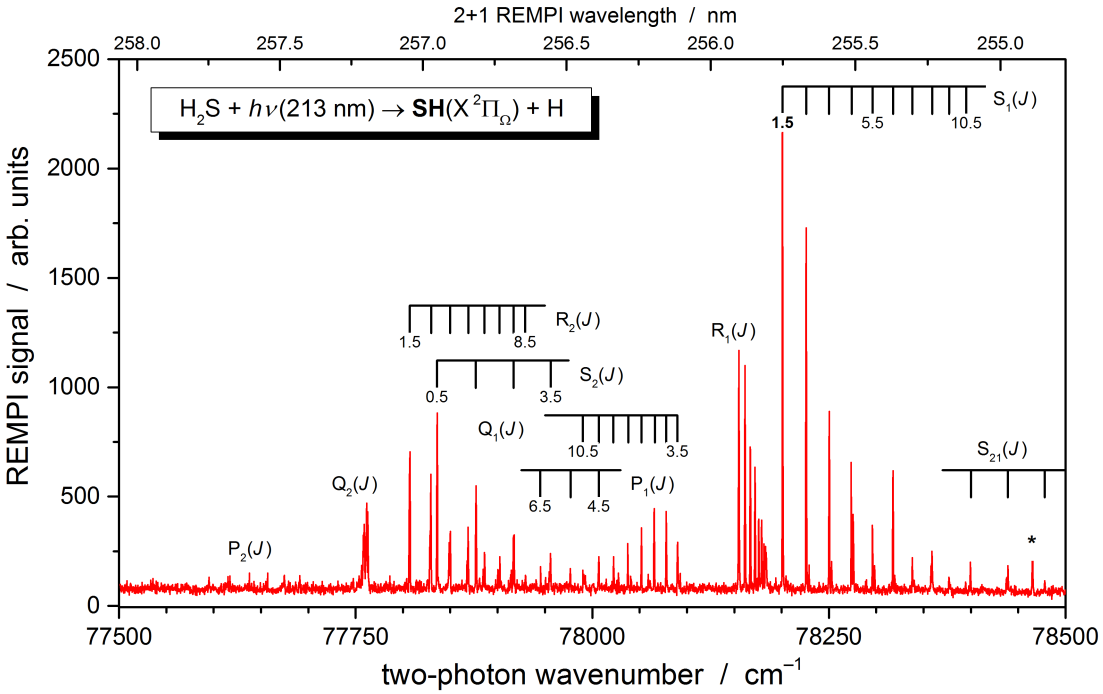

Fig. 8.3 REMPI Spectrum of SH from dissociation of pure H_2S. For this the REMPI signal is measured using the integral of the MCP signal, which is optimised for changes in the power of the dissocation and probe lasers.

Fig. 8.3 can clearly be matched up with previous measurements from the literature [112], suggesting that this is in fact SH. However one peak at approx 254.8 nm (78 450 cm^{-1}) does not fit into the known peaks from SH. When looking further into this particular peak we discovered that this peak was in fact the result of a Coulomb explosion (see Fig. 7.7 for explanation) from a neighbouring mass region. By examining this time-of-flight region as opposed to the SH region, we obtained

the spectrum shown in Fig. 8.4.

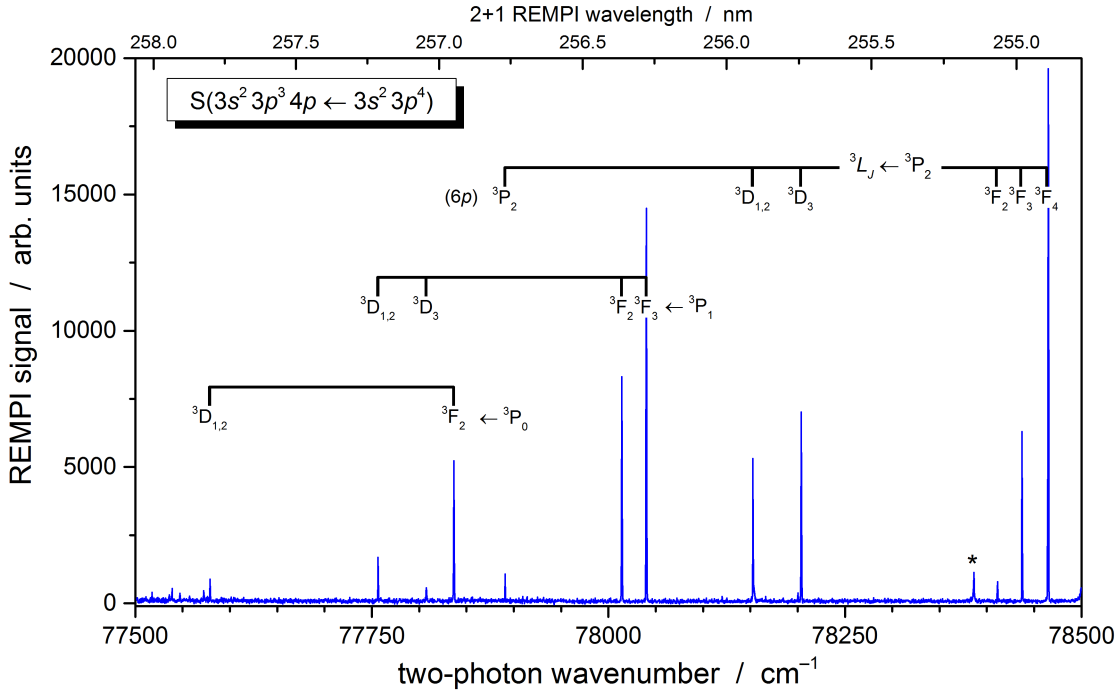

Fig. 8.4 REMPI Spectrum of S from the two stage dissociation of pure H_2S.For this the REMPI signal is measured using the integral of the MCP signal, which is optimised for changes in the power of the dissocation and probe lasers.

Upon examination we have found that the spectrum shown in 8.4 corresponds to the $2+1$ REMPI of sulphur atoms. Given the precursor molecule in this case, it is reasonable to assume that this sulphur has been produced from the dissociation of H_2S so we decided to look into this further (as will be outlined in the next section).

8.3.2 SH dissociation mechanism

To determine the mechanism behind the production of sulphur atoms from H_2S we examined the power dependence of the MCP signal on the intensities of the probe and dissociation lasers, which should indicate how many photons of each are required to produce the signal. The results from this analysis are shown in Fig. 8.5.

By performing a linear fit on these graphs one can ascertain the power dependence of the process, i.e. how many photons of each laser are required to produce the ions seen by the MCP. From this we find that there is a gradient of 2.4 for the probe laser indicating that this is a $2+1$ REMPI process, and 1.8 for the dissociation laser

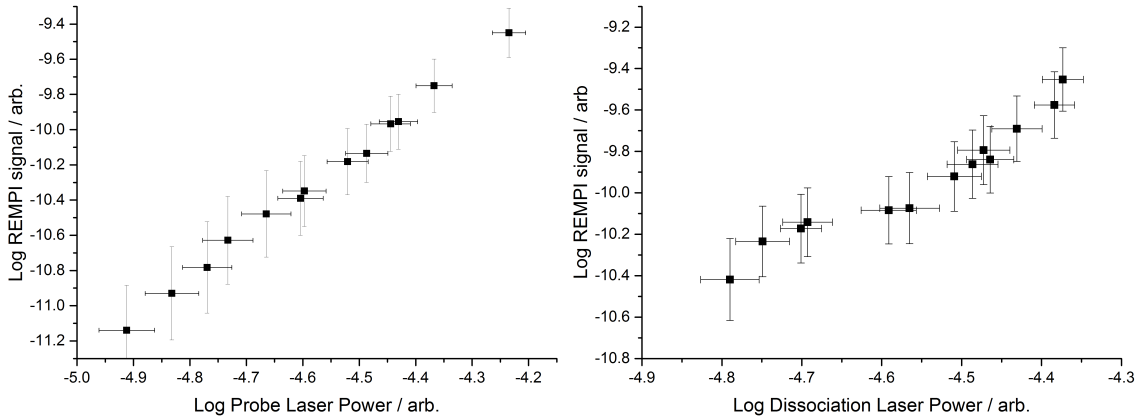

(a) (b)

Fig. 8.5 $\log_{10}$ Power dependencies of the discovered S signal on the probe (a) and dissociation (b) laser energy.

suggesting that this is a two photon process.

Based on these findings and with a further examination of the potential energy surfaces of SH the mechanism for this process can be proposed as illustrated in Fig. 8.7. We are using a 213 nm laser to dissociate the H_2S, which should produce SH predominantly in the ground state. However there is a strong Franck-Condon overlap between the $X^2\Pi_{3/2}$ SH ground state and the $a^4\Sigma^-$ unbound state for an excitation with a 213 nm photon, meaning that the SH can dissociate from a second absorption (see Fig. 8.6). At first glance this discovery appears detrimental to the goal of trapping SH as we are effectively draining the supply of stopped SH molecules to produce sulphur. However this does also pose the question as to whether sulphur atoms could be photostopped using a two stage dissociation. In a similar manner to the one step photostop process, the energetics of the photodissociation can be examined in order to determine the recoil velocity of the sulphur atoms from the second dissociation.

If we first look at the dissociation of H_2S, referring back to Chapter 2, in the centre of mass frame of the photodissociation the velocities of the SH fragment are given by

$$u_{\mathrm{SH}} = \left(2E_{\mathrm{kin}}.\frac{m_{\mathrm{H}}}{m_{\mathrm{SH}}.m_{\mathrm{H_2S}}}\right)^{1/2}, \tag{8.1}$$

where u_{SH} is the recoil velocity of the SH in the centre-of-mass frame, m_{SH}, $m_{\mathrm{H_2S}}$

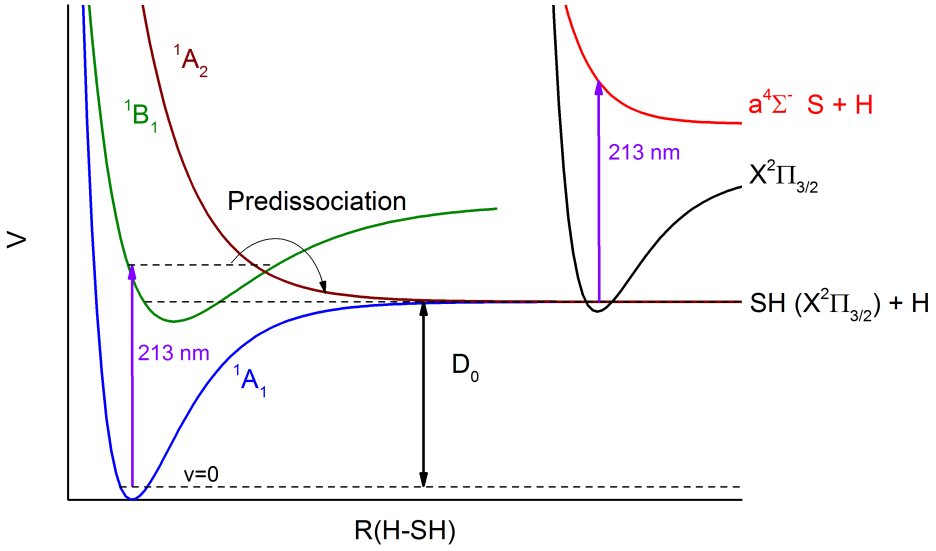

Fig. 8.6 Energy transitions for the H_2S and SH dissociation mechanisms.

and m_H are the masses of SH, H_2S and H respectively and E_{kin} is the total kinetic energy of the fragments as defined by

$$E_{kin} = E_{kin}(SH) + E_{kin}(H) = h\nu - D_0 - E_{int(frag)} + (E_{int(H_2S)}), \tag{8.2}$$

where ν is the frequency of the dissociation laser photons, D_0 is the threshold dissociation energy of the molecule and $E_{int(frag)}$ is the internal energy of both fragments and $E_{int(H_2S)}$ is the internal energy of the H_2S[2]. As the excitation in question is to the ground state of SH (as well as the ground state of H) and using the value of D_0 from [113], we can determine that from dissociation by a 213 nm laser will produce a recoil velocity of

$$u_{SH} = 576\,\mathrm{m\,s^{-1}}. \tag{8.3}$$

Thus by using a $576\,\mathrm{m\,s^{-1}}$ molecular beam one can expect to produce SH molecules with velocities of approx $0\,\mathrm{m\,s^{-1}}$. In practice however the final recoil velocity from this is also influenced by the initial orientation of the dissociated molecule. Not all of the molecules will necessarily be orientated such that the target fragment will recoil directly opposed the propagation of the molecular beam. In fact, given a random orientation a dissociation process could result in the fragments ejecting in essentially

[2] This will be disregarded for reasons outlined in Chapter 2.

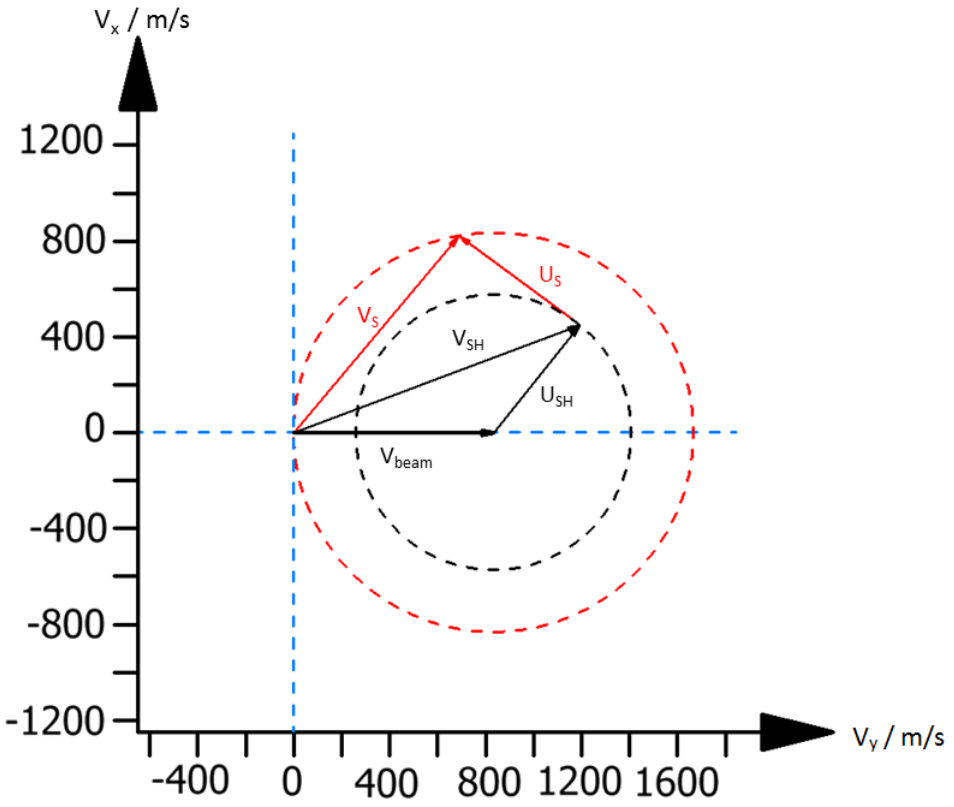

Fig. 8.7 Newton diagram of the photodissociation of SH and S performed by a 213 nm dissociation laser.

any direction, leading to a isotropic distribution of recoil velocities. However the excitation which initiates the dissociation of H_2S has a transition dipole moment which requires a perturbation which is perpendicular to the molecular plane. The upshot of this is that with a linearly polarised laser (such as the dissociation laser we have used) molecules with their plane perpendicular to the laser polarisation will be dissociated preferentially. This ultimately means that when dissociating with the polarised laser, the recoil velocities will occur with a $\cos^2$ distribution with respect to the laser polarisation. In this experiment the dissociation laser is aligned perpendicular to the propagation of molecular beam. This means that if the polarisation of the dissociation laser is orientated perpendicular to the plane of the molecular beam and the laser propagation, this gives rise to velocities on the black dashed circle in the Newton diagram shown in Fig. 8.7 in the xy plane of the experiment.

Similarly the recoil velocity of the S atoms can be determined using the same princi-

ples. From this and using the SH dissociation energy from Equation 8.2, we find that the direct recoil of the S atoms from the photodissociation (in the SH centre-of-mass frame) is

$$u_S = 627\,\mathrm{m\,s^{-1}}. \tag{8.4}$$

Next we need to consider the geometric environment of the photodissociation in order to determine the total resultant recoil velocity from the combination of both processes. In the ground state the H_2S molecule has a bond angle of approximately 90.1°, which does not change significantly during dissociation via the $^1B_1$ and $^1A_2$ excited states [114]. Further, the dissociative transition for the SH is also perpendicular transition, so the recoil velocities from the second dissociation should be preferentially in the same plane as the prior dissociation. Hence we can project this onto the calculations of the recoil velocities of the H_2S and SH dissociations and thus generate a Newton diagram of the final velocity of the S atoms in the lab frame as shown in Fig. 8.7. This gives us a target molecular beam speed of

$$v_{\mathrm{beam}} = 834\,\mathrm{m\,s^{-1}}, \tag{8.5}$$

in order to produce photostopped sulphur atoms with this mechanism. It should be noted that at this stage this model is a supposition and requires that the SH molecule does not rotate between the dissociation of H_2S and the dissociation of SH.

8.3.3 Tuning the molecular beam speed

As the velocity of the molecular beam is critical to the photostop process, it needs to be carefully controlled to match the recoil velocity of the photodissociation. As this REMPI detection system does not allow for velocity map ion imaging (VMI), we determined the molecular beam speed by measuring the molecular beam profile at both the centre of the trap (where the probe laser intersects the molecular beam) and the fast ionisation gauge. By measuring the time difference between the centres of each molecular beam peak and measuring the distance between the trap centre

and the FIG, we determined the molecular beam speed.

As outlined in Chapter 2, for a one stage photostop the desired molecular beam velocity can be determined from the dissociation laser using the equation:

$$v_{\text{beam}} = u_{\text{SH}} = \left(2E_{\text{kin}}.\frac{m_{\text{H}}}{m_{\text{SH}}.m_{\text{H}_2\text{S}}}\right)^{1/2}, \tag{8.6}$$

where v_{beam} is the target molecular beam speed, where u_{SH} is the recoil velocity of the SH in the centre-of-mass frame, m_{SH}, $m_{\text{H}_2\text{S}}$ and m_{H} are the masses of SH, H_2S and H respectively and E_{kin} is the total kinetic energy of the fragments as defined by Equation 8.2. To control v_{beam} the parent molecule was seeded in a mixture of noble gases which, if properly mixed, will speed up or slow down the molecular beam speed depending on the mass of the noble gas in question. If the seeding gas has a greater mass than the target gas then by collisions with the seeding gas the target molecules will slow down, resulting in a slower molecular beam; and the reverse is true for lighter seeding gases. By using equation 8.6, we determined that for a dissociation of H_2S at 213 nm we require a molecular beam speed of 575.6 $\text{m}\,\text{s}^{-1}$. By successively diluting pure H_2S with Kr and measuring the velocity at each dilution we were able to determine the required mixture to produce a close approximation to the photostop velocity as shown in Fig. 8.8.

It should be noted that the dissociation of H_2S produces SH molecules in a range of different rotational states, as evidenced by Fig. 8.3. For each of these states, the recoil will be different as the internal energy of the SH fragments will be different for each. Therefore to photostop each state one would need to use different molecular beam speeds. However, in our case we are examining only the ground state for the purposes of trapping, and so will only be using a single molecular beam speed.

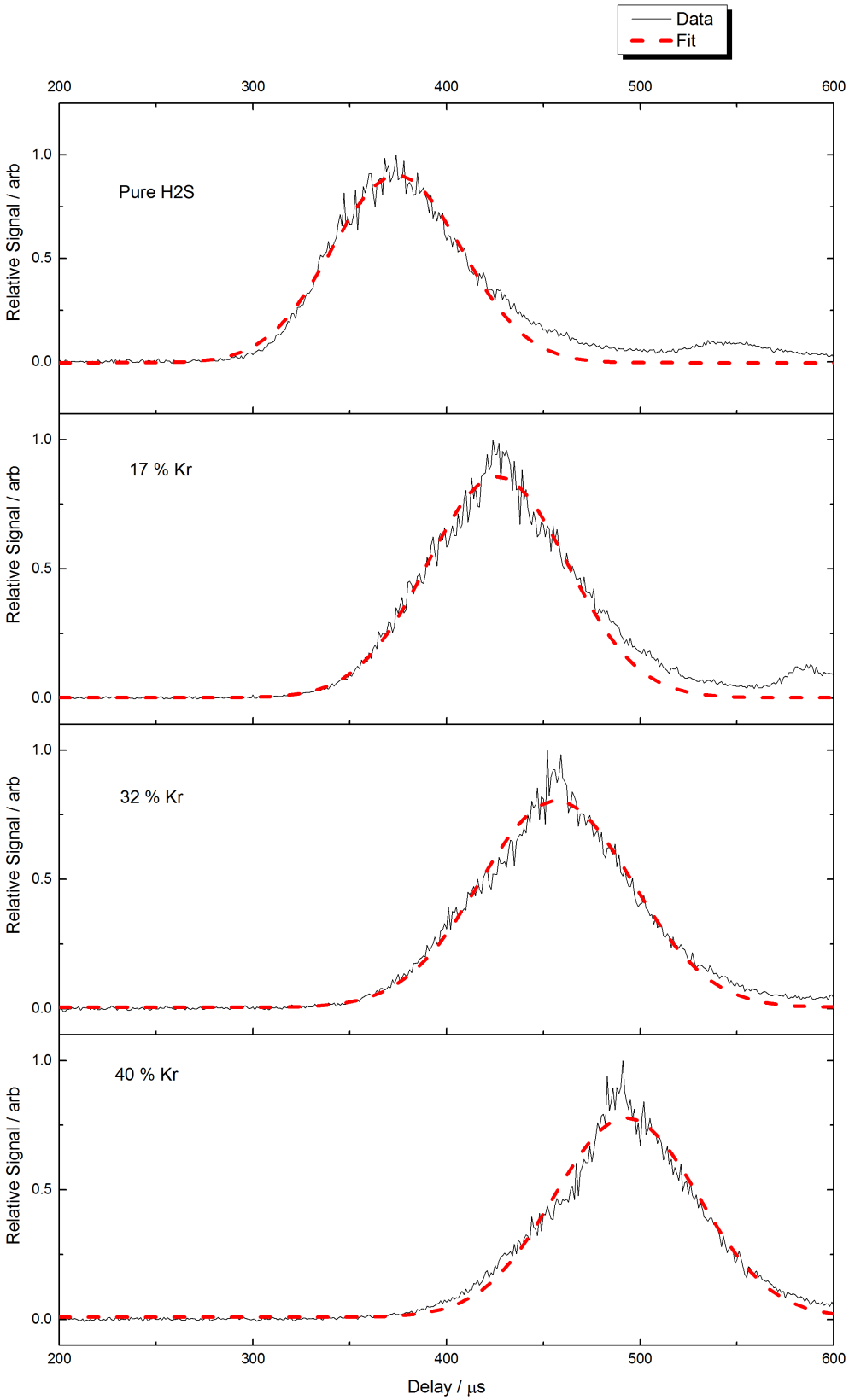

Fig. 8.8 Molecular beam profiles taken using SH REMPI signal. The fits shown were made using a single Gaussian function. The additional rise after the main peak is indicative of un-skimmed gas from the nozzle leaking into the chamber through the laser ports of the outer stage structure on the cryostat.

8.3.4 Room temperature photostop

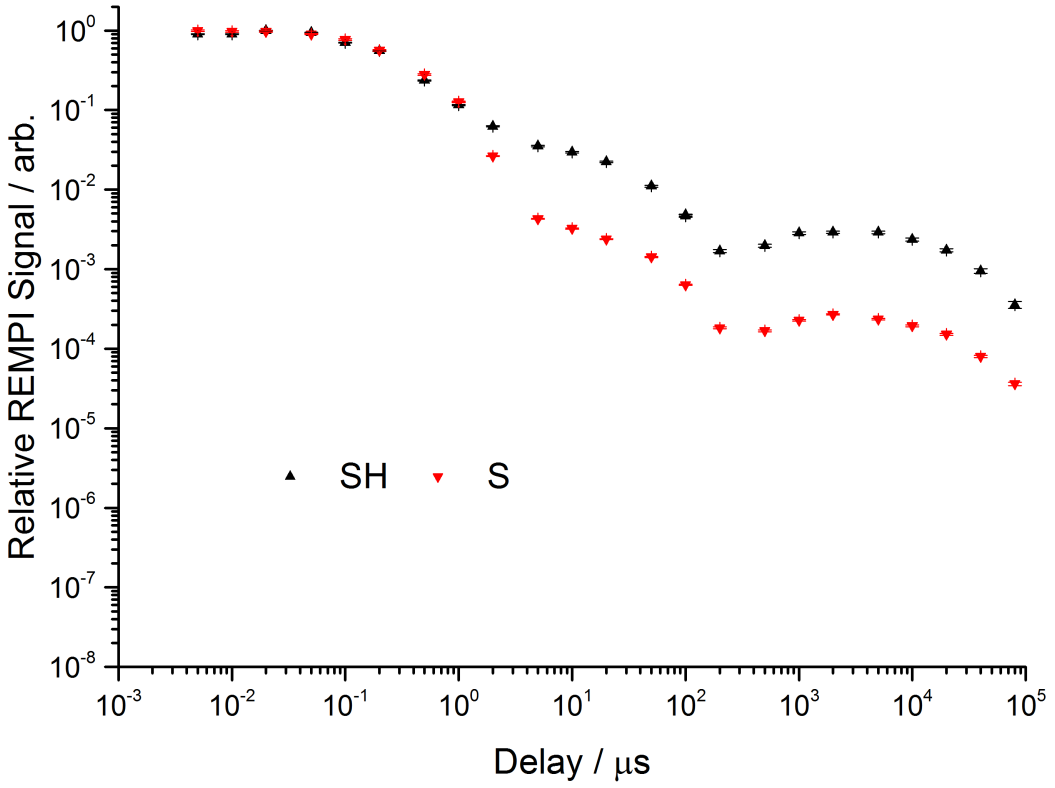

Fig. 8.9 Decay in REMPI signal for increasing delays between the dissociation and probe lasers for both SH and S without the cryostat in operation.

Measurements were made of the REMPI signal as a function of the dissociation laser - probe laser delay. As the REMPI signal decreases over several orders of magnitude, the MCP voltage was sequentially increased to improve the signal on the oscilloscope. At each point the MCP voltage was increased the REMPI signal was remeasured at the same delay to calibrate the different sections with respect to each other.

As a starting point we measured the photostop decay of SH and S without the cryostat in operation so that its effect can be demonstrated. The results of this can be seen in Fig. 8.9. The trends shown clearly indicate a decay in signal with two rises and falls after the initial decay, which we shall refer to as 'humps'. We believe that the first hump is due to the SH/S bouncing off of the magnet surfaces and back into the probe volume and the second is due to gas desorption from the surfaces of the magnets. In any case it is self-evident that in this form there is too much background signal for trapping to be demonstrated, thus making the cryostat

necessary.

8.3.5 Even-Lavie valve characterisation

Due to the requirement of the photostop experiment for a short and sharp molecular beam we decided to replace the General Valve with an Even-Lavie valve. The Even-Lavie valve optimisation is less extensive than for the General valve as it arrives fully constructed with no secondary spring to adjust for shorter molecular beam pulses. For this the only adjustment that could be made was with the length of the driving current pulse for opening the nozzle. Thus for optimisation the nozzle was backed with 3 bar of Ar and the atomic beam optimised by adjusting the length of the driving current pulse. The results from this are shown in Fig. 8.10.

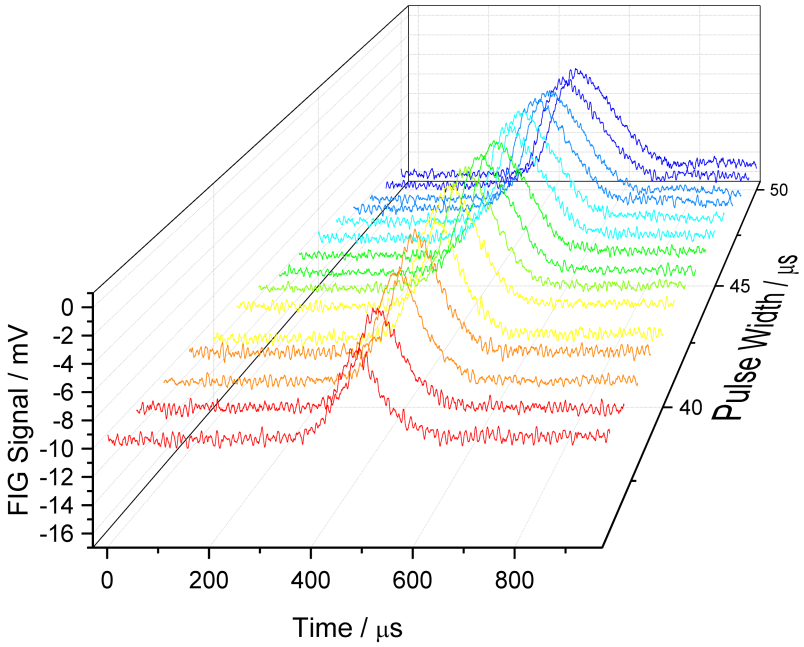

Fig. 8.10 FIG traces for a atomic beam of Ar with increasing driving current pulse lengths on the Even-Lavie.

After performing this initial optimisation, the triaxial cable used to drive the current needed to be re-purposed in another experiment and so was replaced with a coaxial cable. After this adjustment we found that there was a noticeable difference in the operation of the valve and different current pulse lengths were needed to open the valve fully. At present it is not entirely certain what the root cause of this change was

but an initial assessment seems to indicate that the most likely source is the change in the efficiency of the grounding between the cables. The rationalisation of this is thus, the Even-Lavie valve is driven by a current pulse through a (normally) coaxial connection and the current pulse passes through the valve and then dissipates to ground through the shield of the coaxial. Thus with a change in shielding in the cables this dissipation process may occur differently resulting in slightly different properties in the operation of the nozzle. Due to this alteration in the properties of the nozzle the optimisation process was repeated with a beam of Ar but in addition to this, a secondary optimisation was performed by measuring the molecular beam profile of H_2S in the trap centre using the REMPI signal from SH. The results from this are shown in Fig. 8.11.

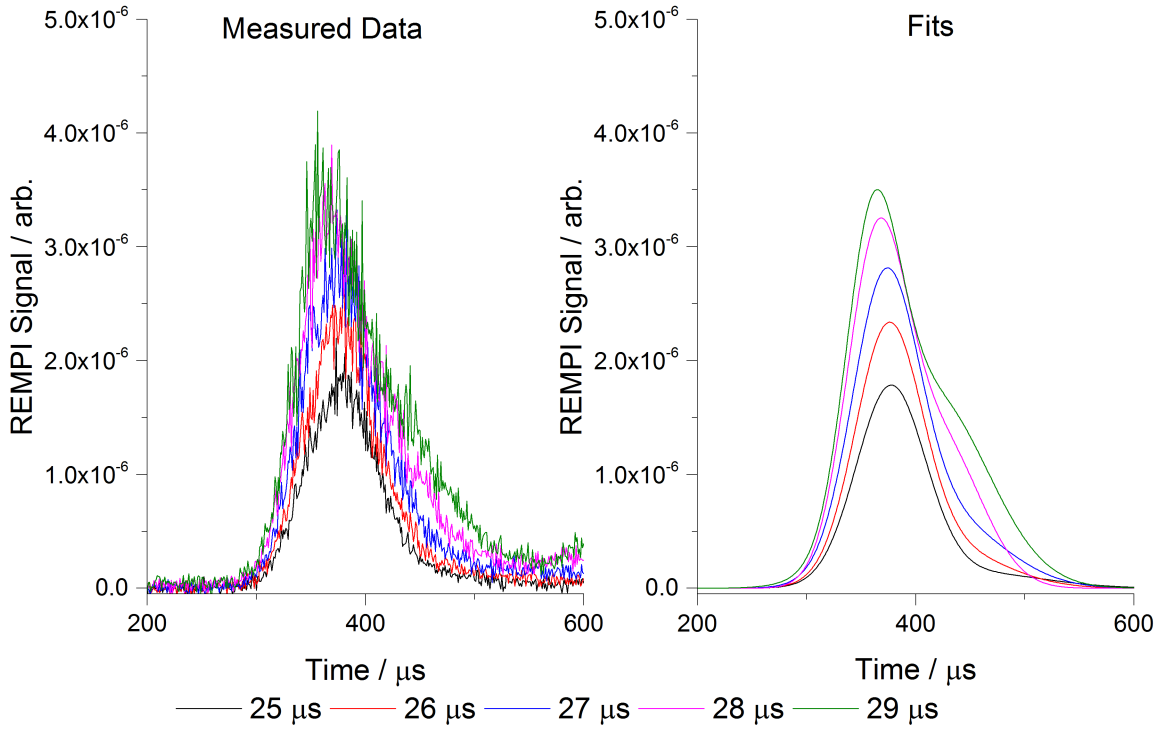

Fig. 8.11 Molecular beam profiles measured using the REMPI of SH with increasing driving current pulse lengths on the Even-Lavie.

As the ideal form of the molecular beam profile for the photostop measurements is a narrow intense molecular beam, the results shown indicate that a compromise must be reached with this configuration. Although there appears to be some increase in signal from 27 µs to 29 µs, the width of the signal appears to also increase, with what appears to be a second peak emerging. This secondary peak could prove

problematic as the increased density in the tail of the molecular beam may result in stopped molecules being pushed out of the trap via collisions. Therefore we would opt for a narrow molecular beam to reduce this possibility. As such a pulse width of 27 µs (which corresponds to a measured full width at half maximum of approx 100 µs using SH REMPI) was chosen for use in the future experiments.

8.3.6 Cryostat-assisted photostop

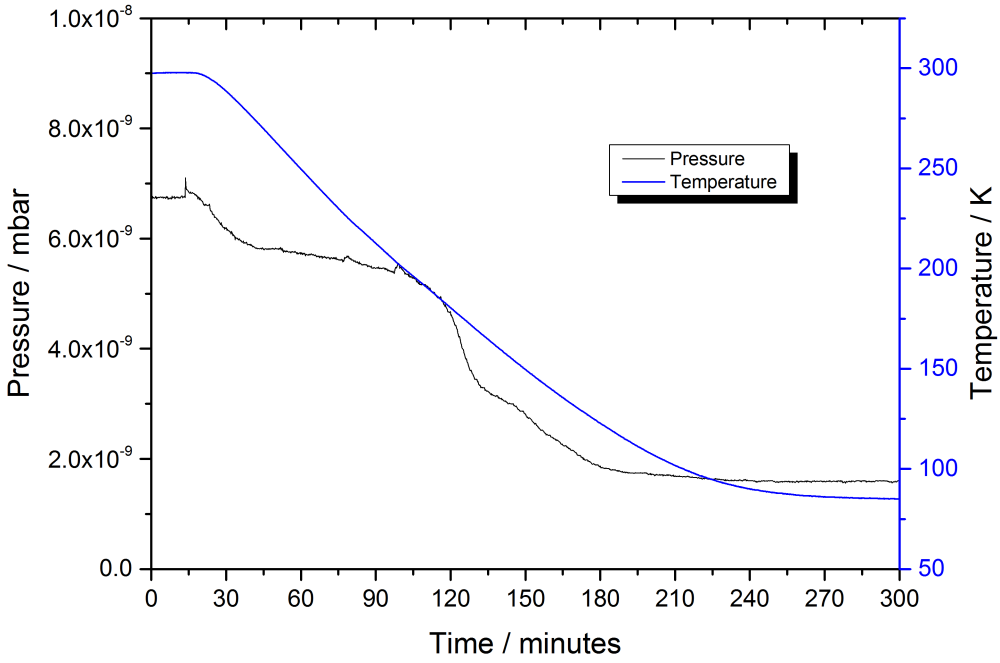

Fig. 8.12 Temperature of the outer stage and pressure of the chamber after the cryostat is turned on.

As with the previous photostop measurements using CELIF with the cryostat active, we measured the temperature of the cryostat as it cooled down to determine the optimum time to start the experiment. However in this case the thermocouple was positioned on the upper portion of the outer stage in order to get a a more accurate measurement of the temperature of the pumping surfaces (i.e. the inner walls of the outer stage). The pumping operation of the cryostat is shown in Fig. 8.12. It is clear from this that the cooling process is taking significantly longer than for the previous measurements. This is most likely due to a combination of the increased mass and repositioning of the thermocouple.

On account of the contraction of the cooling components, the alignment of the

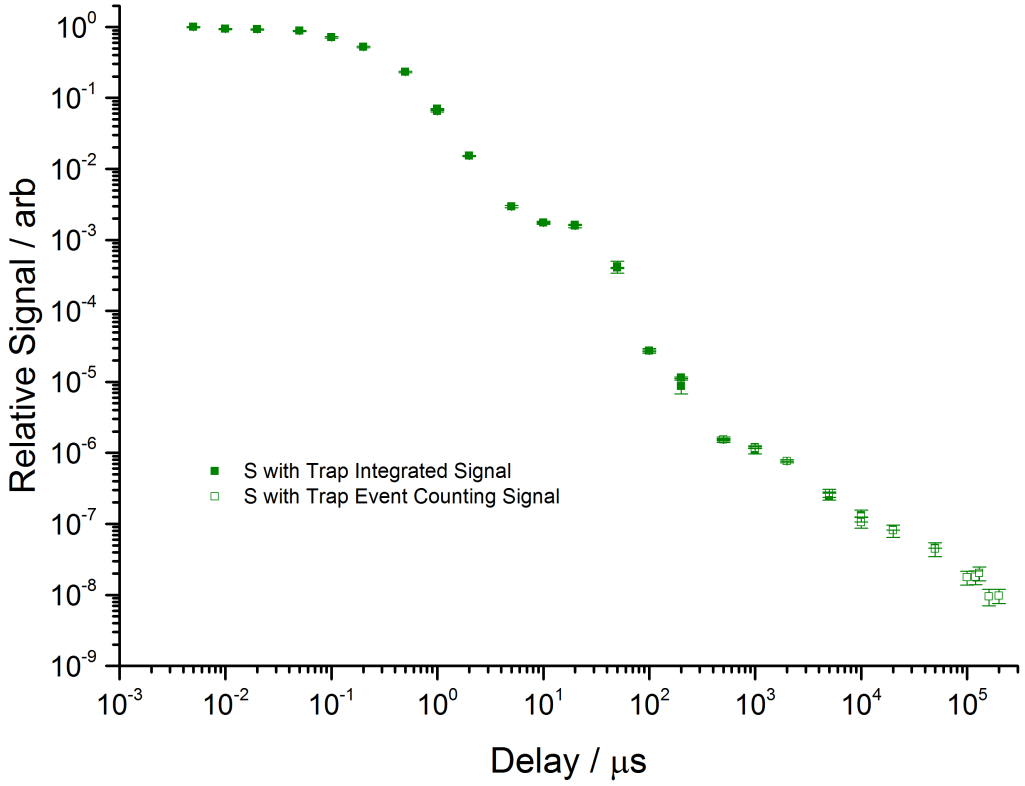

Fig. 8.13 Decay in sulphur REMPI signal for increasing delays between the dissociation and probe lasers for S with the cryostat in operation and the magnetic trap in place.

lasers into the chamber needed to be adjusted in order to compensate for this. This was accomplished by optimising the dissociation laser to lie centrally through the chamber and then adjusting the probe laser alignment to maximise the detected REMPI signal. This process, however, needed to be performed relatively quickly to reduce the likelihood of saturation of the pumping surfaces during the experiment. The results from the photostop measurements taken with the cryostat active are shown in Figs. 8.13 and 8.14.

The first set of measurements was performed with an attempt to photostop S as this gave a far stronger REMPI signal. As can be seen in Fig. 8.13, the initial 'hump' as seen in the measurements without running the cryostat appears to be still present but the second rise has been removed. Following the initial hump, the relative signal appears to decay continuously until it reaches a relative signal of around 5×10^{-9}. That being said, there is no apparent change in this decay rate which would be indicative of the effect of the magnetic trap on the slower molecules. On account of this we decided to see if any kind of effect could be demonstrated with the photostop

of SH as shown in Fig. 8.14.

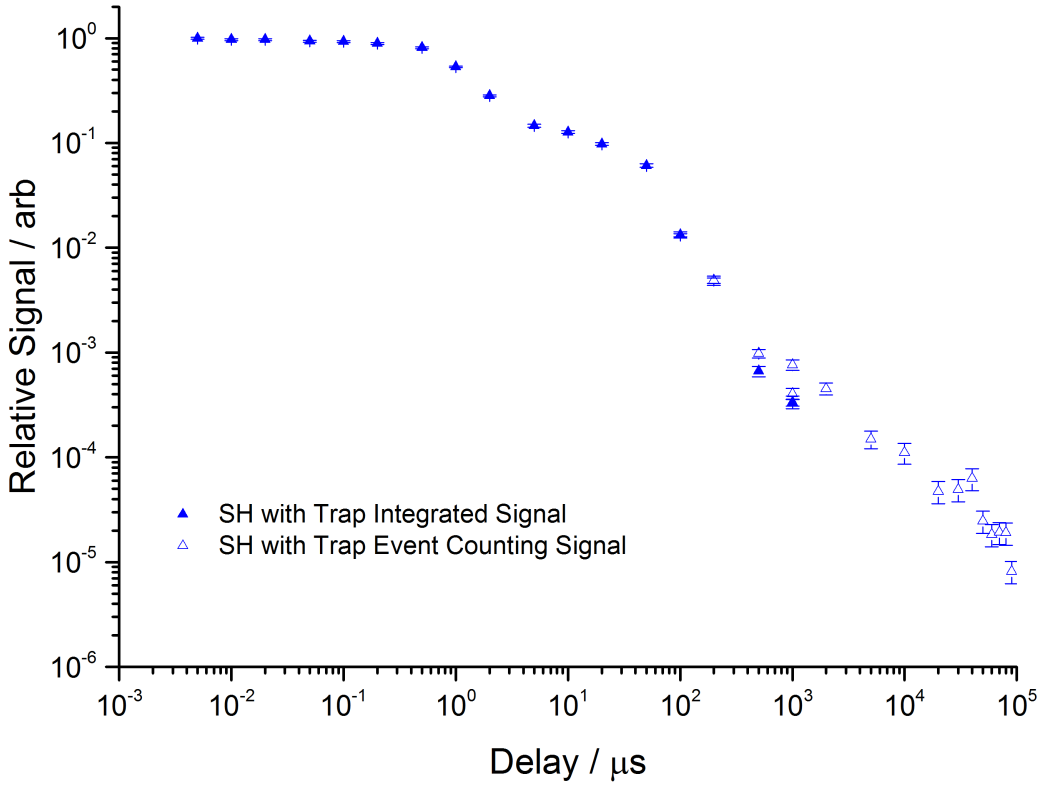

Fig. 8.14 Decay in SH REMPI signal for increasing delays between the dissociation and probe lasers for SH with the cryostat in operation and with the magnetic trap in place.

Initially it appeared that (as with S) there was no real evidence of trapping as, discounting the first 'hump', there appears to be a relatively constant decay at the longer time delays, but in this case reaching a relative signal of around 5×10^{-6}. However, if we examine this with a log/lin format we see a gradual decay emerge after around 1 ms in a similar fashion to the trapping shown in [115]. As such we initially examined the difference between measurements taken at different molecular beam speeds by comparing the photostop gas mixture with pure H_2S as shown in Fig. 8.15. Although there may be some small difference in the relative signals on this tail of the decay, the differences are not statistically valid enough to make definitive conclusions from. So for further confirmation we removed the magnets from the trap, replaced them with copper blanks and retook the measurement as shown in Fig. 8.16.

The difference in the decays with and without the trap are far clearer and more distinct than for the measurements with different velocities. From this one might be

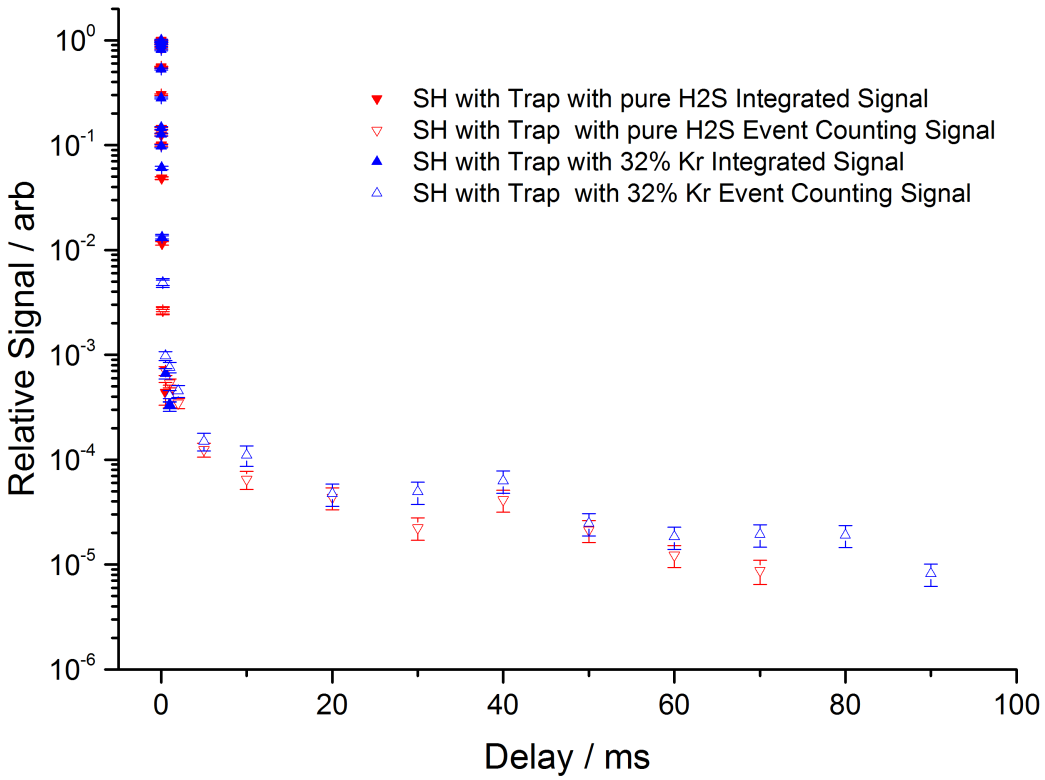

Fig. 8.15 Decay in REMPI signal for increasing delays between the dissociation and probe lasers for SH with the cryostat in operation and using a range of different molecular beam mixtures as specified in the legend.

tempted to declare victory as on the outset this appears to be evidence of trapping. However, it would be expected that the non-trapping signal would simply continue to decay over time as there is nothing to hold the molecules in place so they would all eventually leave. Instead the measurements appear to show the same levelling off as seen with the measurements with the trap.

Although the tail of the decays can be described as "levelling off", the total magnitude is still decreasing for increasing delays which indicates that this effect is dependent on the molecular beam. To confirm this, measurements of the REMPI signal (still without the trap present) at 70 ms were taken with and without the dissociation laser. When compared, these measurements were statistically indistinguishable from each other thus indicating that the signal shown is SH signal produced from the dissociation of the remaining H_2S in the trap volume by the probe laser.

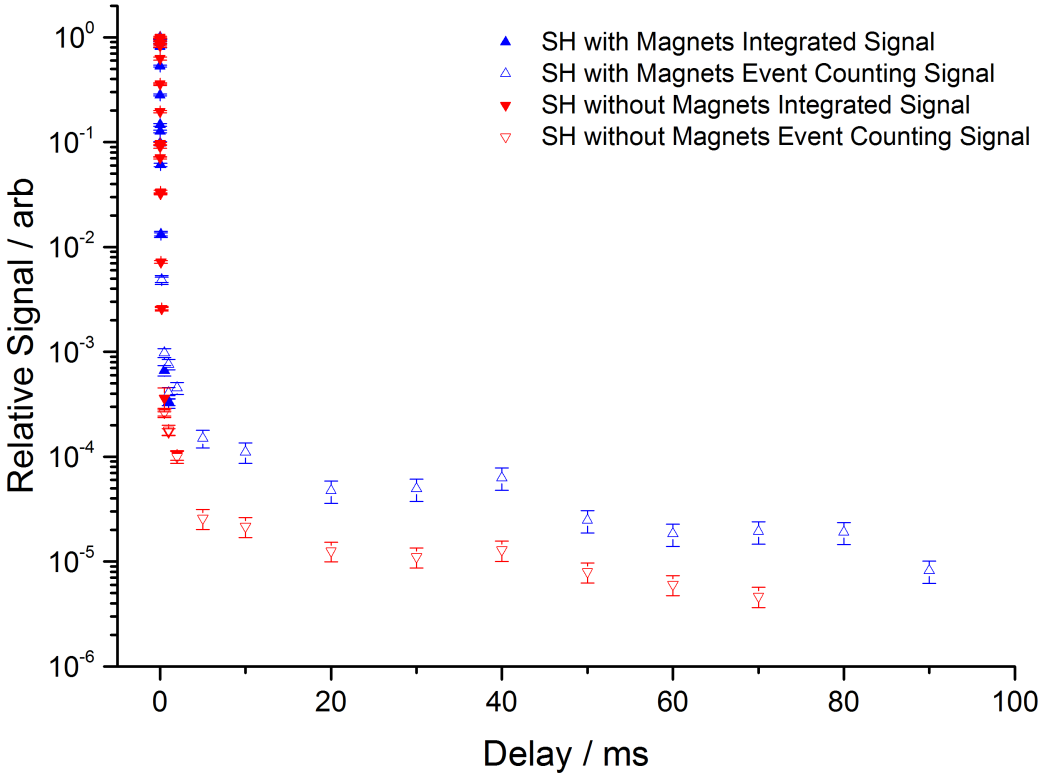

Fig. 8.16 Decay in REMPI signal for increasing delays between the dissociation and probe lasers for SH with the cryostat in operation for both with and without the magnetic trap in place.

8.3.7 Background subtracted measurements

Since the submission of this thesis, work on this experiment has continued by other members of the group[3] applying the use of a background reduction method to reduce the obscuring effect of the background gas from the molecular beam. In essence this involves adjusting the operation of the experiment such that the dissociation laser fires at one half of the repetition rate of the nozzle and probe laser and taking measurements with and without the dissociation laser present. These measurements are averaged separately and the background (without the dissociation laser) is subtracted from the main signal results (with the dissociation laser). The results from this investigation are shown in Fig 8.17.

This clearly shows a definitive change in the decay in SH signal with the trap present after delays of around 5 ms, after which there is a slower decay rate. This is highly similar to the previously recorded results, the main difference being that the "trap-

[3] Specifically, Jack Eardley and Eckart Wrede.

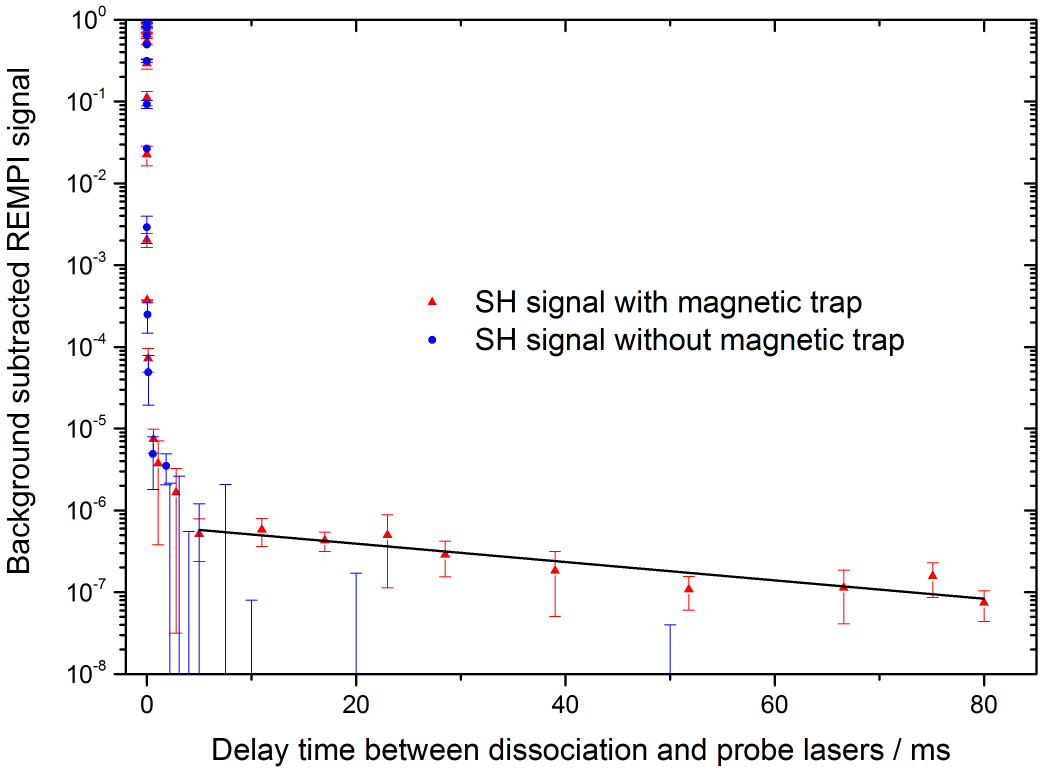

Fig. 8.17 Decay in REMPI signal for increasing delays between the dissociation and probe lasers for SH with the cryostat in operation whilst utilising background subtraction with and without the magnets in place (in red and blue respectively). The black line is a fit of the trap loss rate of the trapped SH molecules

ping" level is significantly lower than the prior measurements. This however would be expected given the introduction of background subtraction. The most striking result from this is that there is a clear distinction between the measurements with and without the magnetic trap in place. This definitively demonstrates the magnetic trapping of cold SH radicals from the photostop process as, with the magnets in place, the background subtracted SH signal is measurable up to 80 ms, whereas without the magnets it quickly becomes undetectable after a few milliseconds. From performing a linear regression on the trapping results with a delay greater than 5 ms, a $1/e$ trap lifetime of 40 ± 1 ms was obtained.

8.4 Discussion

The unexpected discovery of SH dissociation by the 213 nm laser can be seen as something of a mixed result. The primary problem with this is that this mechanism

ultimately leads to the depletion of SH molecules and thus will deplete the supply for any SH photostop measurements. This can be rectified by using a shorter dissociation laser wavelength, namely the 193 nm output of an ArF excimer laser. Using this alternative dissociation method has two benefits, first the absorption cross-section for H_2S is significantly higher at 193 nm when compared to 213 nm, thus giving a greater yield of SH. Additionally, the Franck-Condon overlap for the dissociative transition in SH is reduced at this wavelength, thus meaning fewer SH molecules are dissociated (and therefore lost). Despite this dissociative issue, the production of S in this manner does give rise to the possibility of performing two-photon photostop experiments on S or potentially more complex molecules or other species that would be difficult to produce in a single photodissociation process. This does, however, rely on the assumptions regarding the mechanics of the SH dissociation being valid which, although justified in the literature, would require additional experimental evidence to confirm (preferably using a system with velocity map ion imaging).

Although a definitive difference was initially shown between measurements of the photostop of SH with and without the magnetic trap, the evidence produced without background subtraction was not a conclusive presentation of the trapping effect. The reasoning behind this is predominantly on account of the issue with the dissociation of background gas, which may be masking the signal of the trapped molecules. One might argue that the distinct difference in the signal essentially makes this a moot point as the signal at the tail end of the photostop decay is simply a summation of the signal from the trapped molecules and the background so therefore the difference between the signals with and without the trap in place is the result of the trapped molecules. While this is a valid position, it is not unassailable as by necessity the measurements with and without the trap in place needed to be taken at different times as the chamber needed to be vented and the trap removed. Therefore it is potentially possible that there would be some change in alignment or optimisation between the two measurements, which could dictate the magnitude of the background signal. That being said, the methods used for the optimisation and alignment were the same for each set of measurements, as were the lasers used

so it is unlikely that such a substantial difference would occur as a result of a slight misalignment. Nevertheless, as there is some contention as to the validity of this result, it is evident that trapping has not been sufficiently demonstrated with these initial measurements alone.

The results from the background subtracted measurements have clearly demonstrated the magnetic trapping of photostopped SH radicals, with a measurable trap lifetime of $1/e$ trap lifetime of 40 ± 1 ms. These results are similar to the findings of previous investigations of the photostop of Br atoms [115, 116], but the extension of this technique to the trapping of molecules was not trivial. The trends shown from the background subtracted results also correlate with the previous direct (i.e. non-background subtracted) measurements of the trapping of SH shown in Fig. 8.16. However, the background subtracted results more definitively demonstrate the trapping effect with the absence of potential background gas contribution to the signal. That said, for future investigations with this technique, the clear preference would be to reduce this issue so that background subtraction would not be necessary as, by its very nature, these experiments take twice as long as direct measurements.

In terms of the overall sensitivity of the apparatus, the experiments have shown that it is highly sensitive and able to cover a broad range of signal, covering up to 6 orders of magnitude for the REMPI of SH and up to 9 orders of magnitude for the REMPI of S. When compared to the historical measurements where signal was lost after an approximately 3 orders of magnitude decrease in signal, this is clearly a vast improvement.

As has already been stated, the primary issue which has caused difficulty in the demonstration of trapping is the background gas remaining in the trap volume. Given the vast quantity of pumping surfaces in the area it is unlikely that this issue is a result of insufficient pumping, instead it is more likely that this is due to the broad temporal width of the molecular beam. There are a number of potential methods that can be applied to reduce the width of the molecular beam, which will be outlined in 9.1.

8.5 Conclusions and next steps

The application of REMPI for the photostop measurements has provided a significant improvement in terms of sensitivity when compared to the historical photostop measurements as well as the CELIF measurements. Additionally the unexpected discovery of the photodissociation of SH has opened up the potential for expansions of the photostop technique using multi-stage processes. However, the issue of background signal obscuring our measurements has proven to be somewhat problematic for the demonstration of trapping. That said, more recent results using background subtraction have definitively demonstrated of the trapping of SH radicals using photostop.

Part IV

OUTLOOK

9. THE FUTURE OF PHOTOSTOP

9.1 Solutions to current issues

There have been a number of successes in the photostop project which have ultimately culminated with the recent definitive demonstration of the magnetic trapping of photostopped SH radicals. In particular, the REMPI apparatus has demonstrated a significant dynamic range and sensitivity both for raw signal and with background subtraction. That said there are still a number of issues that hamper the experiment and could be improved upon for future investigations.

As previously stated, the predominant issue that proved problematic in the detection of trapped S/SH is the background gas that remains from the molecular beam. Although background subtraction does reduce this issue, this solution is inefficient as measurements by necessity take twice as long to take. Combating the background gas issue directly will not come without difficulty, but there are some potential solutions to this issue. First and foremost is the application of proprietary molecular beam sources to generate shorter and higher density molecular beams. To this end we have tested an Even-Lavie valve which we jerry-rigged into our apparatus. Although this valve has previously been shown to produce molecular beams with FWHM below 100 µs with noble gases [111], in our experiments we have not experienced this. This discrepancy is likely due to a combination of different factors, first H_2S has significantly different properties from noble gases so there is no guarantee that the supersonic expansion would perform in the same manner. Additionally, as the Even-Lavie valve has been shown to produce much higher density molecular than the General Valve it needed to be positioned significantly further back so that the skimmer would not experience choking issues. That being said, with a modified

high density skimmer this issue should dissipate so that the nozzle can be moved closer. That said, we are currently collaborating with a group in Nijmegen to adapt their Nijmegen Pulsed Valve (NPV) [117] for use in this experiment. Although this could provide the narrow molecular beam width required, this valve has yet to be tested with H_2S so it is uncertain how well this will compare to previous results. Given the resources readily available, the most promising solution to this issue would be to incorporate a chopper to externally shorten the molecular beam as has been applied to other experiments [118].

There are a number of options as to how a chopper could be incorporated into the structure. A common method of chopping a molecular beam is to use a rotating wheel with a narrow slit in it, which is set to rotate such that the wheel blocks the molecular beam and only lets through a small portion that passes through the narrow slit. Although this is a perfectly serviceable method, as the internal structure of the apparatus is small, it may become difficult to mount and operate. As an alternative we are proposing to use an arm on a pivot to serve as a shutter to block the beam. To accomplish this we are planning on re-purposing the mechanical arm from a hard drive to serve as a lever, which is an adaptation that has been used previously for laser shutters [119–121]. At the time of writing some initial tests have been performed on this idea which have unfortunately shown that the time taken to move the lever arm the required distance to block the molecular beam is too long to have significant effect on the molecular beam profile. That said, the principle remains sound and could be implemented if an alternative and faster-moving lever arm mechanism could be found.

A further addition to the chamber that has been added is the introduction of a form of differential pumping as shown in 9.1. The purpose of this is to reduce the level of background gas from the nozzle by effectively segregating it such that only the portion of the gas pulse which passes through the skimmer will have a direct line of sight to the trap centre or the outer stage. The rest of the gas from the nozzle is guided upwards towards to the turbopump by a “chimney” structure so that it can be pumped away more efficiently. In practice some of the gas that travels up the

chimney may, after leaving the chimney, flow downwards towards the outer stage, however the top surface of the outer stage is entirely closed off so there remains no direct line of sight to the trap centre, meaning that in order for gas to reach the trap centre it would have to take a route which makes it likely for it to hit (and become adsorbed to) the walls of the cryostat structure.

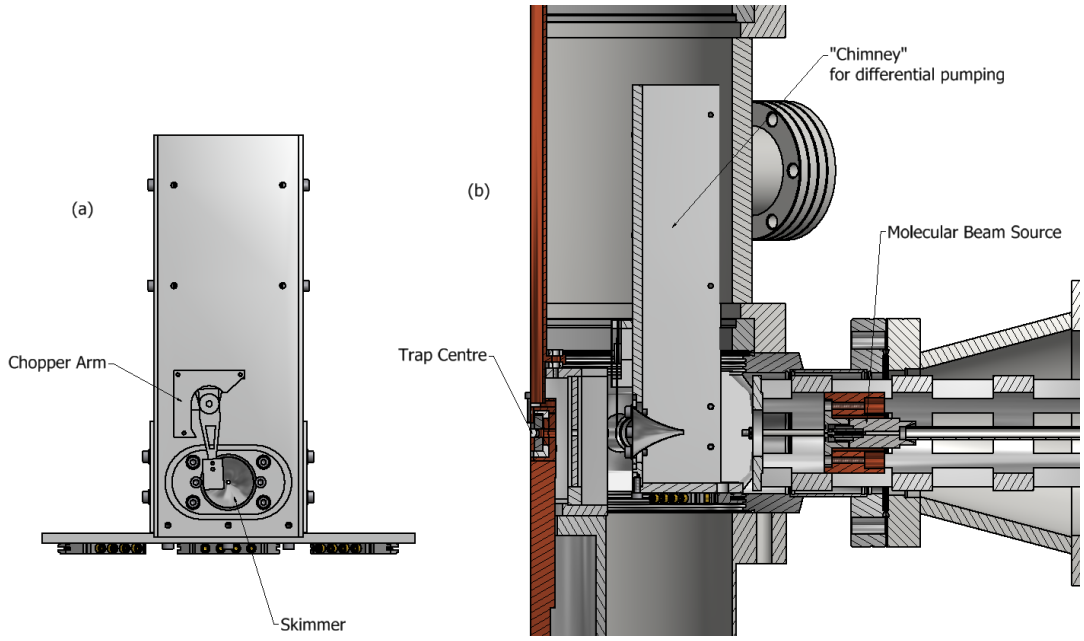

Fig. 9.1 Schematic representation of the planned adaptations to be made to the chamber to allow the incorporation of the chopper arm with a front view of the chopper in position (a) and a cross-sectional view of the chopper mounted in the chamber to the trap centre (b).

9.2 Future Advancements

Assuming that the above issues are successfully combated, the photostop experiment could be expanded further in a range of possible directions. As of this moment the most promising directions for advancement are the reincorporation of CELIF, cooling the molecules further and potentially producing more complex cold molecules.

9.2.1 Further additions to the design

One of the primary limitations of this experimental apparatus in its current state is the lack of velocity map ion imaging, which make measurements of the veloc-

ity of both the dissociated molecules and the molecular beam speed potentially problematic. The justification for the exemption of this capability was to allow for significantly easier access to the central chamber for alterations as well as to maximise the efficiency of the turbopump by positioning it as close to the molecular beam source as possible. Given how efficient the pump has demonstrated to be, it may be possible to make adjustments to the extend the top of the chamber upwards so that the required phosphor plate and CCD camera can be mounted behind the MCP in vacuum. However this may not be practically possible use to the limited vertical space in the lab where it currently sits so further additions may prevent the pump from being easily and effectively removed.

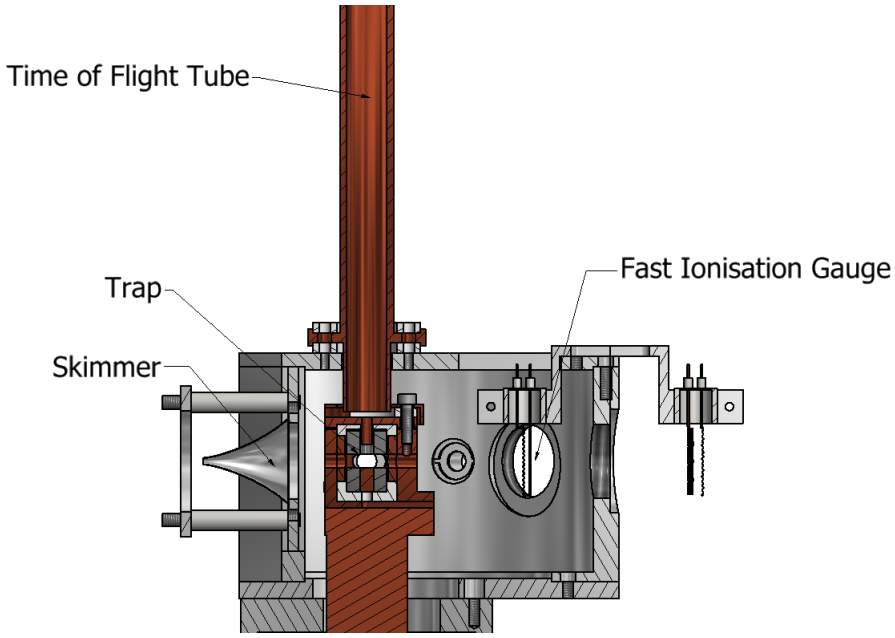

Fig. 9.2 Schematic representation of the adaptation made to the chamber to allow the incorporation of a double FIG mount for more accurate molecular beam speed measurements.

As an alternative to incorporating VMI there is the potential to improve the molecular beam speed measurements by incorporating additional FIGs as shown in Fig. 9.2. In practice this would allow the molecular beam speed to be measured by simply recording the molecular beam profile at both FIGs and measuring the time difference between them to determine the velocity. Although the principle of this is identical to the current method of measuring molecular beam speeds there are some distinct advantages. First, this apparatus has a more distinctly defined difference

between the two points of measurement and so could provide more precise and repeatable measurements. Second, the measurements with the FIGs are significantly faster to take than when using the laser as in the latter case the laser needs to move onto each delay from the nozzle and make a recording whereas the FIG can remain temporally stationary. This increased efficiency would be a definitive benefit as it will allow for greater fine tuning of gas mixtures to produce molecular beam speeds closer to the target velocity for photostop, and hence more trapped molecules.

9.2.2 Reincorporation of CELIF

Although the results from the initial CELIF measurements were less than ideal, the CELIF technique has been shown to be a relatively straightforward and highly sensitive method of measuring molecules and is something that should be explored further. In the context of this experiment the main impediment to the success of CELIF was the stray light and background signal produced by the dissociation laser. This is a significant issue as the predominance of the stray light occurs at the short delays where direct absolute number density calibration using CRDS would take place and so could cause issues. However this is not insurmountable as there are methods that could reduce this stray light such as the incorporation of laser baffles or filters.

If the stray light can be successfully accounted for, it raises a very real possibility of making absolute number density measurements of the trapped molecules. Given what we have seen thus far, it is unlikely that this could be performed entirely by CELIF as it has thus far not demonstrated the required level of sensitivity, however this does open the possibility of a pseudo absolute number density calibration of REMPI. What this would entail is matching up the photostop decays for both techniques so that an absolute number density of molecules producing the REMPI signal could be assumed from the measured number density using CELIF. This would be admittedly an indirect calibration, but given that at present the number of trapped molecules could only be approximated using the REMPI signal, this would be a definitive improvement.

9.2.3 Additional cooling

Given that photostop is somewhat of a hard and fast technique it is unsurprising that the final temperature still lies above the ultracold regime (the magnetic trap depth is approximately in the order of 200 mK for the target SH state). On account of this it is clear that in order to apply this technique for use in applications like the quantum simulator further cooling would be required. On account of how this experiment is constructed there are numerous possibilities for advancement in this direction. First, as the chamber is constructed around a central cryostat, there is the possibility of feeding in a buffer gas source into the trap volume for additional cooling. However, buffer gas cooling has limited effect for reaching sub-millikelvin temperatures and so would not necessarily aid that much in further cooling the stopped molecules, but it may still aid in cooling the molecular beam.

As an alternative to buffer gas cooling, there is the possibility of incorporating sympathetic cooling to further cool the trapped molecules. Admittedly this would require significant redesigning of the current apparatus to accommodate the required optical access for laser cooling the atoms which will be sympathetically cooling the target molecules. Additionally, the high density influx of the molecular beam may result in losses of the laser cooled atoms, thus making the cooling less efficient.

Assuming that the target molecules can be reliably cooled and trapped, there is the possibility that photostop could be used as a source of cold molecules, which can then be further cooled by a Zeeman or Stark decelerator. In this circumstance the target molecules would likely be first accumulated in the trap before extracting them from the trap with and feeding them into a decelerator. If this could be achieved it would mean that decelerator could be loaded with an initially cold and slow moving source so that it would not need to be as long to produce significantly slower/colder molecules. The key to this however is the extraction process from the trap, which could involve implementing a pulsed magnetic field to push the trapped molecules out of the trap when the trap density has accumulated sufficiently. This could prove to be a challenging prospect on account of the small size of the trap

but in principle this could provide a novel method of loading a decelerator and thus produce significantly colder molecules.

Alternatively, the photostop technique could be applied to molecules that have already been decelerated. Both Stark and Zeeman decelerators generate slow moving molecules with high rotational state purity, which could be brought to a standstill by photostop. This has the advantage that as the decelerator significantly reduces the velocity of the target molecules, the photostop dissociation energy can be tuned to near threshold levels and therefore reduce the size of the Newton sphere from the dissociation meaning that a greater proportion of the dissociated molecules will be directly slowed by the process. Further, as the dissociation is near threshold, the possibility of rotational heating of the fragments is significantly reduced.

Additionally, the technique could be used to create translationally cold but rotationally hot molecular super rotors. Super rotors are molecules with rotational energy that exceeds their bonding strength, so in effect they are only quasi-bound. With the molecules rotating so fast collision events take longer than the revolutionary period meaning that the molecules mostly perform elastic collisions, which hardly affect their rotation [122]. Crucially, the inelastic collision rates for these molecules are inversely proportional to the J rotational quantum number of the rotor, ultimately leading to longer lifetimes for these states. As photostop can be tuned to be rotationally selective, there is the potential of generating molecules from the output of a decelerator in a single high rotational state. In effect this could lead to the production of a translationally cold super rotors which have long lifetimes for study. That said, this would be an ambitious undertaking and would require the application of a functioning decelerator as well as a femtosecond laser, and would thus require significant instrumentation development before this experiment could be realised.

10. OVERALL SUMMARY AND CONCLUSIONS

Given the initial state of the photostop experiment at the beginning of this project, significant advances have been made during this project. In particular the design and construction of the new experimental apparatus has allowed for the testing of different measurement techniques and has the potential to be easily re-purposed for any number of applications thanks to the multiple axes of optical access to the chamber centre and the adaptability of the structure as a whole.

Despite being not entirely successful for this experiment, the CELIF technique, has shown some promise as a method for measuring absolute number densities of small numbers of molecules. Although a detection limit could not be reached with measurements of SO_2 in this experiment, the relative simplicity of the construction and application of this technique has shown that it could easily be applied to other systems. The primary limiting factors of this technique largely lie in the measurement of the fluorescing light. Firstly, the issue of direct calibration with CRDS at high number densities can be an issue as the results from SO_2 have shown a significant discrepancy between the calibrated CELIF signal and the measured CRDS signal. This however may be an issue of the method of calibration and could be corrected for; besides which, the primary interest for CELIF application is in the determination of lower number densities, so the poor calibration at higher number densities is of little consequence if the calibration is consistent at lower number densities. The major limiting issue for the application of CELIF with photostop is that of stray light obscuring the fluorescence signal. An inevitable consequence of using a cavity is that the light intensity of the probe laser is lost in favour of a longer interaction with the substance in question. As such there is very little than can be done to compensate for external sources of light (such as the dissociation laser), besides re-

ducing the stray light with barriers or filters. However, there still remains the issue of the fluorescence of the windows themselves, which provided a level of background signal in the CELIF only experiments. This background level will ultimately determine the detection limit of the CELIF experiment in question, and in this case was exacerbated by the fact the probe laser wavelength is in the ultra-violet range. That being said, CELIF experiments at longer wavelengths will have less issue with this, which, coupled with the fact that it is easier to get higher reflectivity mirrors ar longer wavelengths, could lead to highly sensitive molecular measurements if properly applied.

Although initially problematic due to the small scale of the ion optics, the REMPI detection method has proven to be highly sensitive and capable of detecting a large range of molecular number densities. The initial tests with Xe clearly showed that we could obtain a strong signal with good mass resolution using the mass-resolving mode. The under-performance of the "Hoover" mode was unfortunate, but given the strong signal found from the mass resolving mode, this was not a significant hindrance. That being said, now that we have a greater understanding of the failings of the hoover mode, there could still be application for this mode in the detection of slow moving molecules.

The initial measurements of the REMPI signal of SH confirmed the high sensitivity and mass resolution of the ion extraction system. The unexpected discovery of the S production from the photodissociation of SH was an added bonus which leads to the possibility of a multi-stage photostop process, which may open up the possibility of producing a greater range of cold molecules. The early measurements of the SH and S photostop decays clearly demonstrated the improved sensitivity of the new apparatus and technique when compared to the old one, as a strong signal was measured at significant delays after the initial photodissociation. However, due to the significant issues with background gas obscuring signal, this was not sufficient to demonstrate the trapping of either species, hence the necessity of the cryostat. With the cryostat in operation the sensitivity of the apparatus was further demonstrated, showing that the REMPI detection scheme could cover at least 6 orders of magnitude of SH

signal and at least 8 for S signal. However, despite this sensitivity, the trapping of either species could not initially be demonstrated due to obscuring of trapping signal at long delays by the broad molecular beam. That said, recent measurements with the instrument using background reduction have now conclusively demonstrated the trapping of photostopped SH.

Despite this success, the issue of the broad molecular beam obscuring the trapped molecule signal remains a significant obstacle for further development. To combat this, background reduction has been used to great effect. Additionally, work is under way to incorporate a chopper system into the system as well as a high density Nijmegen-pulsed valve to more definitively remove this issue.

Despite these advancements (and those to come) it is still self-evident that the photostop technique is not an optimum method for producing large numbers of cold molecules. This is self-evident given the substantial difference in the number of dissociated molecules compared to the stopped/trapped molecules. Although there is the possibility for accumulation of molecules in the magnetic trap over several pulses, this is limited by the high density of the molecular beam which at a certain point would result in losses in the trap as the molecules will effectively be knocked out by the incoming molecular beam.

To summarise, the photostop experiment has been rebuilt from ground up and trapping of cold photostopped molecules has now been demonstrated. In particular the new apparatus has shown a significant improvement in terms of sensitivity when compared to previous measurements. That said, there are still issues to address, particular with background gas from the molecular beam obscuring the signal. However steps are being taken to address these issues and there is significant potential for further development of this experiment.

REFERENCES

[1] Anderson, M. H., Ensher, J. R., Matthews, M. R., Wieman, C. E., and Cornell, E. A. *Science* **269**(5221), 198–201 (1995).

[2] Regal, C. A., Greiner, M., and Jin, D. S. *Physical Review Letters* **92**, 040403 Jan (2004).

[3] Qumner, G. and Julienne, P. S. *Chemical Reviews* **112**(9), 4949–5011 (2012).

[4] Balakrishnan, N. and Dalgarno, A. *Chemical Physics Letters* **341**(56), 652 – 656 (2001).

[5] Herschbach, D. *Reviews of Modern Physics* **71**, S411–S418 Mar (1999).

[6] Moore, M. G. and Vardi, A. *Physical Review Letters* **88**, 160402 Apr (2002).

[7] Carr, L. D., DeMille, D., Krems, R. V., and Ye, J. *New Journal of Physics* **11**(5), 055049 (2009).

[8] Herrera, F. *Physical Review A* **78**, 054702 Nov (2008).

[9] Bethlem, H. and Meijer, G. *Inernational Reviews in Physical Chemistry* **22**(1), 73–128 Jan-Mar (2003).

[10] Gilijamse, J. J., Hoekstra, S., van de Meerakker, S. Y. T., Groenenboom, G. C., and Meijer, G. *Science* **313**(5793), 1617–1620 (2006).

[11] Sawyer, B. C., Stuhl, B. K., Wang, D., Yeo, M., and Ye, J. *Physical Review Letters* **101**, 203203 Nov (2008).

[12] Hudson, E. R., Lewandowski, H. J., Sawyer, B. C., and Ye, J. *Physical Review Letters* **96**, 143004 Apr (2006).

[13] DeMille, D., Sainis, S., Sage, J., Bergeman, T., Kotochigova, S., and Tiesinga, E. *Physical Review Letters* **100**, 043202 Jan (2008).

[14] Schiller, S. *Physical Review Letters* **98**, 180801 Apr (2007).

[15] Zelevinsky, T., Kotochigova, S., and Ye, J. *Physical Review Letters* **100**, 043201 Jan (2008).

[16] Shelkovnikov, A., Butcher, R. J., Chardonnet, C., and Amy-Klein, A. *Physical Review Letters* **100**, 150801 Apr (2008).

[17] Chengalur, J. N. and Kanekar, N. *Physical Review Letters* **91**, 241302 Dec (2003).

[18] Darling, J. *Physical Review Letters* **91**, 011301 Jul (2003).

[19] Kanekar, N., Carilli, C. L., Langston, G. I., Rocha, G., Combes, F., Subrahmanyan, R., Stocke, J. T., Menten, K. M., Briggs, F. H., and Wiklind, T. *Physical Review Letters* **95**, 261301 Dec (2005).

[20] Hudson, J. J., Kara, D. M., Smallman, I. J., Sauer, B. E., Tarbutt, M. R., and Hinds, E. A. *Nature* **473**(7348), 493–U232 MAY 26 (2011).

[21] Kara, D. M., Smallman, I. J., Hudson, J. J., Sauer, B. E., Tarbutt, M. R., and Hinds, E. A. *New Journal of Physics* **14**(10), 103051 (2012).

[22] Tarbutt, M. R., Hudson, J. J., Sauer, B. E., Hinds, E. A., Ryzhov, V. A., Ryabov, V. L., and Ezhov, V. F. *Journal of Physics B: Atomic, Molecular and Optical Physics* **35**(24), 5013–5022 (2002).

[23] Schaller, R. *Spectrum, IEEE* **34**(6), 52–59 (1997).

[24] Shor, P. W. In *Proceedings of the 35th Annual Symposium on Foundations of Computer Science*, SFCS '94, 124–134 (IEEE Computer Society, Washington, DC, USA, 1994).

[25] Bihary, Z., Glenn, D., Lidar, D., and Apkarian, V. *Chemical Physics Letters* **360**(5-6), 459–465 Jul 17 (2002).

[26] Glenn, D., Lidar, D., and Apkarian, V. *Molecular Physics* **104**(8), 1249–1266 Apr 20 (2006).

[27] Zadoyan, R., Kohen, D., Lidar, D., and Apkarian, V. *Chemical Physics* **266**(2-3), 323–351 May 15 (2001).

[28] DeMille, D. *Phys. Rev. Lett.* **88**, 067901 Jan (2002).

[29] Barnett, R., Petrov, D., Lukin, M., and Demler, E. *Physical Review Letters* **96**, 190401 May (2006).

[30] Büchler, H. P., Demler, E., Lukin, M., Micheli, A., Prokof'ev, N., Pupillo, G., and Zoller, P. *Physical Review Letters* **98**, 060404 Feb (2007).

[31] Micheli, A., Pupillo, G., Büchler, H. P., and Zoller, P. *Physical Review A* **76**, 043604 Oct (2007).

[32] Feynman, R. P. *International Journal of Theoretical Physics* **21**, 467–488 June (1982).

[33] van de Meerakker, S. Y. T., Bethlem, H. L., and Meijer, G. *Nature Physics* (8), 595–602 (2008).

[34] Kay, J. J., Kłos, J., Alexander, M. H., Strecker, K. E., and Chandler, D. W. *Physical Review A* **82**, 032709 (2010).

[35] Strecker, K. E. and Chandler, D. W. *Physical Review A* **78**, 063406 Dec (2008).

[36] Elioff, M. S., Valentini, J. J., and Chandler, D. W. *Science* **302**(5652), 1940–1943 (2003).

[37] Kay, J. J., Paterson, G., Costen, M. L., Strecker, K. E., McKendrick, K. G., and Chandler, D. W. *The Journal of Chemical Physics* **134**(9), 091101 (2011).

[38] Kay, J. J., van de Meerakker, S. Y. T., Strecker, K. E., and Chandler, D. W. *Faraday Discussions* **142**, 143–153 (2009).

[39] Manai, I., Horchani, R., Lignier, H., Pillet, P., Comparat, D., Fioretti, A., and Allegrini, M. *Physical Review Letters* **109**, 183001 Oct (2012).

[40] Shuman, E. S., Barry, J. F., and DeMille, D. *Nature* **467**(7317), 820–823 OCT 14 (2010).

[41] Hansen, A. K., Staanum, P. F., Hojbjerre, K., Skyt, P. S., Sorensen, M. A., Kristensen, S. B., Gingell, A., and Drewsen, M. *Nature Physics* , 271–274 (2011).

[42] Barry, J. F., Shuman, E. S., Norrgard, E. B., and DeMille, D. *Physical Review Letters* **108**, 103002 Mar (2012).

[43] Zhelyazkova, V., Cournol, A., Wall, T. E., Matsushima, A., Hudson, J. J., Hinds, E. A., Tarbutt, M. R., and Sauer, B. E. *Physical Review A* **89**, 053416 May (2014).

[44] Wan, M.-j., Shao, J.-x., Huang, D.-h., Jin, C.-g., Yu, Y., and Wang, F.-h. *Physical Chemistry Chemical Physics* **17**, 26731–26739 (2015).

[45] Yzombard, P., Hamamda, M., Gerber, S., Doser, M., and Comparat, D. *Physical Review Letters* **114**, 213001 May (2015).

[46] Wan, M., Shao, J., Gao, Y., Huang, D., Yang, J., Cao, Q., Jin, C., and Wang, F. *The Journal of Chemical Physics* **143**(2), 024302 (2015).

[47] Zeppenfeld, M., Motsch, M., Pinkse, P. W. H., and Rempe, G. *Physical Review A* **80**, 041401 Oct (2009).

[48] Zeppenfeld, M., Englert, B. G. U., Gloeckner, R., Prehn, A., Mielenz, M., Sommer, C., van Buuren, L. D., Motsch, M., and Rempe, G. *Nature* **491**(7425), 570–573 NOV 22 (2012).

[49] Prehn, A., Ibrügger, M., Glöckner, R., Rempe, G., and Zeppenfeld, M. *Physical Review Letters* **116**, 063005 Feb (2016).

[50] Comparat, D. *Physical Review A* **89**, 043410 Apr (2014).

[51] Sparkes, B. M., Weber, K. P., Hawthorn, C. J., Walkiewicz, M. R., Vredenbregt, E. J. D., and Scholten, R. E. *Physical Review A* **92**, 023411 Aug (2015).

[52] Weinstein, J. D., deCarvalho, R., Guillet, T., Friedrich, B., and Doyle, J. M. *Nature* **395**, 148–150 (1998).

[53] Maussang, K., Egorov, D., Helton, J. S., Nguyen, S. V., and Doyle, J. M. *Physical Review Letters* **94**, 123002 Mar (2005).

[54] Egorov, D., Campbell, W., Friedrich, B., Maxwell, S., Tsikata, E., Buuren, L., and Doyle, J. *The European Physical Journal D - Atomic, Molecular, Optical and Plasma Physics* **31**(2), 307–311 (2004).

[55] Bakker, J. M., Stoll, M., Weise, D. R., Vogelsang, O., Meijer, G., and Peters, A. *Journal of Physics B: Atomic, Molecular and Optical Physics* **39**(19), S1111 (2006).

[56] Maussang, K., Egorov, D., Helton, J. S., Nguyen, S. V., and Doyle, J. M. *Physical Review Letters* **94**, 123002 Mar (2005).

[57] Larson, D. J., Bergquist, J. C., Bollinger, J. J., Itano, W. M., and Wineland, D. J. *Physical Review Letters* **57**, 70–73 Jul (1986).

[58] Myatt, C. J., Burt, E. A., Ghrist, R. W., Cornell, E. A., and Wieman, C. E. *Physical Review Letters* **78**, 586–589 Jan (1997).

[59] Modugno, G., Ferrari, G., Roati, G., Brecha, R. J., Simoni, A., and Inguscio, M. *Science* **294**(5545), 1320–1322 (2001).

[60] Hadzibabic, Z., Stan, C. A., Dieckmann, K., Gupta, S., Zwierlein, M. W., Görlitz, A., and Ketterle, W. *Physical Review Letters* **88**, 160401 Apr (2002).

[61] Schreck, F., Ferrari, G., Corwin, K. L., Cubizolles, J., Khaykovich, L., Mewes, M.-O., and Salomon, C. *Physical Review A* **64**, 011402 Jun (2001).

[62] Mudrich, M., Kraft, S., Singer, K., Grimm, R., Mosk, A., and Weidemüller, M. *Physical Review Letters* **88**, 253001 Jun (2002).

[63] McCarron, D. J., Cho, H. W., Jenkin, D. L., Köppinger, M. P., and Cornish, S. L. *Physical Review A* **84**, 011603 Jul (2011).

[64] Lara, M., Bohn, J. L., Potter, D., Soldán, P., and Hutson, J. M. *Physical Review Letters* **97**, 183201 Nov (2006).

[65] Wallis, A. O. G. and Hutson, J. M. *Physical Review Letters* **103**, 183201 Oct (2009).

[66] Tscherbul, T. V., Grinev, T. A., Yu, H.-G., Dalgarno, A., Kos, J., (), L. M., and Alexander, M. H. *The Journal of Chemical Physics* **137**(10), 104302 (2012).

[67] González-Martínez, M. L. and Hutson, J. M. *Physical Review Letters* **111**, 203004 Nov (2013).

[68] Blythe, P., Roth, B., Fröhlich, U., Wenz, H., and Schiller, S. *Physical Review Letters* **95**, 183002 Oct (2005).

[69] Roth, B., Blythe, P., Daerr, H., Patacchini, L., and Schiller, S. *Journal of Physics B: Atomic, Molecular and Optical Physics* **39**(19), S1241 (2006).

[70] Ostendorf, A., Zhang, C. B., Wilson, M. A., Offenberg, D., Roth, B., and Schiller, S. *Physical Review Letters* **97**, 243005 Dec (2006).

[71] Bethlem, H. L., Berden, G., and Meijer, G. *Physical Review Letters* **83**, 1558–1561 Aug (1999).

[72] Hogan, S. D., Sprecher, D., Andrist, M., Vanhaecke, N., and Merkt, F. *Physical Review A* **76**, 023412 Aug (2007).

[73] Bochinski, J. R., Hudson, E. R., Lewandowski, H. J., Meijer, G., and Ye, J. *Physical Review Letters* **91**, 243001 Dec (2003).

[74] Jung, S., Tiemann, E., and Lisdat, C. *Physical Review A* **74**, 040701 Oct (2006).

[75] Tarbutt, M. R., Bethlem, H. L., Hudson, J. J., Ryabov, V. L., Ryzhov, V. A., Sauer, B. E., Meijer, G., and Hinds, E. A. *Physical Review Letters* **92**, 173002 Apr (2004).

[76] Wall, T. E., Kanem, J. F., Dyne, J. M., Hudson, J. J., Sauer, B. E., Hinds, E. A., and Tarbutt, M. R. *Physical Chemistry Chemical Physics* **13**, 18991–18999 (2011).

[77] Narevicius, E., Libson, A., Parthey, C. G., Chavez, I., Narevicius, J., Even, U., and Raizen, M. G. *Physical Review Letters* **100**, 093003 Mar (2008).

[78] Wiederkehr, A. W., Motsch, M., Hogan, S. D., Andrist, M., Schmutz, H., Lambillotte, B., Agner, J. A., and Merkt, F. *The Journal of Chemical Physics* **135**(21) (2011).

[79] Trimeche, A., Bera, M. N., Cromieres, J. P., Robert, J., and Vanhaecke, N. *European Physical Journal D* **65**(1-2), 263–271 NOV (2011).

[80] Motsch, M., Jansen, P., Agner, J. A., Schmutz, H., and Merkt, F. *Physical Review A* **89**, 043420 Apr (2014).

[81] Dulitz, K., Tauschinsky, A., and Softley, T. P. *New Journal of Physics* **17**(3), 035005 (2015).

[82] Akerman, N., Karpov, M., David, L., Lavert-Ofir, E., Narevicius, J., and Narevicius, E. *New Journal of Physics* **17**(6), 065015 (2015).

[83] Ludlow, A. D., Zelevinsky, T., Campbell, G. K., Blatt, S., Boyd, M. M., de Miranda, M. H. G., Martin, M. J., Thomsen, J. W., Foreman, S. M., Ye, J., Fortier, T. M., Stalnaker, J. E., Diddams, S. A., Le Coq, Y., Barber, Z. W., Poli, N., Lemke, N. D., Beck, K. M., and Oates, C. W. *Science* **319**(5871), 1805–1808 (2008).

[84] Miller, J. D., Cline, R. A., and Heinzen, D. J. *Physical Review Letters* **71**, 2204–2207 Oct (1993).

[85] Wagshul, M. E., Helmerson, K., Lett, P. D., Rolston, S. L., Phillips, W. D., Heather, R., and Julienne, P. S. *Physical Review Letters* **70**, 2074–2077 Apr (1993).

[86] Shaffer, J. P., Chalupczak, W., and Bigelow, N. P. *Physical Review Letters* **82**, 1124–1127 Feb (1999).

[87] Kerman, A. J., Sage, J. M., Sainis, S., Bergeman, T., and DeMille, D. *Physical Review Letters* **92**, 033004 Jan (2004).

[88] Schnell, M. and Meijer, G. *Angewandte Chemie International Edition* **48**(33), 6010–6031 (2009).

[89] Trottier, A., Carty, D., and Wrede, E. *Molecular Physics* **109**(5), 725–733 (2011).

[90] Eppink, A. T. J. B. and Parker, D. H. *Review of Scientific Instruments* **68**(9), 3477–3484 (1997).

[91] Brouard, M., Campbell, E. K., Johnsen, A. J., Vallance, C., Yuen, W. H., and Nomerotski, A. *Review of Scientific Instruments* **79**(12) (2008).

[92] Doherty, W. G., Bell, M. T., Softley, T. P., Rowland, A., Wrede, E., and Carty, D. *Physical Chemistry Chemical Physics* **13**, 8441–8447 (2011).

[93] Murphy, E. J., Brophy, J. H., Arnold, G. S., Dimpfl, W. L., and Kinsey, J. L. *The Journal of Chemical Physics* **74**(1), 324–330 (1981).

[94] Zare, R. N. *Annual Review of Analytical Chemistry* **5**(1), 1–14 (2012). PMID: 22149473.

[95] Herbelin, J. M., McKay, J. A., Kwok, M. A., Ueunten, R. H., Urevig, D. S., Spencer, D. J., and Benard, D. J. *Applied Optics* **19**(1), 144–147 Jan (1980).

[96] Anderson, D. Z., Frisch, J. C., and Masser, C. S. *Applied Optics* **23**(8), 1238–1245 Apr (1984).

[97] O'Keefe, A. and Deacon, D. A. G. *Review of Scientific Instruments* **59**(12), 2544–2551 (1988).

[98] Vallance, C. *New Journal of Chemistry.* **29**, 867–874 (2005).

[99] Matthews, S. J., Willitsch, S., and Softley, T. P. *Physical Chemistry Chemical Physics* **9**, 5656–5663 (2007).

[100] Herzberg, G. *Molecular Spectra and Molecular Structure*, volume 1. D. Van Nostrand Company Inc: Princeton, (1950).

[101] Butler, J. *Applied Optics* **21**(20), 3617–3618 (1982).

[102] Sanders, S. E., Willis, O. R., Nahler, H., and Wrede, E. *arXiv:1308.1989* (2013). Submitted JCP.

[103] Kirste, M. *OH-NO Scattering at the Quantum Level*. Thesis, Fritz-Haber-Institut der Max-Planck-Gesellschaft and Freien Universitaet, (2012).

[104] Mizouri, A., Deng, L., S. Eardley, J., Hendrik Nahler, N., Wrede, E., and Carty, D. *Physical Chemistry Chemical Physics* **45**(15), 19575–19579 (2013).

[105] Brooker, G. *Modern Classical Optics*. Oxford University Press.

[106] Clements, J. H. *Physical Review* **47**, 224–232 Feb (1935).

[107] Keller-Rudek, H., Moortgat, G. K., Sander, R., and Sörensen, R. *Earth System Science Data* **5**(2), 365–373 (2013).

[108] Biswal, H. S., Kumar, S. V. K., and Wategaonkar, S. J. *The Journal of Chemical Physics* **128**(20) (2008).

[109] Gerwat, C. *Magnetic Trapping of SD Molecules Produced via Photostop*. 4th year project report, Durham University, (2012).

[110] Rosman, K. and Taylor, P. *Pure and Applied Chemistry* **70**(1), 217–235 JAN (1998).

[111] Luria, K., Christen, W., and Even, U. *The Journal of Physical Chemistry A* **115**(25), 7362–7367 (2011).

[112] Milan, J. B., Buma, W. J., and de Lange, C. A. *The Journal of Chemical Physics* **105**(16) (1996).

[113] Shiell, R. C., Hu, X. K., Hu, Q. J., and Hepburn, J. W. *The Journal of Physical Chemistry A* **104**(19), 4339–4342 (2000).

[114] Weiner, B. R., Levene, H. B., Valentini, J. J., and Baronavski, A. P. *The Journal of Chemical Physics* **90**(3), 1403–1414 (1989).

[115] Rennick, C. J., Lam, J., Doherty, W. G., and Softley, T. P. *Physical Review Letters* **112**, 023002 Jan (2014).

[116] Lam, J., Rennick, C. J., and Softley, T. P. *Physical Review A* **90**, 063419 Dec (2014).

[117] Yan, B., Claus, P. F. H., van Oorschot, B. G. M., Gerritsen, L., Eppink, A. T. J. B., van de Meerakker, S. Y. T., and Parker, D. H. *Review of Scientific Instruments* **84**(2), 023102 (2013).

[118] Lam, J., Rennick, C. J., and Softley, T. P. *Review of Scientific Instruments* **86**(5) (2015).

[119] Maguire, L. P., Szilagyi, S., and Scholten, R. E. *Review of Scientific Instruments* **75**(9) (2004).

[120] Scholten, R. E. *Review of Scientific Instruments* **78**(2) (2007).

[121] Landolsi, T., Dhaouadi, R., and Aldabbas, O. *Journal of the Franklin Institute* **348**(1), 1 – 11 (2011). Mechatronics and its Applications.

[122] Korobenko, A., Milner, A. A., and Milner, V. *Physical Review Letters* **112**, 113004 Mar (2014).

INDEX

A

C

E

F

L

M

P

R

S

U